5-2018

Microheater Array Powder Sintering (MAPS) for Printing Flexible Electronics

Nicholas Holt
University of Arkansas, Fayetteville

Microheater Array Powder Sintering (MAPS) for Printing Flexible Electronics

A thesis submitted in partial fulfillment
of the requirements for the degree of
Master of Science in Mechanical Engineering

by

Nicholas Holt
University of Arkansas
Bachelor of Science in Mechanical Engineering, 2014

May 2018
University of Arkansas

This thesis is approved for recommendation to the Graduate Council

Wenchao Zhou, PhD
Thesis Director

Steve Tung, PhD
Committee Member

Simon Ang, PhD
Committee Member

Abstract

Microheater array powder sintering (MAPS) is a novel additive manufacturing process that uses an array of microheaters to selectively sinter powder particles. MAPS shows great promise as a new method of printing flexible electronics by enabling digital curing of conductive inks on a variety of substrates. MAPS operation relies on establishing a precision air gap of a few microns between an array of microheaters, which can reach temperatures of 600°C, and a layer of conductive ink which can be deposited onto a flexible substrate. This system presents challenges, being: the fabrication of a microheater that can reach suitable temperatures in an acceptable time frame and is reliable, electronic control of a single microheater, electronic control of an array of microheaters, and precise control of the position of the array of microheaters relative to the substrate.

This work describes the design and fabrication of a printer which uses this novel technology to print flexible circuit boards. Various simulations are discussed which are used to explore the parameters affecting the MAPS printing process. Then, a small microheater array is fabricated and controlled using an electronic circuit using a PID feedback loop. This microheater array is used in an experimental proof of concept machine to print conductive lines onto a flexible substrate. Finally, a prototype MAPS printer is developed which is capable of using an improved microheater array to print simple circuits onto flexible substrates.

Acknowledgements

I gratefully acknowledge the help of my lab mates for their continued support throughout my graduate career: Chao Sui, Edidiong Udofia, and Mahsa Montezeri. I would also like to thank Lucas Galvan Marques for his role in designing electronic components that were used for this project. I would also like to credit Steven Brown, who helped tremendously in creating the first proof of concept printer described in this thesis. Thank you to Errol Porter, Clint Hardee, and other members of the HiDEC staff at the University of Arkansas for their expert advice when fabricating components for this project. Lastly, thank you to my advisor Dr. Wenchao Zhou for helping me reach my potential; I have not met anyone else with as much passion for a project as him. And of course, thank you to the University of Arkansas and Oak Ridge Associated Universities for the funding which made this project possible.

Table of Contents

List of Tables

List of Figures

CHAPTER 1

Introduction

1.1 Flexible Electronics

The growing demand for lighter, more portable, and more flexible technologies has spurred the development of flexible electronics. Flexible electronics consist of electronic components which can be attached to a flexible substrate to suit applications in many industries from consumer electronics, Internet of Things (IOT), and aerospace, to name a few. As consumer electronic devices become thinner and smaller, the demand for flexible electronics will continue to grow. However, the current production methods of flexible electronics have some problems that are holding back the growth in this market.

1.2 Manufacturing Technologies and Limitations

A flexible circuit board provides the structure for a flexible electronic device. It usually consists of conductive traces and dielectric layers deposited onto a flexible substrate, usually some plastic such as polyethylene terephthalate (PET), polyethylene naphthalate (PEN), or glasses or metal foils [1]. The conductive traces are formed by one of many conductive inks, which differ in their composition (silver, copper, graphene, etc. nanoparticle and flake inks), their intended deposition method (gravure, inkjet, etc.) and their content (solvent or water based, weight % solids, capping agents, etc.). Traditionally, silver micro and nano flake inks have been used for flexible electronics, although copper is gaining popularity due to its high conductivity and generally lower cost, although it suffers from oxidation problems during processing [2, 3, 4]. Nanoparticles are becoming more popular recently due to the phenomenon where a smaller particle size

reduces the melting temperature of the material [2, 5, 6, 7, 8, 9], which can make it possible to process inks on substrates with a lower heat tolerance.

The conductive ink is applied to the substrate via a printing process. Some common methods used in industry to print the conductive ink used for flexible electronics are gravure, flexographic, screen and inkjet printing. These processes can be integrated into a roll-to-roll production system, which is preferred for high-volume production, or a sheet-by-sheet system, which is preferred for low or medium-volume production. In a roll-to-roll system, a web of material (the substrate) runs through several rollers as it undergoes the deposition and curing processes. High volume roll-to-roll systems typically utilize gravure or flexographic printing methods, since they are characterized by rollers with images etched into the cylinder walls and are thus easy to integrate into a continuous roll-to-roll system. Gravure and flexographic are characterized by very high printing speeds and fine resolutions less than 20μm [10], but rollers are expensive and the production method lacks flexibility since the pattern to be printed cannot be changed quickly [11]. In contrast, screen printing is generally more suitable to low volume production when the flat-bed variety is used. Screen printing has traditionally been used in graphics printing but has seen great popularity in printing flexible electronics due to its relatively low cost, small and large-scale capacity, and the ease at which inks may be formulated [12]. Typically, screen printing is preferred for printing large particle silver inks because it offers the ability to accurately deposit thick films at economical production rates with inks that have a large rheological window [10, 13].

Gravure, flexographic and screen printing are categorized as impact printing methods, in that they all require some upfront toolmaking before printing can be accomplished. Flexographic and gravure printing require imaged rollers to be manufactured while screen printing requires a mesh

to be patterned using emulsion which can sometimes be done in-house, and there exist some digital imaging options for manufacturers who use screen printing extensively [14].

By contrast, Inkjet printing offers non-impact (or digital) printing, meaning it does not require any tooling to make unique prints: the image may be uploaded to the system as a bitmap image or some other file format. Inkjet printers use tiny nozzles to jet the conductive ink as droplets directly onto the substrate. Generally, each droplet is only a few picoliters so printing times can be very long. Although inkjet is typically considered very slow, the speed can be improved by increasing the number of nozzles, such as Ceradrop's X-Serie which uses thousands of nozzles to provide printing speeds of up to 500mm/s [15]. Besides the speed issue, there are other typical problems that plague some inkjet systems, such as clogged nozzles and satellite droplets, and inkjet systems are also very limited to certain ink formulations, because the ink must be very low viscosity, < 30cP [16, 17].

After deposition of the ink onto a substrate, the ink must be dried and cured to allow it to achieve high electrical conductivity and adhesion to the film. Generally, the drying and curing step is the speed-limiting factor in roll-to-roll production [16] and can be accomplished by a combination of hot air, infrared radiation or photonic curing. Thermal curing in an oven or by hot air is very time consuming [18], but photonic curing systems such as those offered by NovaCentrix allow full sintering of the nanoparticles in the ink in only a millisecond [19], however it often needs to be preceded by a drying step to remove liquids from the ink.

1.3 Problem Formulation

Based on our review, there are some fast production methods for printing flexible electronics that are often limited by the speed of the drying step but are also burdened by large costs associated

with tooling and equipment. There is a need in this market for a digital printing method which consolidates the patterning and curing processes into one step, which would eliminate costs associated with imaging (in the case of gravure, flexographic or screen printing) and post-processing (drying and curing). This new method should also outpace the speed of inkjet printing, currently the dominant digital printing technology in the market.

1.4 MAPS Printing

Microheater Array Powder Sintering (MAPS) is a novel Additive Manufacturing (AM) technology developed by the AM^3 lab at the University of Arkansas. MAPS technology resembles Selective Laser Sintering (SLS) in that it replaces the laser with a microheater array that can deliver a heat pattern onto a substrate over a small gap of gaseous medium (e.g., air) for sintering powder particles with scalability (using a large array of microheaters) and much less power consumption (~100s milliwatts for a microheater VS. ~100 watts for laser). MAPS can be used as a method of printing flexible electronics with metallic nanoparticle inks by combining the patterning and curing steps of existing printed electronics methods into one step as shown in Figure 1. After a thin layer of ink is deposited onto a flexible substrate, a microheater array can pass over while being separated from the substrate by a thin air gap. The microheaters selectively activate, which transfers heat directly to the ink. Then, the unused ink can be removed and recycled for other prints.

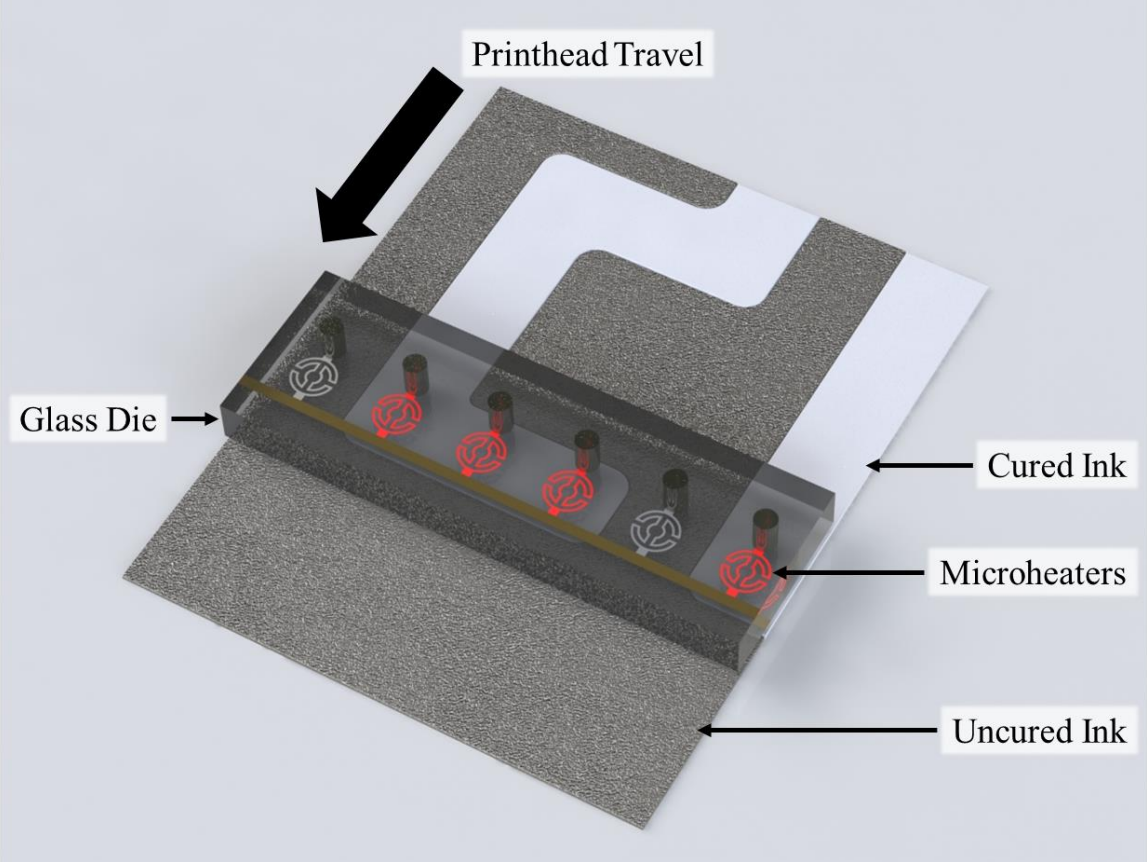

Figure 1 - Overview of the MAPS printing process: the powder particles underneath the selectively activated microheaters are sintered as the printhead moves overhead [20].

1.5 Outline of Thesis

Chapter 2 is a literature review: first, similar additive manufacturing technologies are explored; then, aspects of relevant technologies critical for MAPS are explored including rapid sintering, microheater design and fabrication, and air gap control. Chapter 3 describes the design and fabrication process of the microheater array used for this novel process; it also describes how the microheaters are controlled. Chapter 4 describes how an experimental proof of concept device was built, and reports on successful tests where conductive lines were printed on a plastic substrate. Chapter 5 describes an improved prototype printer and details the validation of its function. Chapter 6 offers a summary to this research and suggests areas for future development of this technology.

CHAPTER 2

Literature Review

This work aims to provide a basis for the development of MAPS printing technology. So far, there has not yet been developed a digital technology that can match the production capacity of screen printing for producing flexible electronics. Likewise, in the space of additive manufacturing, there are key areas that can be improved with MAPS. This literature review explores some areas relating to this new technology, notably similar additive manufacturing technologies, rapid sintering, microheaters and precision gap controls.

2.1 Similar Additive Manufacturing Technologies

Selective laser sintering (SLS), developed at the University of Texas at Austin, was among the first commercialized AM processes [21]. It uses a laser beam as the energy source to selectively induce fusion between powder particles layer by layer to build 3D structures. Originally developed to produce plastic prototypes (e.g., Nylon) using a point-wise laser scanning technique, SLS was subsequently extended to process metal and ceramic powders based on different sintering mechanisms [22, 23], such as solid state sintering, chemical induced sintering, liquid phase sintering, and full melting [24, 25, 26, 27]. Alternative energy sources have also been utilized, such as electron beam. These variants of SLS are categorized as powder bed fusion (PBF) processes, which have proven to be the most flexible general approach to AM due to its capability of working with a broad range of materials (including polymers, metals, ceramics, and composites) to directly manufacture end-use products with engineering-grade properties [28]. Unlike laser beams that heat the powder when photons are absorbed by powder particles,

electron beams heat powder by imparting the kinetic energy of accelerated electrons to the powder particles as utilized in the electron beam melting (EBM) process commercialized by Arcam AB (recently acquired by General Electric) [29]. Although it is more efficient to convert electrical energy into an electron beam than laser, and thus cheaper to achieve higher beam energies, the system poses a problem. The powder particles can be negatively charged by the electrons in the EBM and the repulsive forces between the negative charges can create a powder cloud due to the rapid expulsion of powder particles. This in turn repels incoming electrons, which typically require the powder bed of EBM to be very conductive and the minimum feature and powder particle size for EBM to be larger than that for SLS; this is to avoid the buildup of electron charges in the powder bed [30]. Extensive research and significant progress have been reported on understanding of the PBF processes (e.g., energy absorption by the materials, sintering kinetics, phase transformation, thermal expansion, heat transfer, wetting, etc.), and on optimizing the process parameters [26, 27, 31] to improve the accuracy and the properties of the finished parts [32, 33, 34, 35].

However, the SLS and EBM processes suffer from slow manufacturing speed, which is primarily limited by the point-wise scanning process. Several other powder-bed processes have been developed or have been under development to address this issue, including multi-beam laser additive manufacturing (MB-LAM) [36], selective mask sintering (SMS) [37], High-Speed Sintering (HSS) [38], selective inhibition sintering (SIS) [39, 40], and binder jetting [41]. MB-LAM uses two or more laser beams to scan simultaneously to increase productivity, but it would be very challenging and expensive to scale up using this approach as the complexity and cost of the system increase with the number of lasers. SMS, commercialized by Sintermask GmbH, fuses an entire layer of powder in a single exposure to reduce time using an infrared lamp that

projects the energy pattern of the layer through a dynamic mask, which is formed by electrostatically depositing toner on a glass plate for each layer (similar to that used in a photocopier). This method prints at a speed of 10 to 20 seconds per layer with a layer thickness of 50 to 120μm. Due to its layer-wise manufacturing approach, it can print about four times faster than a comparable SLS system at about one third of the costs. Due to the use of relatively low-power infrared lamps, no protecting environment (e.g., with nitrogen gas) is necessary as typically required for SLS systems. One main drawback of SMS is the limit of material choices due to the use of an infrared energy source, which requires the powder materials can readily absorb infrared light (typically dark-colored materials). HSS, originally developed at Loughborough University, also uses an infrared lamp to quickly scan over an entire layer to sinter the powder particles. The sintering pattern for each layer is achieved by depositing inks that are formulated to significantly enhance the absorptivity of infrared energy of the powders in the desired region using an inkjet printhead. By processing one layer at a time, HSS can print significantly faster than comparable SLS systems at a few seconds per layer with a lower machine cost due to the elimination of the laser. SIS, originally developed at the University of Southern California, is a similar process to HSS that also uses inkjet. Unlike HSS, SIS prints ink that inhibits the sintering of the powder particles at the outline of the desired geometry on each layer. A 3D structure can be fabricated by applying infrared radiation to each layer or bulk sintering all the layers in an oven. Although full information is not yet available, HP's multi-jet fusion technology appears to be similar to HSS or SIS or a combination of both by ink-jetting multiple chemical agents onto the powder layer. HP claims that the multi-jet fusion process can print ~10 times faster than comparable SLS systems. Binder jetting, originally developed at the Massachusetts Institute of Technology (MIT) in the early 1990s and commercialized by ZCorp

(now part of 3D Systems) and ExOne, is another similar process that uses an inkjet printhead to print binders onto a powder bed to join the powder particles together layer by layer. The printed green part (i.e., the bonded layers) needs to be post-sintered in an oven and infiltration of infiltrant materials is often needed to increase the density and the strength of the part. Although the printing speed of binder jetting is relatively fast, the post processing can take hours or even longer.

Although these processes, as they are being further developed, will undoubtedly provide a boost to the 3D printing industry, they have two main drawbacks. One is the energy source for sintering. Infrared radiation is an indirect energy source that needs to be converted into heat for sintering, which often imposes material-specific limitations and requires extra time for the powders to absorb the radiation. Bulk sintering is not energy-efficient and not accurate because it typically requires a high-temperature oven and cannot accurately control the local sintering process on the scale of the powder particles. Therefore, it is beneficial to use an energy source that can directly deliver heat patterns because heat can be absorbed by any material. Direct heat patterns have been utilized for material processing and printing before. Scanning thermal lithography [42] was developed as a maskless lithography technique that uses a scanning thermal probe to pattern photoresist with a submicron resolution. Thermal printing (direct thermal printing or thermal transfer printing), which operates at relatively low temperature (~ 300°C), has long been used in the point-of-sale (POS) printers by applying heat patterns in a contact mode to heat-sensitive papers to print receipts [43]. Selective heat sintering (SHS) [44], which uses a commercial thermal printhead to transfer heat through an 80μm-thick protective thin-film sheet to selectively heat the powder particles. However, due to the low operation temperature of the commercial thermal printhead and the plastic protective sheet, the temperature of the powder

particles can only be raised by a few degrees and the powder bed must be preheated to just a few degrees below the sintering temperature of the powder particles, causing significant energy waste and limiting its potential (especially for high-temperature materials). The second drawback is the exposure timescale. Sintering typically takes place in a few milliseconds in SLS systems when laser or electron beam scan over the powder particles (~100μm) at a speed of ~100mm/s due to the high energy density of laser or electron beam (i.e., each particle get exposure for ~1 ms) [28], while it generally requires much longer exposure time (~1s) for the aforementioned processes that use infrared radiation [38, 45, 46].

2.2 Rapid Sintering in Additive Manufacturing

Most of the technologies covered in the previous sections produce parts by joining powders together into one continuous structure. The mechanism which enables parts to be made from powders is sintering; an understanding of the theory behind sintering as well as common sintered materials used for flexible electronics is required for development of MAPS printing technology.

Sintering is a high-temperature process that causes material particles to join and gradually reduce the pore space between them [47]. During sintering, the powder particles join and the pores between them become nearly spherical and the density of the compact increases [48]. Sintering is frequently used for processing ceramic materials or for powder metallurgy but has also become a popular mechanism to utilize in additive manufacturing of parts in powder bed fusion processes. The four different fusion methods used are solid-state sintering, chemically induced binding, liquid-phase sintering and full melting [30]. Solid-state sintering refers to the joining of particles without melting, which occurs at a temperature between one half of the melting temperature and the melting temperature [30]. Solid-state sintering involves heating the material until particles

form “necks” between each other, which binds them [49]. Chemically induced binding utilizes thermally activated chemical reactions between two powders or between powders and an atmospheric gas to form a by-product which binds the powders together [30]. Liquid phase sintering refers to sintering under conditions where solid grains coexist with a wetting liquid [30, 50]. Liquid phase sintering has applications in automobile engine connecting rods and high-speed metal cutting inserts, among others [51]. Full melting refers to the mechanism of completely melting a powder to join it into a cohesive unit and is a mechanism commonly associated with Powder Bed Fusion (PBF) processing [30].

Powders can be suspended in solution to make ink for the fabrication of flexible electronics. This is done so that the ink can be applied using a printer, so these inks are usually developed as a compromise between printing and sintering capability. The ink is usually deposited by inkjet, screen, flexography or other technique before being cured either in an oven [52] or by using a flash bulb [19, 53, 54]. Inks typically consist of metal nanoparticles or flakes with some solvents and organic content [52, 55]. Nanoparticle inks generally consist of the nanoparticles coated in a capping agent such as Polyvinylpyrrolidone (PVP) suspended in various solvents such as ethylene glycol and ethanol with some organic content. The sintering procedure for these inks consists of first evaporating the solvents from the ink, after which the capping polymer (PVP) which coats the nanoparticles starts to deform as its glass transition temperature is reached; sintering occurs when the nanoparticles are discarded from their capping [56]. Low organic content of the ink is preferred, as sintering a high organic content ink too fast results in delamination from the substrate [57].

The particle size is also a major parameter of the sintering process due to the phenomenon where particles of a smaller size will have a lower melting temperature [2, 5, 6, 7, 8, 9]. This

characteristic of nanoparticles is very exploitable in both solid state sintering and full melting. Buffat has proposed the following equation to determine the melting temperature of nanoparticles [6]:

$$T_m = T_0 * \left(1 - \frac{2}{\rho_s L r}\left[\gamma_s - \gamma_l \left(\frac{\rho_s}{\rho_l}\right)^{2/3}\right]\right) \quad (1)$$

Where ρ is the density, γ is the surface tension, T_0 is the melting temperature of bulk metal, L is the latent heat of fusion, and r is the radius of the nanoparticle. The subscripts s and l denote solid and liquid, respectively. Furthermore, the range of the particle size should be reduced to prevent cracking of the sintered product in the case of inks [2].

Techniques that achieve millisecond-scale sintering of particles are SLS and photonic curing. Material properties that affect SLS include viscosity, surface tension, particle shape and size distribution, absorptivity/reflectivity, thermal conductivity, specific heat, emissivity and the melting temperature [22]. In photonic curing, which is frequently used for flexible electronics, a thin layer of a conductive ink is deposited onto a substrate; then this substrate is moved underneath a flash lamp which emits a high energy light on the order of milliseconds to provide energy to the particles and raise their temperature to an acceptable level for sintering [18, 19, 54]. Schroder quantified the temperature at the surface of the exposed surfaces to be greater than 1000°C, but the temperature is only sustained for 1ms before quickly cooling to well below the working temperature of PET; this prevents damage to the substrate [54].

2.3 Microheaters

As discussed in the previous section, rapid sintering such as photonic curing occurs when powders are exposed to high temperatures exceeding their melting point [54]. MAPS technology

accomplishes this with the use of a microheater array. To make this process successful, the microheater must be able to transfer enough energy to the powders in a very short timescale. This requires the use of microheaters that can reliably operate at temperatures much higher than the sintering temperatures of the powders.

A microheater is a resistive heater with a filament miniaturized to ~100nm to ~100µm with MEMS fabrication techniques. The filaments are generally made of heating materials such as titanium, platinum, molybdenum, tungsten, or polysilicon, to name a few [58, 59, 60, 61, 62]. Characteristics of these thin film microheaters are low power consumption, fast response, good heat confinement, good mechanical stability, and good fabrication yield [58]. Applications for these microheaters include micro-ignition for micro-propulsion systems and micro-explosive boiling [58]. Microheaters have been used in both 2D and 3D printing systems such as inkjet printing [63, 64], thermal printing commonly used in a point-of-sale (POS) printer [65], and selective heat sintering (SHS) [66]. In these printing technologies, the microheater usually operates at around 300°C.

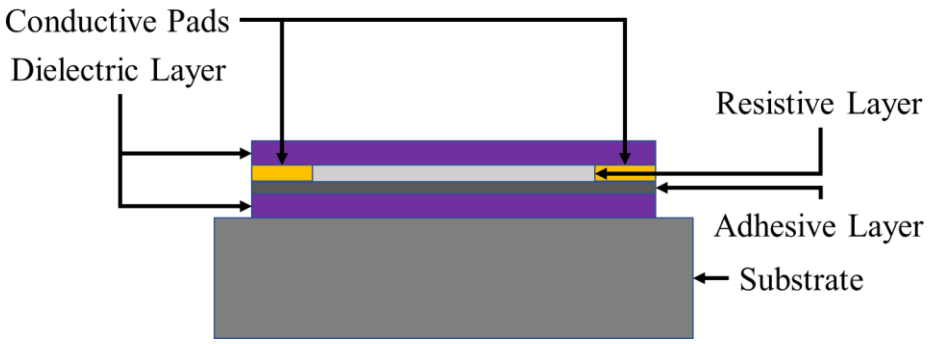

Figure 2 - Typical configuration of a microheater [67].

Microheaters are generally built on a substrate of glass or silicon. Glass is a good choice due to its low thermal conductivity. Silicon has also been used despite its high thermal conductivity due

to its ease of processing with MEMS fabrication. Silicon underneath the microheater can be etched away to leave the microheater on a thin membrane of dielectric material to increase power efficiency [68]. The typical process flow to fabricate a heater using MEMS techniques is to grow a dielectric layer, use photolithography to pattern the substrate then deposit the microheater material and conductive leads using sputtering or e-beam evaporation [69, 70]. Some important considerations in designing microheaters is the heat transfer characteristics, geometry, and thermal response time. Microheaters transfer heat in three modes: conduction, convection and radiation [71]. Of these three modes, the conduction and convection are significant while radiation is insignificant at temperatures less than ~700°C for Ti or Pt microheaters [65, 71, 72]. Numerical simulations have been used to select materials by evaluating maximum temperature and power savings with different insulating layers [59]. Geometries can also be optimized for power savings, reduced stress profiles and even heat distribution [73, 74, 75]. Thermal response time is critical to the operation of a microheater. In previous studies, a thermal response time of 2ms for a temperature of 600°C was achieved with tungsten microheaters with a power consumption of 12mW [61] and a thermal response time of 1ms was achieved with a Pt/Ti heater reaching a temperature of 400°C using only 9mW of power [76].

Since the response time of a microheater is generally very fast, a sophisticated feedback system is required to control the temperature. Proportional-integral-derivative (PID) controls have been effectively used to control the temperature of a microheater [77, 78]. The feedback control for a microheater relies on a phenomenon in which the resistance of a conductor changes with its temperature; thus, the average temperature of some conductor may be determined through its change in resistance [79]. The temperature of the microheater is usually read through the resistance change of an additional metal filament which is near the microheater, rather than by

reading the resistance of the microheater [78, 79], although the resistance change of the microheater has been successfully used for low temperature applications at 200°C [77]; MAPS requires the microheater to operate at a high temperature of at least 400°C and does not have room for additional temperature sensors.

2.4 Gap Control

MAPS requires a high-temperature microheater to sinter powders, and it is also necessary to bring the microheater close to the powders in a repeatable way. If the microheater must scan over the powder, the gap between the microheater and the powder must be maintained during this motion. This dynamic system presents a challenge in the precision of gap control required.

When trying to provide quality gap control for additive manufacturing applications, there are two things that are required, leveling the build plate to maintain that gap across the entire surface and measuring and finding the appropriate gap. There are a few simple techniques for leveling that include adjusting a set of three or four screws and are found on most 3D printers [80]. However, these often rely on imprecise measurement and guess and check methods. To ensure that the build plate is precisely leveled, some measurement will need to occur. Another alternative that researchers have focused on is creating ultra-precise motion stages by eliminating any friction and creating a suspended stage [81]. This train of thought has produced quite a bit of work on magnetically suspended linear motion stages that can move in the X and Y directions while rotating about the Z axis [82] which eventually led into a magnetically suspended platform that could be controlled by all six degrees of freedom within a relatively small travel volume to a nanometer resolution [83]. Another similar technology has been developed, but instead of suspending the entire stage with magnets, they were only used to help orient the stage, although

it was noted that an entirely suspended linear motion stage could be possible [84, 85, 86]. Another group began testing the durability and stability of some of the current linear motion stages by challenging the systems to consistently meet plus or minus one nanometer resolutions while under a static load, which was achievable up to thirty-two Newtons of force [87]. This research certainly reinforced the idea that having multiple stages stacked on top of each other was a reasonable way to achieve multiple degrees of freedom without sacrificing the nanometer precision required.

There are a few different options that can be implemented to accurately measure the gap. Contact sensors have been used for many years in different industries as everything from simple switches to delicate positioning sensors. There are also a variety of non-contact sensors that can be used without the need to physically touch the substrate which could damage it as well as the contact sensors [88]. Capacitive non-contact sensors are relatively common in industry and work by energizing the surface with a high frequency and then measuring the feedback given off by the surface. From this difference, an actual distance can be determined between the measuring plate on the sensor and the surface it is measuring [89]. There are also inductance and laser-based systems that achieve a similar result by measuring the feedback given relative to each method. Recently, hybrid non-contact measurement systems have been developed that allow the system to measure the thickness of a substrate as it is deposited or before it is cured. This combination of inductance and laser-based measurements allows for the measuring of two separate materials at the same time. This could also be achieved with two inductive or capacitive sensors as well as two laser sensors. After taking readings from both sensors, one calibrated to measure the top surface and the other calibrated to measure the bottom surface, a thickness can be determined by comparing the two measurements [90].

There are also a few functional gap control systems that could be utilized in a MAPS printer. Some focus on the process of sensing the gap and accounting for the environmental conditions, particularly in imprint lithography and similar applications [91]. While others focus on how to handle multiple contact points with the substrate and how to compensate for the other points when one makes contact or becomes to close [92]. The key to the above processes is the ability to adapt in real time and with the same expected precision that is required of the process. The culmination of that idea is a multi-stage orientation device designed to maintain a predefined gap with regards to the substrate beneath it [93]. This idea was refined to be implemented in even more precise applications by the addition of a piezoelectric stage as the final moving stage [94].

CHAPTER 3

Microheater Development

To overcome the drawbacks of other powder bed AM and flexible electronic printing processes, we propose to use a high-temperature microheater as the energy source to create and apply a heat pattern directly to the powder particles in a non-contact mode by placing the microheater near the substrate. The microheater will deliver a very high energy density in a few milliseconds for rapid sintering like laser or electron beam but in a scalable design. This section chronicles the design, fabrication, control, and validation of the microheaters used for this new technology.

3.1 Design and Numerical Modeling

Previous research for this new technology has detailed the design of a microheater optimized for MAPS printing [67, 95]. In these works, a microheater was designed which could meet the following specifications:

1. A target temperature of 600°C;
2. A heating and cooling cycle on the timescale of ~1ms;
3. Minimal power consumption.

The microheater geometry was optimized for even heat distribution, as shown in Figure 3. Simulations showed that the microheater could be brought to the target temperature of 600°C in 1ms with a power input of only 1.2W, and the microheater cooled to below 200°C in another 1ms.

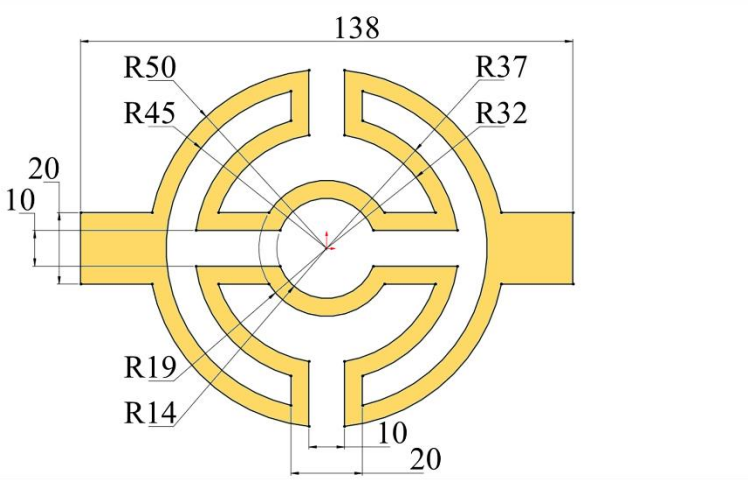

Figure 3 - Dimensions of an optimized microheater (unit: mm) [96].

Some additional work was done to explore the effects of the microheater on a substrate in close proximity: for example, the temperature profile on the substrate and the effect of changing the air gap for a 10ms dwell time (the timescale of exposure to the microheater). However, no results had been reported for the following:

1. Necessary air gap and dwell time for sintering silver nanoparticles
2. Effect of dwell time on print resolution
3. Increasing the air gap by changing the conducting medium

The following sections explore these problems.

3.1.1 Numerical Model

The numerical model of the microheater used in previous research is used again for simulating the printing system [67]. In this study, the microheater is placed over the material being sintered which is placed on top of another glass substrate (or the printing substrate). The heater and the sintering material is separated by an air gap, modeled as a fluid; this air gap is the medium

through which the heat transfer from the heater to the sintered material occurs. An overview of the setup can be seen in Figure 4.

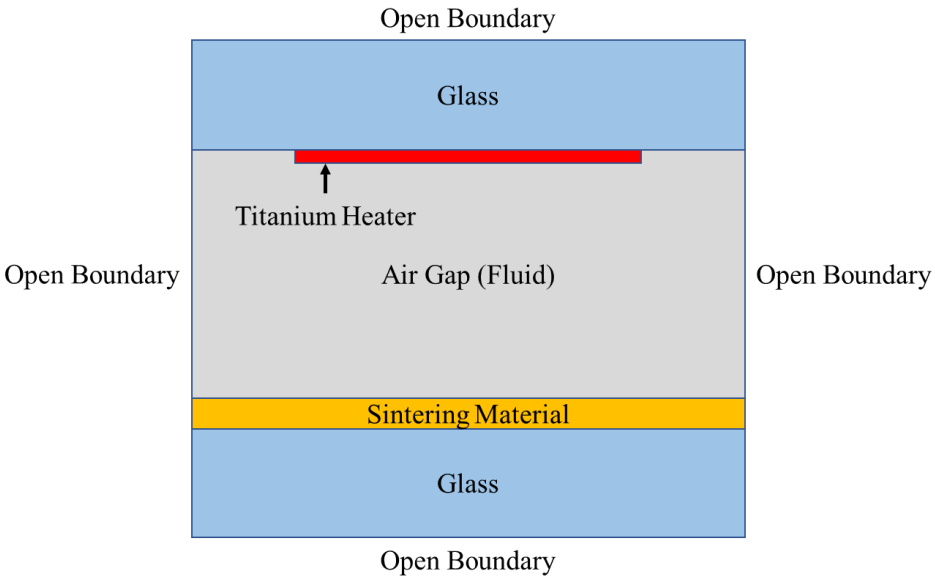

Figure 4 - Modeling setup of MAPS simulations [96].

To simplify the numerical model, open boundaries have been used where boundaries would be continuous. The initial temperature in the simulation is 20°C. Material properties are the same for the microheater part of the simulation. Air has material properties that are temperature dependent, which are modeled based on known relationships [97]. The printing substrate is Pyrex 7740 glass. The additional material properties used at room temperature are in Table 1 [67].

Table 1 - Properties of materials used in numerical study [96].

Summary	Pyrex-7740	Air
Electrical Resistivity (Ω*m)	1.26E+06	-
Thermal Conductivity (W/m*K)	1.18	.0257 or >
Specific Heat (J/kg*K)	753.12	1.005 or >
Density (kg/m^3)	2230	1.225 or >
Temperature Coefficient of Resistance (1/K)	-	-
Young's Modulus (Pa)	1.16E+11	-
Poisson's ratio (1)	0.321	-
Thermal Expansion Coefficient (1/K)	8.60E-06	-
Function	Substrate	Conducting Medium
Thickness (μm)	550	0 to 50

For these simulations, silver nanoparticles are used as the material to be sintered, such as the dried silver nanoparticles offered by NanoComposix [98]. Typically, powder bed processes use micron scale powders (10s of microns diameter), but as will be revealed in later sections, the air gap must be maintained at a sub-micron scale. The surface roughness of the powder layer will depend on the size of the powder particles, which implies that larger particles will lead to an air gap that is on the order of the powder particle size. It is for this reason that nanoparticles will be used: nanoparticles will offer a relatively smooth top surface, and the layer thickness can be kept to a low 1μm with a surface roughness on the order of ~10s of nanometers. NanoComposix offers this powder in various sizes, but for our study we will focus on a particle size of 50nm. The objective of this simulation is to numerically validate that the resistive heating source previously designed can provide adequate heat to elevate the temperature of the powder to sintering temperature.

Modeling the thermal conductivity of the powder particles is an essential aspect of accurate prediction. In these simulations, we will model the powder particles as a combination of densely populated nanoparticles and air. Thus, the powders can be treated as a bulk thin film material

with an effective bulk thermal conductivity as a function of temperature, as shown in Equation 2 [67]:

$$k(T) = 0.0006T + 0.245 \quad (2)$$

Next, the size of the air gap must be determined. In the previous research, it was shown that an increase in the air gap by only a few microns dramatically lowers the temperature on the surface of the powder layer [67]. Because of this, a smaller air gap is desired to decrease the amount of time required to heat the powder layer to an acceptable level. For the following simulations, an air gap of 2μm is used.

3.1.2 Sintering of Silver Nanoparticles

A target temperature must be determined that will be sufficient to sinter the silver nanoparticles. Per NovaCentrix (a supplier of silver nanoparticle ink), it is required to sinter some silver nanoparticles inks with a particle size of 50nm at 250°C for 10 minutes [52]. To achieve our objective of millisecond sintering, the sintering temperature needs to be significantly higher. In laser sintering processes, a laser power and scanning speed are chosen to accomplish millisecond sintering: the combination affects the Gaussian distribution of temperature at the location of the laser scan in the horizontal plane [23, 99]. The temperature of the powder below the surface dramatically drops with increased depth [23, 99, 100], but this is irrespective of the method of heating the surface of the powders. In this regard, there is not a major difference between the MAPS process and SLS: MAPS will apply this heating pattern directly via the air gap while SLS applies this heating pattern via radiation. The surface temperature is the most important indicator for sintering to occur. Once the critical surface temperature is reached, the diffusion or partial

melting will occur on the surface to fuse the powder particles together even though the temperature in the powder bed may still be low.

In our simulations, we will monitor the surface temperature of the powder layer to determine the state of the powder regarding sintering. Peng et al has achieved sintering of silver nanoparticles in 1ms using SLS which was found to be at 440°C [101]. In this simulation, we have achieved a temperature of 440°C in 12ms as shown in Figure 5. Although sintering may be achieved before this time, we have shown that our system can achieve a temperature deemed necessary for millisecond scale sintering by previous works.

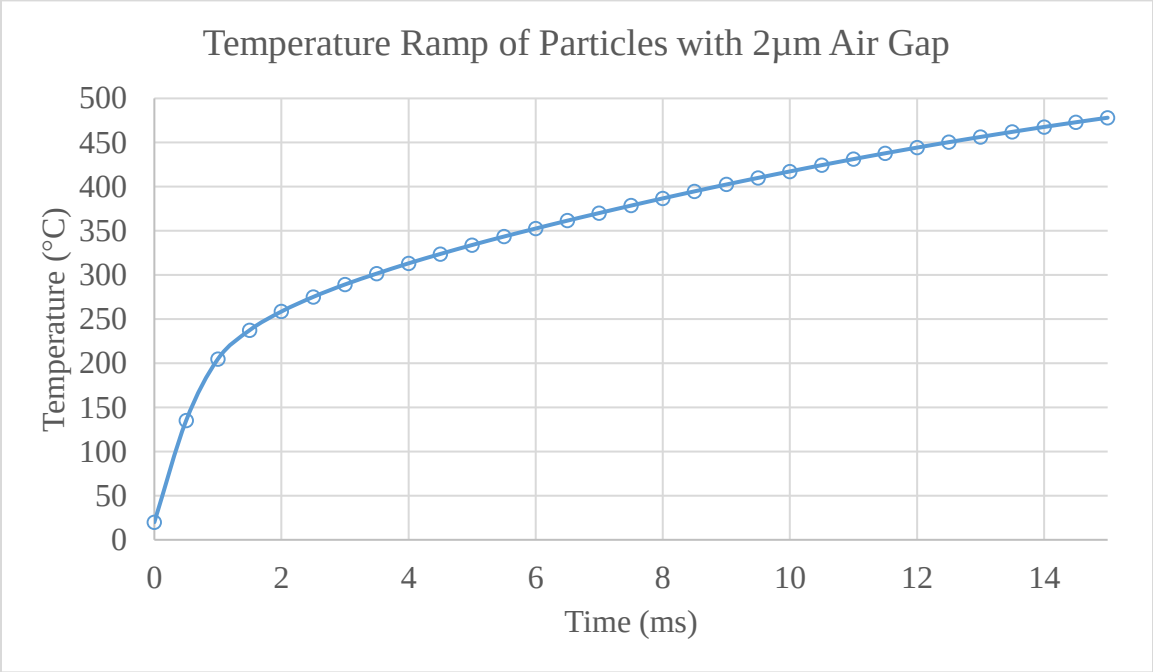

Figure 5 - Maximum temperature experienced at the surface of the silver nanoparticles [96].

3.1.3 Effect of Dwell Time on Resolution

Another parameter to determine was the printing resolution. This was evaluated by observing the temperature distribution on the surface of the nanoparticles. The temperature was sampled every

5µm on the surface of silver nanoparticles along the centerline of the microheater as illustrated in Figure 6 by the dotted line labeled x-axis and extending 50µm outside the heater.

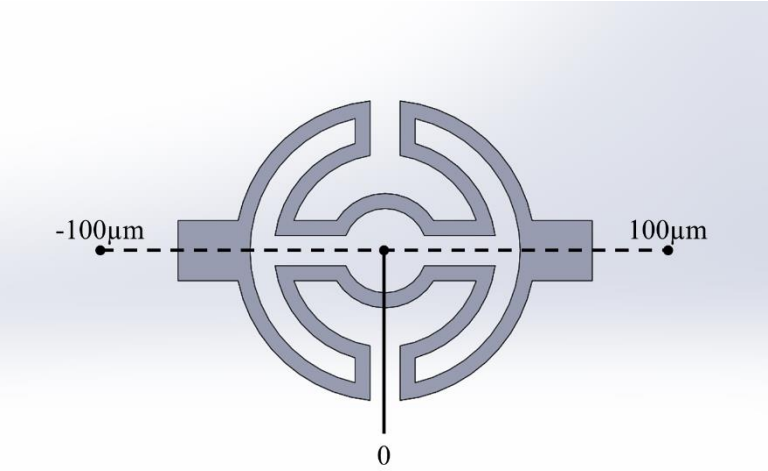

Figure 6 - Line sampled for temperature plot to show resolution [96].

It is observed that there is a sharp decline in the temperature beyond 50µm in either direction from the center of the microheater. The dwell time can be changed to increase or decrease the temperature over this area. The dwell time could be adjusted to accommodate another material with a different required sintering temperature or to achieve a different printing resolution; this is illustrated in Figure 7. It was established previously that a temperature of 440°C is needed for fast sintering of the silver nanoparticles, so in our case a 100µm resolution can be achieved by setting the dwell time to be 14ms.

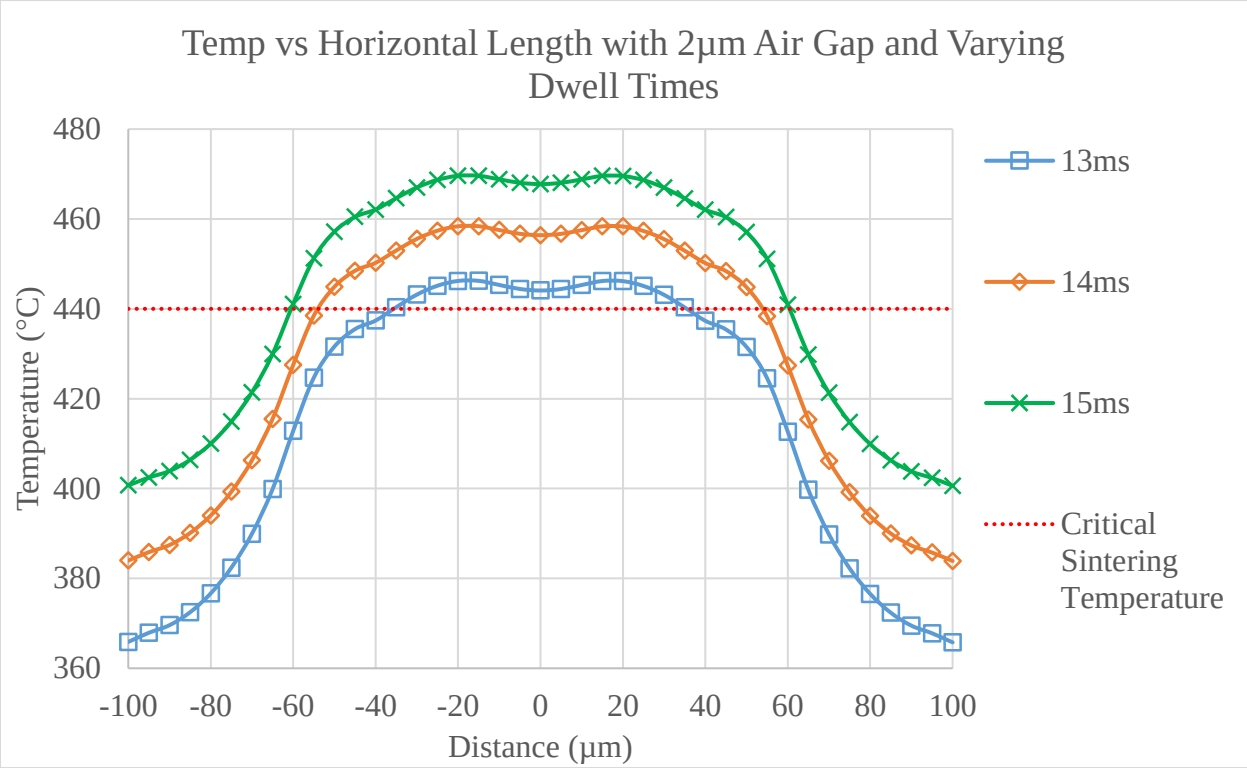

Figure 7 - Temperature of the material underneath the microheater to show resolution. The horizontal line represents a critical sintering temperature of 440°C above which any powder will be sintered. For dwell times of 13, 14 and 15ms, a resolution of 70, 100 and 120µm is achieved, respectively [96].

3.1.4 Increasing Air Gap

One limiting factor of this technology is the requirement of a small air gap (a few microns), which necessitates a more complex printing system which increases the cost and excludes the use of larger powder particles, as mentioned in Section 3.1.1. Increasing the air gap to ~100µm would significantly reduce the design and manufacturing complexity of the printing system and allow the use of most commercial powders (most of the existing powders have a particle size less than 100µm).

There are two different approaches to increase the air gap. One is to use a medium with higher thermal conductivity in the air gap and the other is the increase the microheater temperature.

Helium has a thermal conductivity roughly an order of magnitude greater than that of air (0.142 W/(m*K) VS 0.024 W/(m*K)), which if used as a conducting medium allows us to increase the air gap by an order of magnitude (from 2µm to 20µm). Using an induction plasma, which would potentially have a higher thermal conductivity by an order of magnitude than normal helium, could allow us to increase it even further to ~100s of microns. Another method to increase the air gap would be to increase the temperature of the microheater. Some platinum microheaters can be operated at temperatures up to 800°C, and Tungsten microheaters can be operated at temperatures up to 1200°C [60]. One side benefit of increasing microheater temperature is that the thermal conductivity of gas increases with higher temperature. For example, the thermal conductivity of air increases to 0.08 W/(m*K) at 1000°C, which is almost four times that of room temperature due to the higher degree of ionization at high temperature. By combining a microheater capable of higher temperatures with a more suitable conducting medium, the air gap can be increased to ~100s µm.

Figure 8 illustrates the air gap that can be achieved by changing the conducting medium to helium and increasing the temperature of the microheater. By only changing the conducting medium to helium, a 20µm gap is achieved, and increasing the operating temperature of the microheater to 1000°C allows us to increase the gap even further to 100µm without significantly increasing the sintering time.

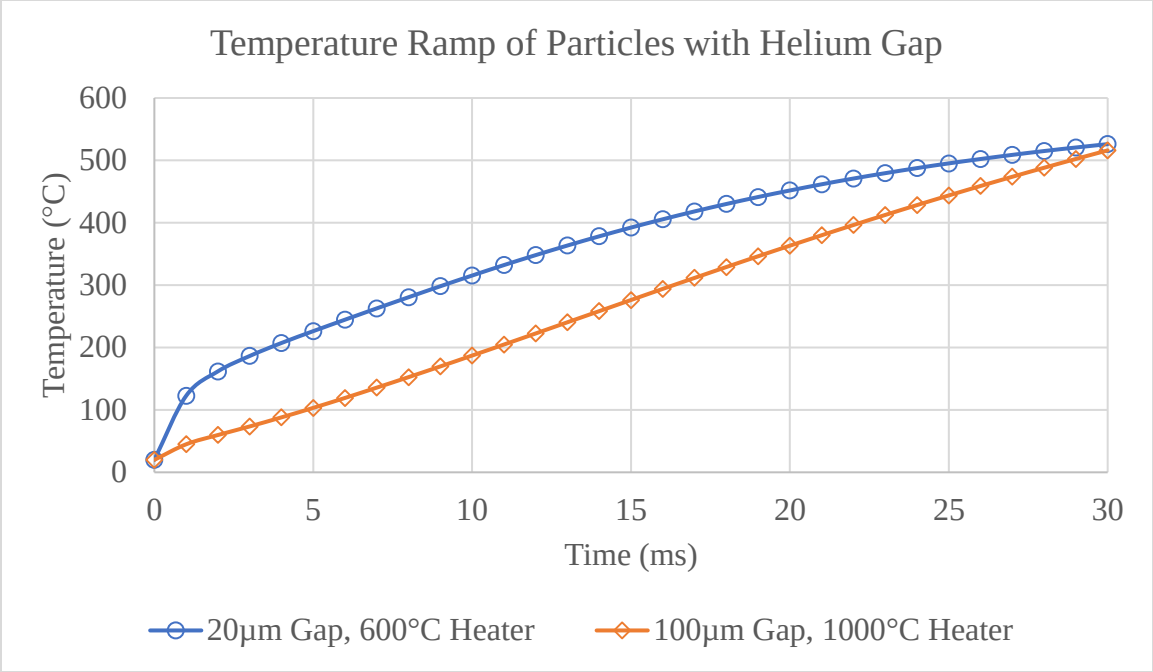

Figure 8 - Temperature ramp of the surface of the powder particles with modified conducting medium and microheater operating temperatures [96].

A couple of side effects are noted when we increase the air gap. One is that a longer heating time is needed to ramp up the powder temperature to the same target temperature (e.g., a heating time of 20ms is needed for a 100µm air gap as opposed to 14ms for the 2µm airgap as shown in the previous simulations). In addition, when increasing the air gap, the temperature gradient along the surface of the particles is affected, which in turn influences the printing resolution. Figure 9 shows the comparison of the temperature profiles on the powder surface between an air gap of 20µm and 2µm. The intuition is that there is a balance between the heat source temperature, the speed, and the time of the heat transfer for minimizing the heating time and printing resolution. Therefore, these side effects can be alleviated by optimizing the heater geometry (e.g., such that the temperature is higher in the center of the microheater and lower on the edge) and the input electrical current, which will be left for future research.

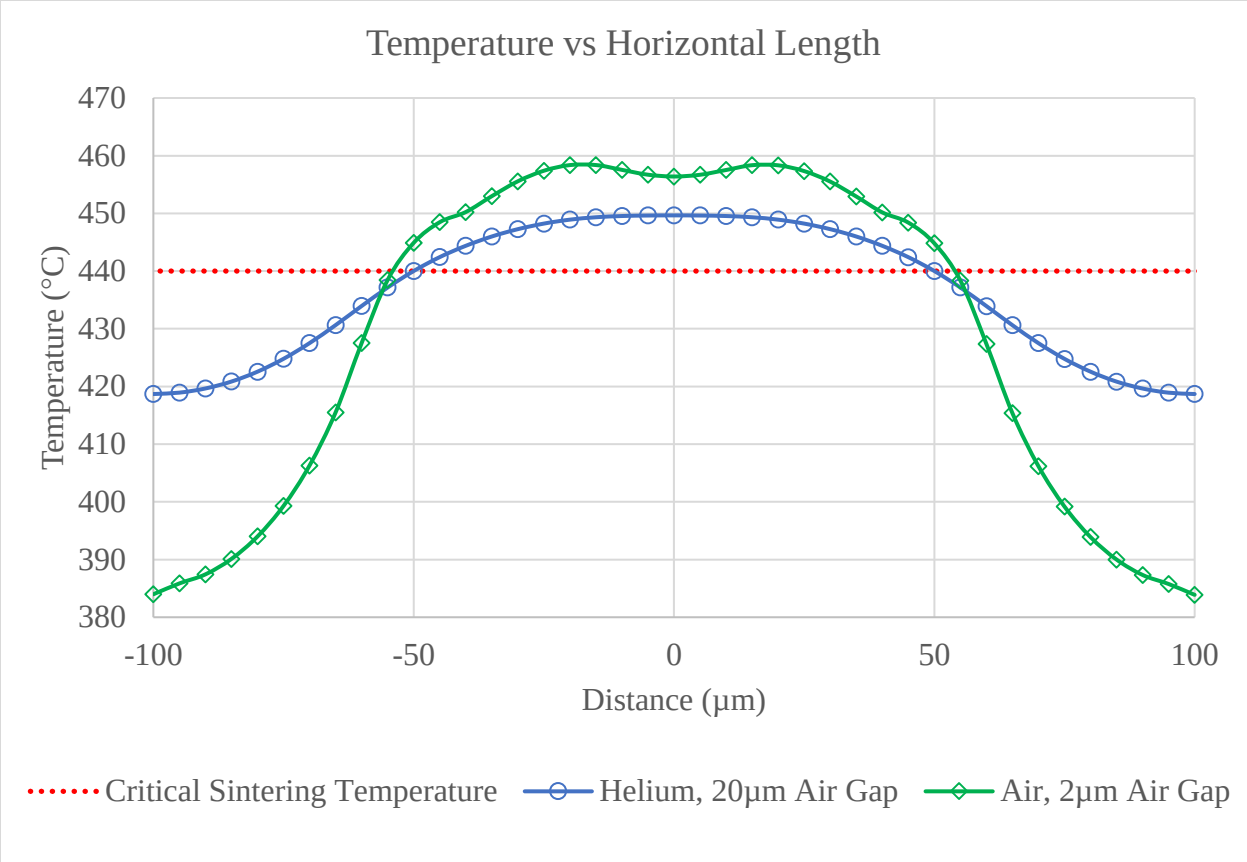

Figure 9 - Illustration of the effects of increasing air gap. Both curves are taken at a dwell time which achieves a 100µm resolution, but the temperature profile along the powder layer becomes flat as the air gap is increased [96].

3.2 Microheater Fabrication

This section is built on the previous sections which proposed a microheater with the following criteria: a maximum temperature of 600°C with a response time of 1ms [67].

3.2.1 Microheater Die Design

Platinum was chosen as the filament material due to its oxidation resistance and ability to reach the target temperature, and Schott's AF 32 eco glass wafer was chosen as a substrate due to its low thermal conductivity and high glass transition temperature of 717°C [67, 102]. As higher temperature microheaters are developed, different substrates may be used. For example, Sapphire

and Langasite have much higher working temperatures and thus may be used for future microheater designs [103, 104]. The microheater from previous sections was scaled to a 2 x 2 array, as can be seen in Figure 10(a).

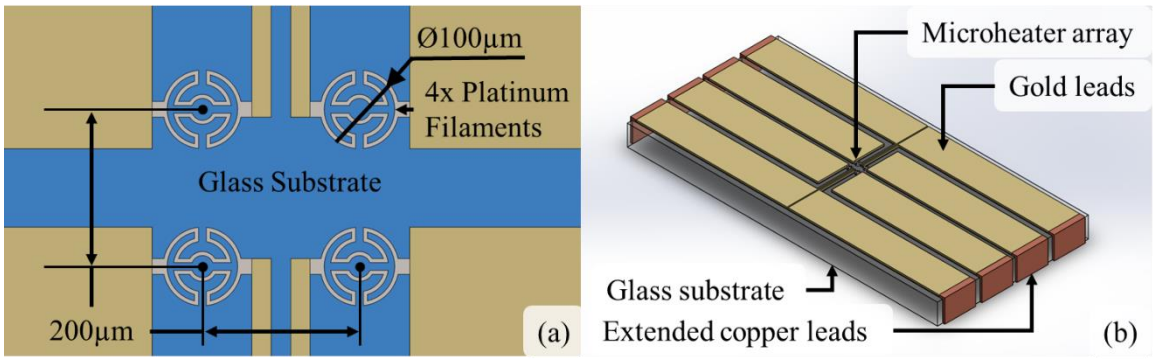

Figure 10 - (a) Design of a microheater array with evaporated gold leads; (b) 3D Model of microheater die with leads evaporated onto the sides. This enables electrical connections to the side of the die, allowing the heaters to approach close proximity to a substrate [20].

One critical design aspect of the microheater die used for MAPS is that the microheater must be able to approach the substrate to a gap of only a few microns. This makes it necessary to eliminate any wire bonding or other electrical connections that may protrude out of the surface of the microheater die. One approach is to connect the microheater to the external control circuit from the other side of the die, which can be done using a glass wafer with through-vias as illustrated in Figure 1, such as that offered by Schott [105], which can be an ideal solution for mass production. Since only small batches of microheater dies are required, it is sufficient to evaporate conductive copper leads along the sides of the die to enable electrical connections as shown in Figure 10(b).

3.2.2 Microheater Die Fabrication

The die described above was manufactured using MEMS fabrication techniques. Photolithography followed by sputtering was used to deposit the microheater filaments and e-beam evaporation was used to deposit the conductive leads. A more detailed description of the fabrication process is described below and shown in Figure 11.

1. A 500µm thick AF 32 eco glass wafer from Schott Inc. was used.
2. The wafer was cleaned using acetone and isopropyl alcohol, then rinsed with DI water and dried.
3. AZ 5214-E photoresist was spin coated to a thickness of 2µm and prebaked.
4. UV photolithography was performed using the microheater mask, followed by post-baking and a second blanket exposure.
5. The photoresist was etched using AZ MIF 300 developer.
6. 100Å of tantalum (adhesion layer) followed by 1500Å of platinum (heater filaments) was deposited by sputtering.
7. Lift-off of the photoresist and metal layer was achieved using acetone in an ultrasonic bath.
8. A second photolithography stage identical to that previously mentioned was used to pattern the wafer using the leads mask.
9. E-Beam evaporation was used to deposit 100Å of titanium followed by 1000Å of gold.
10. Lift-off of the photoresist and metal layer was achieved using acetone in an ultrasonic bath.
11. The dies were cut using a dicing saw such that the gold leads extended to the edge of the die.

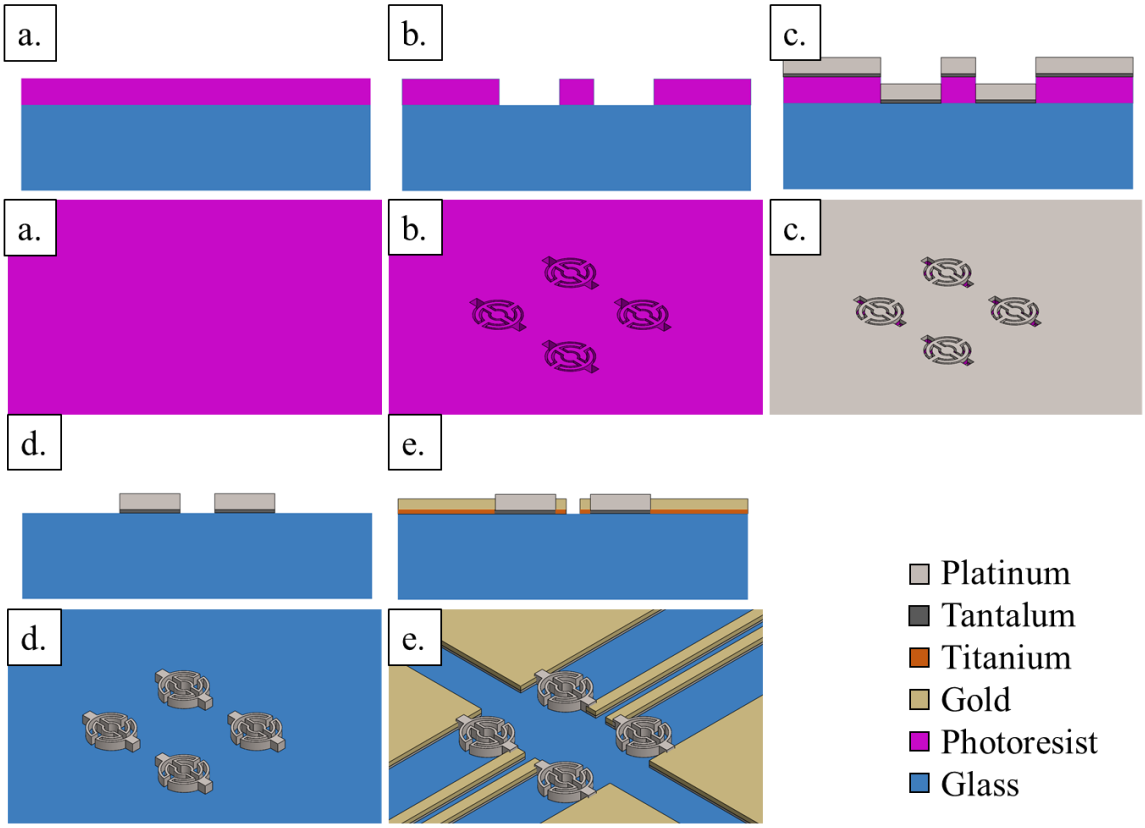

Figure 11 - 2D and 3D representations of the fabrication steps of the microheater array: (a). the glass wafer is coated with a layer of photoresist; (b). the photoresist is exposed using the microheater mask and etched; (c). an adhesion layer of Ta followed by Pt filaments are deposited; (d). the photoresist is removed using acetone; (e). an adhesion layer of Ti followed by Au leads are deposited using the same procedure in steps (a) – (d) [20].

After the heaters are deposited onto the glass substrate, the wafer is diced into the individual heater dies, consisting of four microheaters each with two leads. After dicing, it is possible to fabricate the extended leads, which are deposited via e-beam evaporation. The leads consist of an adhesion layer of titanium, followed by a layer of copper and finally a layer of tin, which is included to protect the copper from oxidation. The extended leads are fabricated onto these dies using the following steps, as shown in Figure 12:

1. Kapton tape was used to mask the sides of the dies in between each of the leads and to mask the top of the die where the microheaters are to avoid shorts between the leads.
2. The dies were put into a fixture to tilt them at a 45° angle such that both the side and top of the dies are exposed during evaporation.
3. E-beam evaporation was used to deposit 100Å of titanium followed by 1000Å of copper and finally another 100Å of tin to extend the leads to the sides of the die.

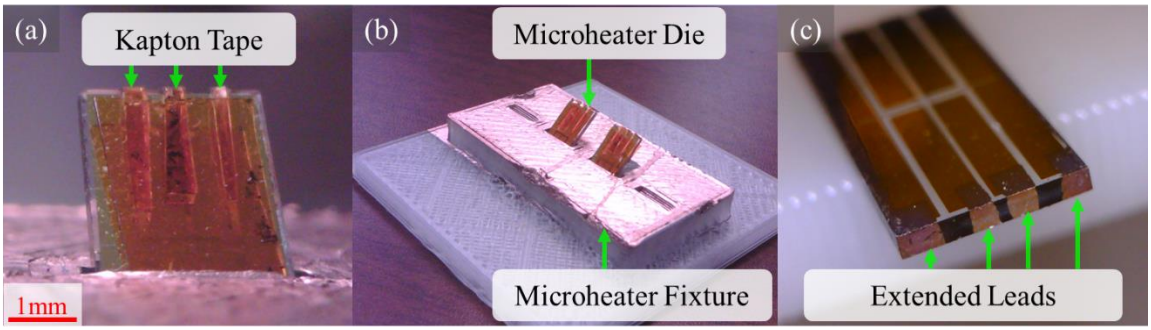

Figure 12 - Fabrication steps to extend leads. a. thin strips of Kapton tape are placed in between the leads and on top of the microheater array, b. the microheater dies are fixed at a 45° angle, c. extended copper leads are evaporated onto the top and sides of the microheater die [20].

3.2.3 Microheater Packaging

The packaging of the microheater is an integral part to the success of MAPS. The packaging must accomplish the following tasks:

1. Provide fixture of the heater die to the rest of the printer assembly;
2. Provide a method of electrical connection to the heaters;
3. Allow the microheaters to approach a flat substrate to a distance of ~2µm.

To satisfy these requirements, a basic Quad Flat No-leads (QFN) package was devised for the microheater die. The package is a two-layer printed circuit board (PCB) with an FR4 substrate, purple mask over bare copper, and ENIG finish.

The extended side leads of the microheater die are bonded directly onto the conductive pads on the packaging using a silver epoxy – this allows for both electrical connection and a method of attachment between the die and the packaging. EPO-Tek® P1011 silver epoxy [106] was used to bond the heater die to the packaging using the following steps:

1. The microheater die is attached to the package using Kapton tape such that the leads on the die are aligned with the contact pads of the package.
2. The epoxy is manually applied using a needle such that it connects the individual leads to the contact pads.
3. A weight is placed on top of the die to ensure it stays in place, and the package is loaded into a vacuum oven to bake at 150°C for one hour to cure the epoxy.
4. The package is removed from the vacuum oven and the Kapton tape is removed. The finished packaging of the microheater die is shown in Figure 13.

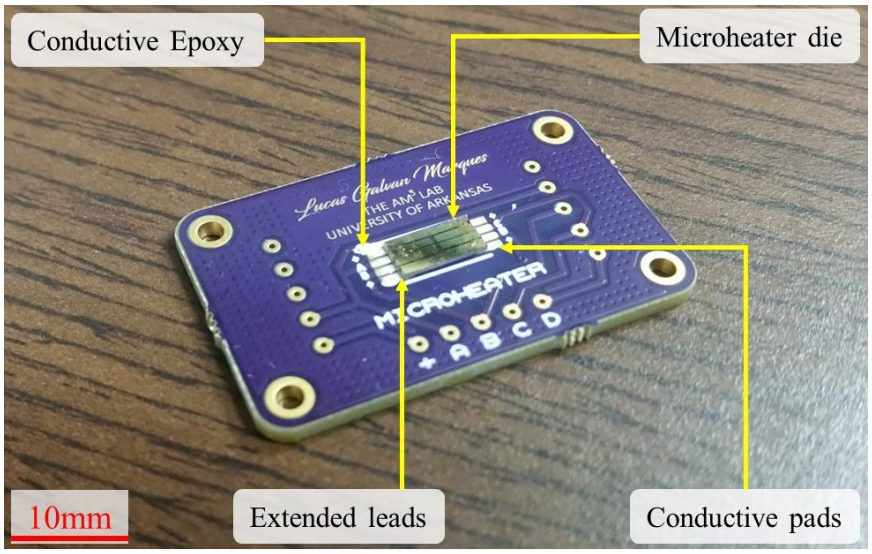

Figure 13 - Finished microheater packaging with electrical connections and attachment accomplished with conductive epoxy [20].

3.3 Microheater Control

For MAPS, it is important to have precise control of the temperature of the microheater. Ideally, the microheater should ramp to its target temperature of 600°C in 1ms and be maintained at that temperature until sintering is complete. It is also critical that the temperature of the microheater does not too far exceed the target temperature or else there is a risk of damaging the microheater. Because of these requirements, a sophisticated feedback control is needed.

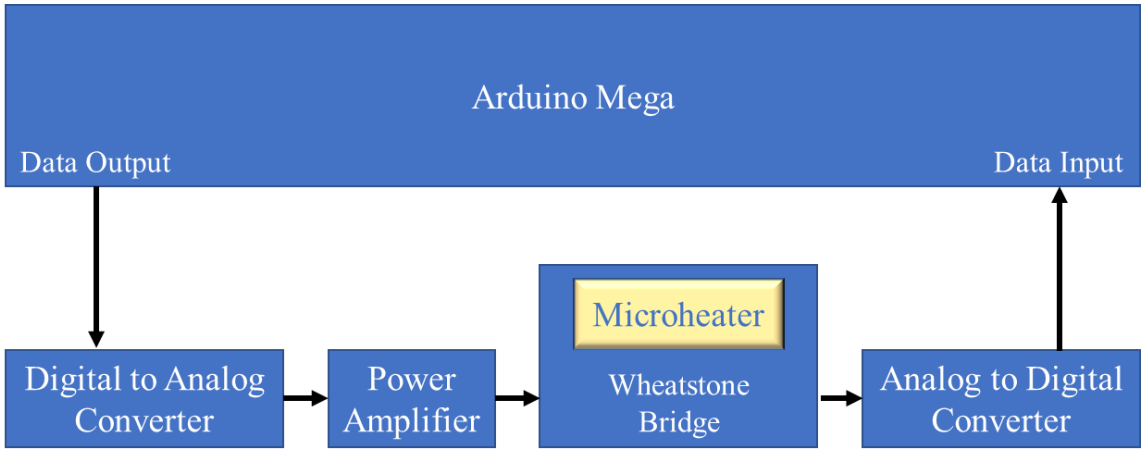

Figure 14 - Block diagram of the microheater control unit [20].

The microheater temperature is maintained by a PID controller, a closed-loop control based on the temperature-resistivity relation of the microheater. Figure 14 illustrates the control loop of the microheater temperature. All data is processed by an 8-bit microcontroller board Arduino Mega. Arduino Mega generates an 8-bit data output which is converted to an analog voltage between 0 and 10 volts by a Digital to Analog Converter (DAC). The signal goes through the power amplifier to ensure that enough power will be delivered to the Wheatstone bridge where the microheater is connected. The voltage difference in the Wheatstone bridge between the Point A and Point B (Figure 15) is converted by the Analog to Digital Converter (ADC) and sent back to the Arduino Mega where the resistance of the Microheater is calculated. Based on the

temperature-resistance relation, the temperature of the microheater is calculated and the control voltage output is updated to keep the microheater temperature around the target temperature.

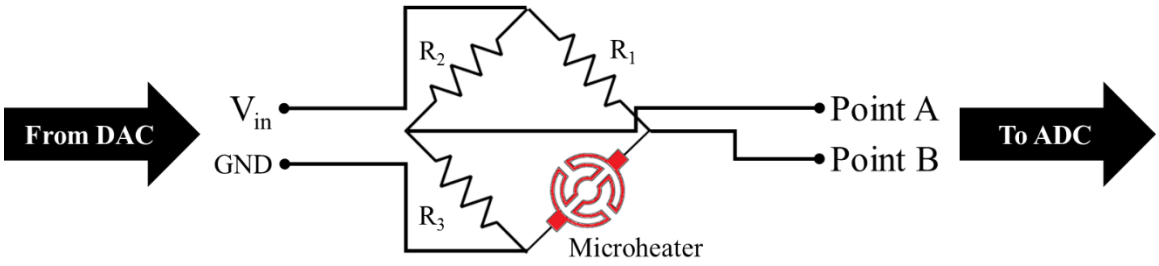

Figure 15 - Microheater connected in the Wheatstone bridge [20].

The microheater resistance R_m is calculated using three known resistors in the Wheatstone bridge as shown in Equation 3 [20].

$$R_m = \left(\frac{R_2 * R_3 + \left(R_3 * (R_1 + R_2) * \frac{\text{ADC Voltage}}{\text{DAC Voltage}} \right)}{R_1 - \left((R_1 + R_2) * \frac{\text{ADC Voltage}}{\text{DAC Voltage}} \right)} \right) \quad (3)$$

3.4 Microheater Validation

To use the circuit described in Section 3.3, it is first required to determine the relationship between temperature and resistance of the microheater. This was accomplished by loading the microheater into a furnace with a thermocouple and recording the resistance of the microheater at various temperatures. Platinum's resistance changes linearly with changes in temperature [107], so a linear line of best fit was applied to the acquired data. The result of this test is shown in Figure 16.

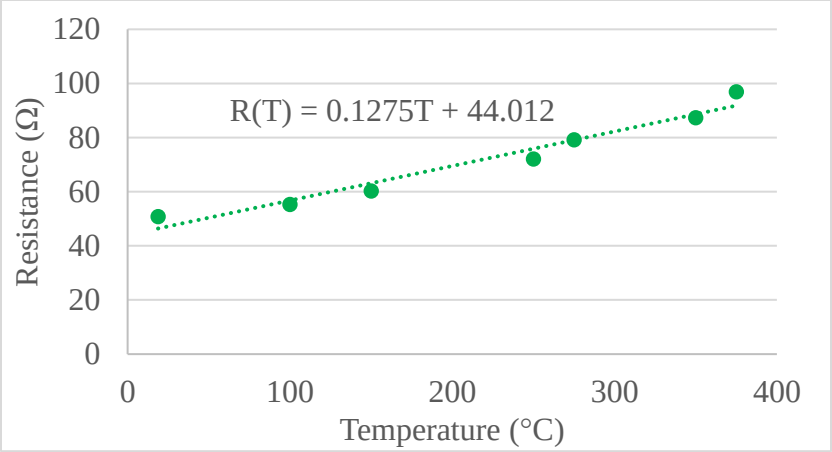

Figure 16 - The resistance of the Pt microheater as a function of temperature [20].

For validation, a temperature control circuit was made on a PCB onto which the microheater package was connected, as shown in Figure 17.

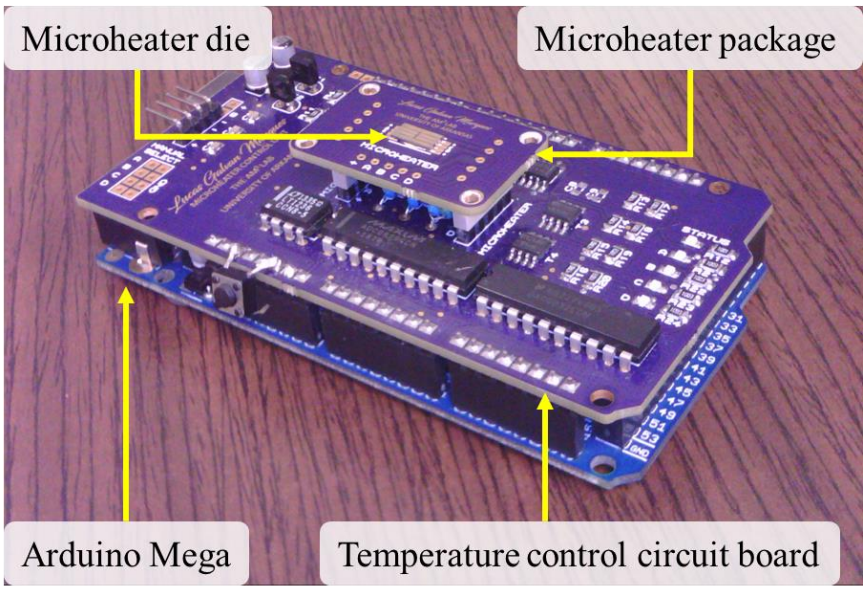

Figure 17 - Microheater package mounted to control board [20].

To validate the function of the controller, a single microheater was activated and its temperature was calculated using the temperature-resistance relationship shown in Figure 16: the resistance of the microheater was found by measuring the DAC and ADC voltages as shown in Figure 15

and then calculating using Equation 3. This was accomplished with only a maximum of 1.2W power consumption. The change of temperature and power consumption over time are shown in Figure 18. It shows the designed circuit can effectively raise and maintain the microheater temperature to the target temperature in the desired timescale.

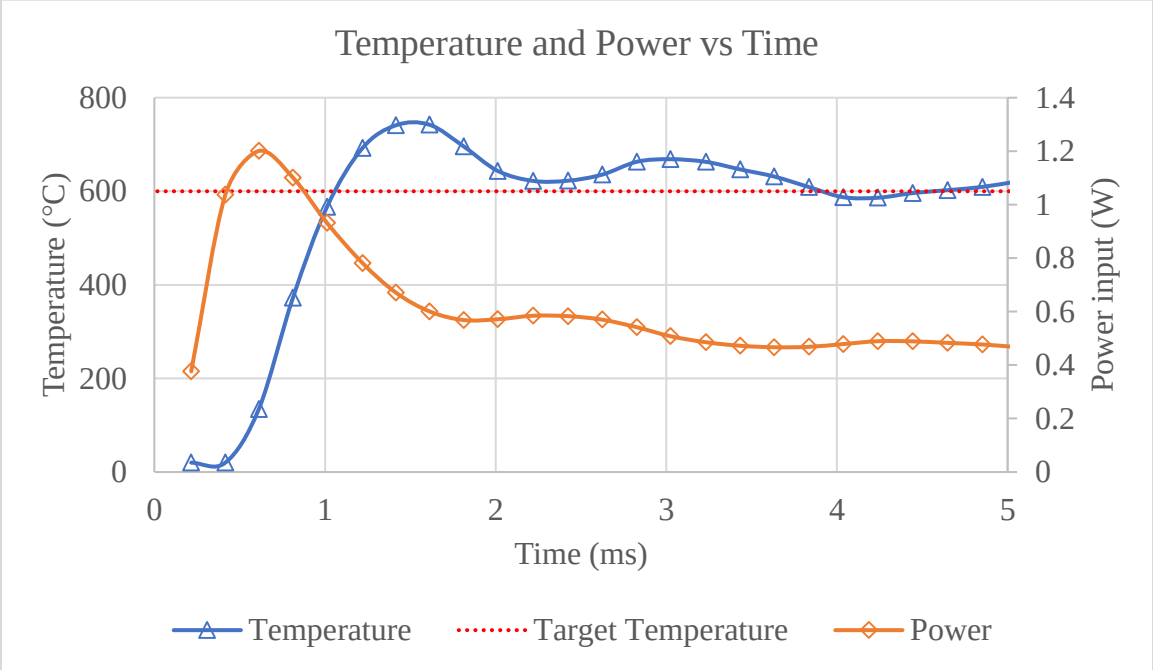

Figure 18 - Pt microheater being heated to a target temperature of 600C in 1ms [20].

Additionally, because the microheater will be turned on and off to selectively sinter powder particles, it was desired to determine a cycling frequency for the microheater operation for the MAPS process. For this test, the microheater was heated to the target temperature of 600°C then allowed to cool until reaching room temperature by natural cooling (i.e., no assistive cooling mechanism is used) at which point it is ramped up again, etc. The results of this test are shown in Figure 19. It shows the designed microheater and temperature control circuit can meet the requirements of the MAPS process to quickly turn on and off to reach the target temperature in a couple of milliseconds.

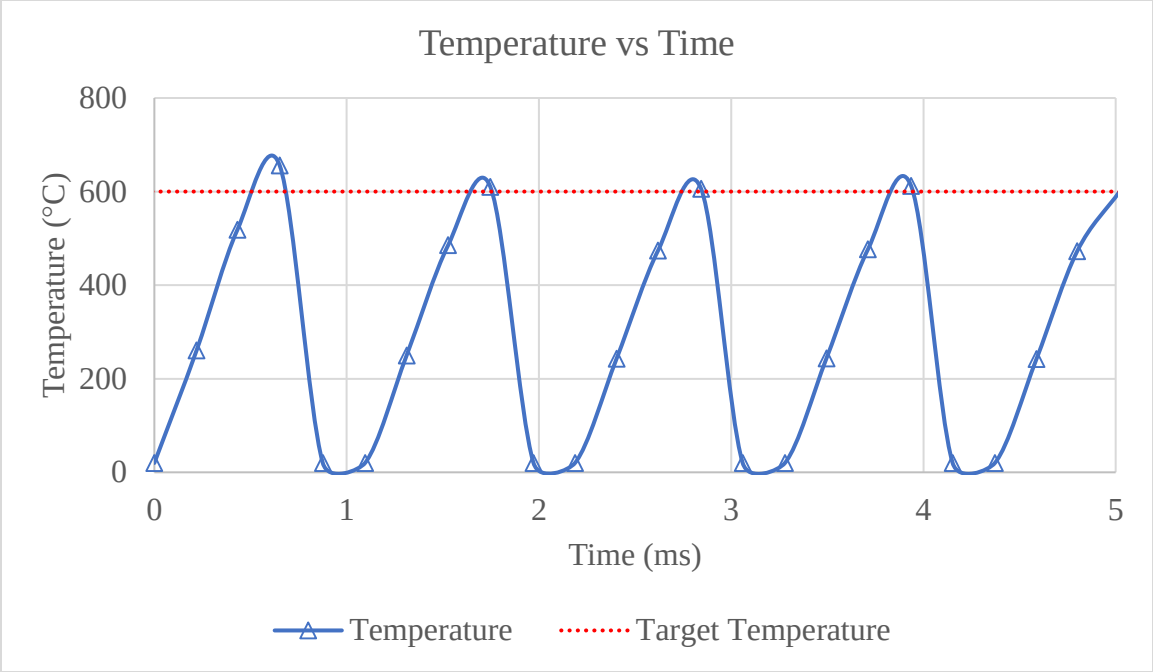

Figure 19 - Cycling the Pt heater on and off resulted in a response time of less than 1ms to heat up and cool down between the target operating and room temperatures [20].

CHAPTER 4

Experimental Proof of Concept

In the previous chapter, the MAPS process was studied with extensive simulations and a microheater array required for MAPS printing was developed. This chapter presents the design and construction of an experimental proof of concept which is used to print conductive lines with silver nanoparticle ink onto a plastic substrate. The conductive line is analyzed, and the MAPS process is compared to other printing methods. Results show that MAPS performs on par with or better than the existing fabrication methods for printed electronics in terms of both the quality (conductivity of the printed line) and speed, which shows great promise of MAPS as a competitive new method for digital production of printed electronics.

4.1 Design

MAPS is a relatively simple system which can conceptually be reduced to the following elements as illustrated in Figure 20:

1. A microheater (or array of microheaters) capable of reaching a temperature necessary for sintering;
2. A gap between the microheater and sintering layer filled with a conducting medium such as air;
3. A method to move the substrate horizontally relative to the microheater without affecting the air gap.

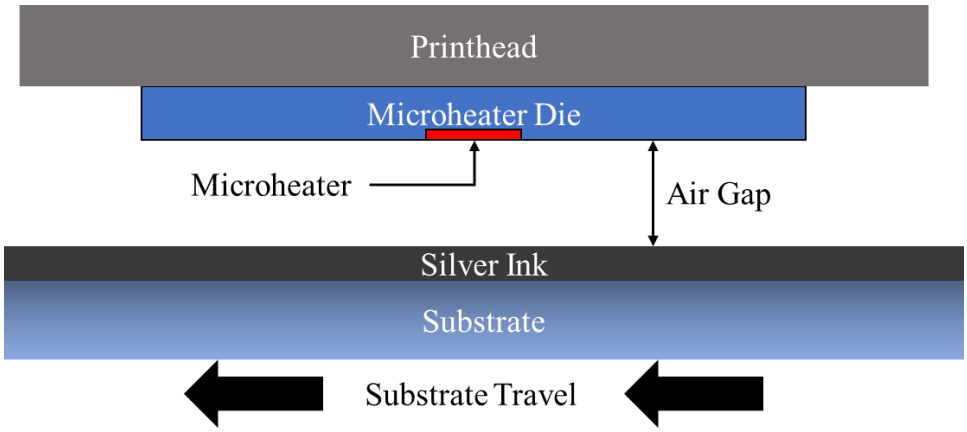

Figure 20 - Illustration of the parameters of the MAPS printing process: a microheater die must be precisely suspended over an ink layer as they move relative to each other [108].

To implement the experimental setup, the following design requirements are established:

1. A 50mm x 100mm printing area: this printing area is decided as a trade-off between printing capability and cost.

2. An automated mechanism to move the substrate relative to the microheater: motion between the microheater and substrate must be allowed in a digitally controlled manner for consistent patterning to occur.

3. An air gap of 5µm ± 3µm between the microheater and the layer of conductive ink must be established: too large of an air gap will undermine the sintering of the nanoparticles, while too small of an air gap risks contact between the microheater and substrate.

4. Parallelism between the microheater die and the substrate must be established and maintained over the printing area: this is necessary to achieve a consistent air gap.

4.2 Experimental Setup

A system was designed to meet the design requirements as shown in Figure 21: it consists of a motorized stage onto which the substrate is placed. Over this stage, the microheater is attached to

a stationary printhead, which allows precise adjustment of the airgap and keeps the microheater in place during the motion of the substrate underneath.

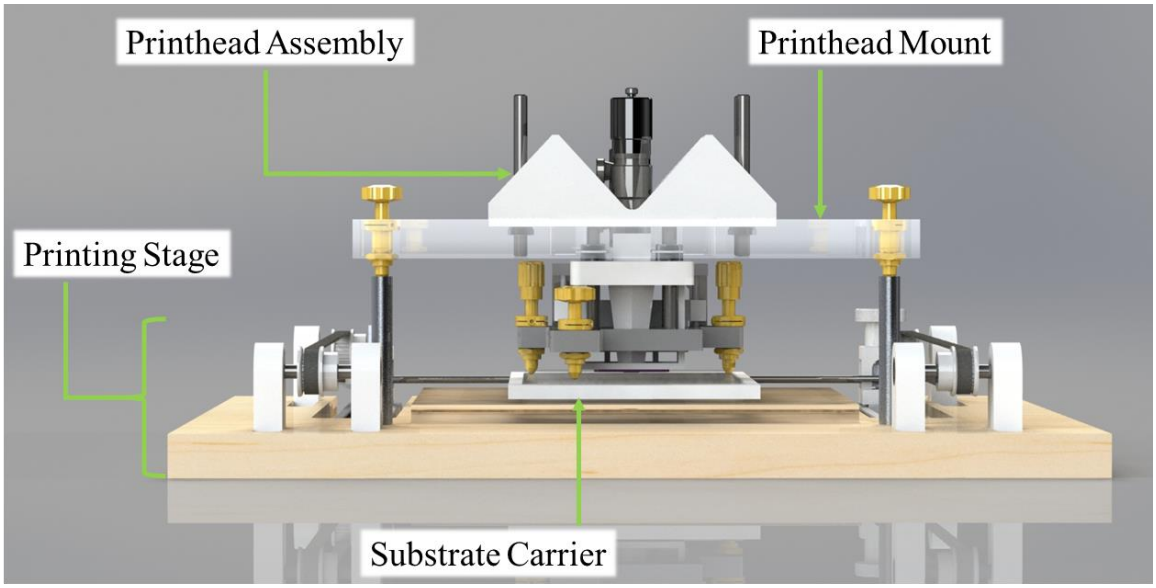

Figure 21 - Overview of printer assembly: the substrate carrier can support a film 100mm wide and has a range of motion of 50mm, fulfilling requirement 1; the substrate carrier is enabled by a stepper motor, fulfilling requirement 2; the microheater die's vertical position and level is adjustable using features of the printhead, fulfilling requirement 3 and 4 [108].

In the following sections, a more detailed analysis of the individual components will be presented.

4.2.1 Microheater Package

For this printer, the microheater was only scaled to a small 2 x 2 array as reported in Section 3.2. The microheater array can be scaled further to encompass the full width of the entire printing area so that circuits can be made in a single pass. The microheater array is fabricated onto a glass die and is attached to a PCB package for digital control as shown in Figure 13.

4.2.2 Printhead Assembly

The printhead consists of a linear motion carriage onto which the microheater packaging is mounted. The linear motion carriage is used to adjust the vertical position of the microheater array with a WGP-13 nanoprecision adjustment micrometer from OptoSigma [109]. The level of the microheater can be adjusted by manipulating three supports, which are AJS127-0.5 nanoprecision adjustment screws available from Newport [110]. A model of the printhead can be seen in Figure 22.

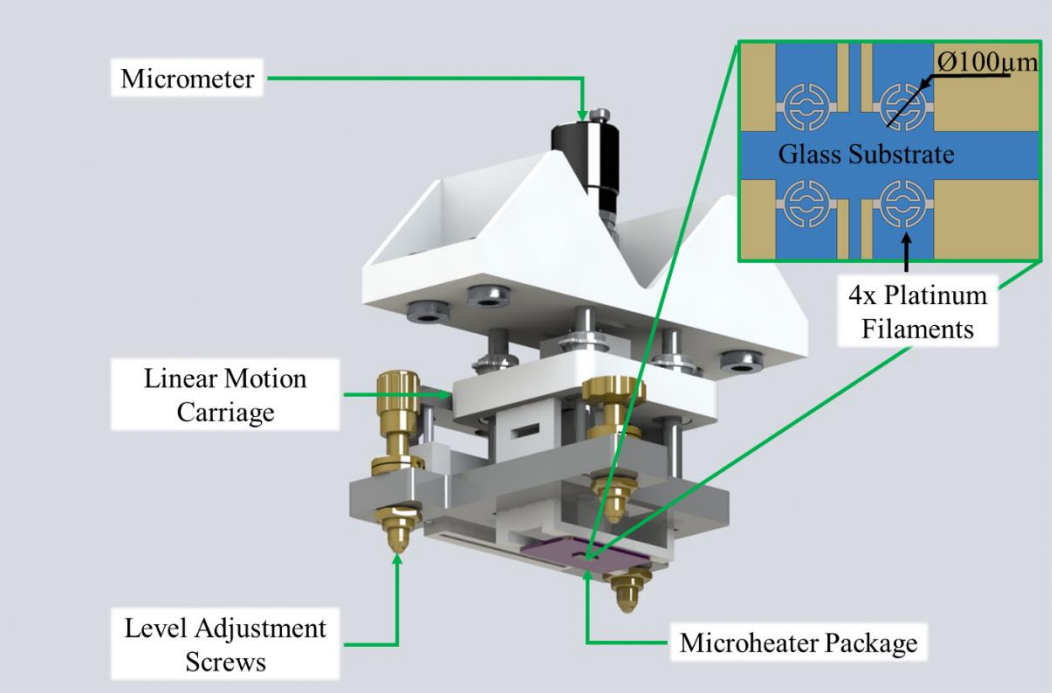

Figure 22 - Model of the printhead assembly: precise positioning and leveling of the microheater, which is mounted to a linear motion carriage, is achieved with the micrometer and level adjustment screws [108].

The printhead assembly for this system serves the following purposes:

1. It suspends the microheater over the substrate: the microheater is attached to the bottom of the printhead, which remains stationary during printer operation.
2. It provides a mechanism for leveling the microheater die by means of the adjustment screws which act as supports.
3. It provides a mechanism for adjusting the air gap by adjusting the height of the microheater die with a micrometer.

4.2.3 Printing Stage

A system to move the substrate underneath the microheater is required. A simple stage was designed that allows motion along the horizontal plane. The printing stage consists of two thick sheets of glass: a carrier onto which the substrate is placed and a stationary base glass on top of which the substrate carrier slides. This motion is enabled by a system of timing belts and automated in one axis by a NEMA 17 stepper motor KL17H248-25-4A from Automation Technology [111]. These components are mounted onto a base which is constructed of particle board.

During operation, the substrate is placed on top of the substrate carrier. Then, the printhead assembly is placed over the substrate. The stepper motor then slides the substrate carrier so that it moves relative to the printhead assembly at a speed specified by the user.

4.2.4 Printhead Mount

The printhead mount consists of an acrylic sheet which is suspended over the stage. It has four linear motion shafts which match the linear motion bearings in the printhead assembly. Because the printhead is not suspended over the printing stage but instead rests directly on top of the substrate, the printhead mount must only hold the printhead assembly in place during operation. The interface allows the printhead to rest on the substrate rather than be suspended and ensure the parallism between the microheater and the substrate, which is illustrated in Figure 23.

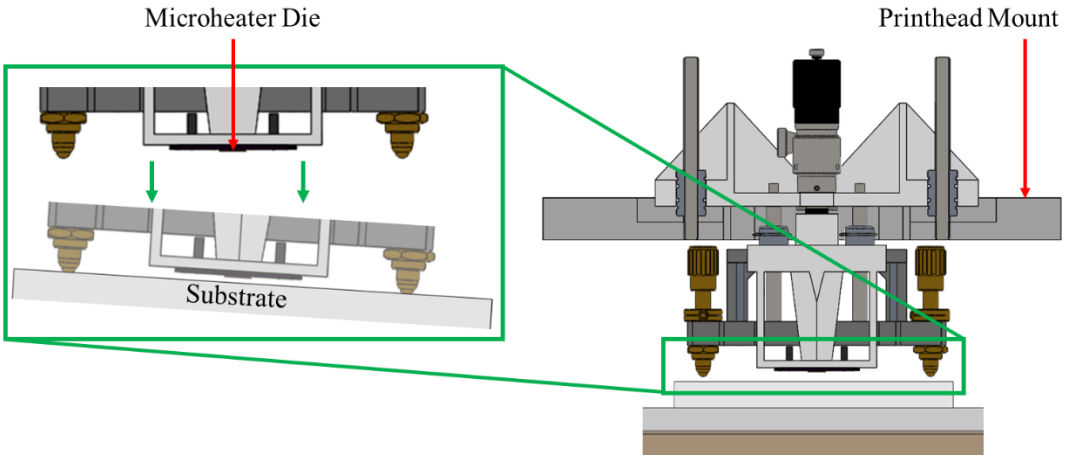

Figure 23 – Illustration of the interface between the printhead and the substrate. By allowing the printhead to rest directly on top of the substrate rather than be suspended over it, the position and orientation of the microheater relative to the substrate can be controlled more easily [108].

4.3 Air Gap Analysis

Airgap control is critical to successful printing with MAPS. For the experimental setup, it was desired to obtain an air gap of 5 ± 3µm to achieve best printing results based on simulations. There are a few functional precision gap control systems that could be utilized in a MAPS machine. One is to use capacitive sensors. Capacitive non-contact sensors are relatively common in industry and work by energizing the sensor surface with a high frequency and then measuring the feedback given off by the surface to determine the air gap down to nanometer precision [89].

Typical commercial capacitive sensors are available with resolutions as low as 0.55nm [112]. Ganjeh et al have parallelized two flat plates to within 0.15nm using interferometric-spatial-phase-imaging (ISPI) as a detector with a piezoelectric stage for adjustment [113]. Some other methods focus on the process of sensing the gap and accounting for the environmental conditions, particularly in imprint lithography and similar applications which rely on nanometer precision of airgap control [91].

These methods are all very effective at solving the air gap issue, but implementation can be very expensive. For our system, a low-cost method was desired. Successful implementation of our low-cost air gap control involved careful evaluation of the materials used to build the printer, fine adjustment tools used to change the position of the microheater die, and a contact sensing system which has been shown effective in establishing nanometer scale air gaps [113].

4.3.1 Contact Sensor

A simple contact sensor was fabricated from a flat silicon wafer by depositing a 150nm thick film of tin onto the polished surface as shown in Figure 24. To use the contact plate to establish the “zero” air gap position of the microheater, it is placed underneath the printhead assembly: the flat surface of the contact plate acts in place of the substrate. Then, the microheater can be lowered and the electrical connection can be checked between the contact plate and the conductive leads of the microheater die. For this purpose, a simple electrical circuit was devised which turns on an LED bulb once contact is made. Once the desired air gap is established, the printhead can be transferred to the substrate and will maintain the air gap.

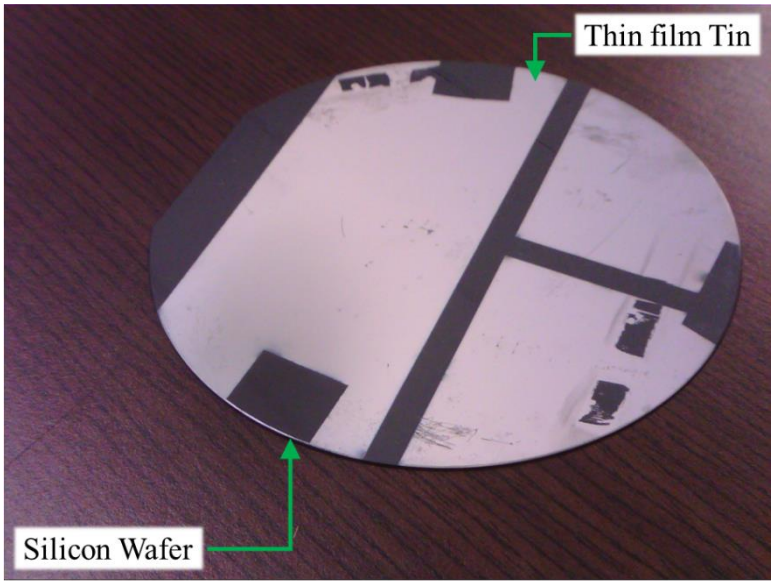

Figure 24 - The contact plate used to establish the air gap. A 150nm thin film of tin was deposited onto the polished surface of a silicon wafer to create the contact plate [108].

The steps for using the contact plate are listed below:

1. The contact plate is placed underneath the printhead, on top of the substrate carrier;
2. The microheater is lowered until the LED turns on;
3. The microheater is raised to the desired air gap.

4.3.2 Air Gap Tolerance

Once the air gap is established between the face of the microheater die and the ink layer, it can be affected by several factors as illustrated in Figure 25: parallelism, the flatness of each surface, the roughness of each surface, and the deflection of components onto which the surfaces mount. It was necessary to carefully examine each of these factors to obtain our target air gap.

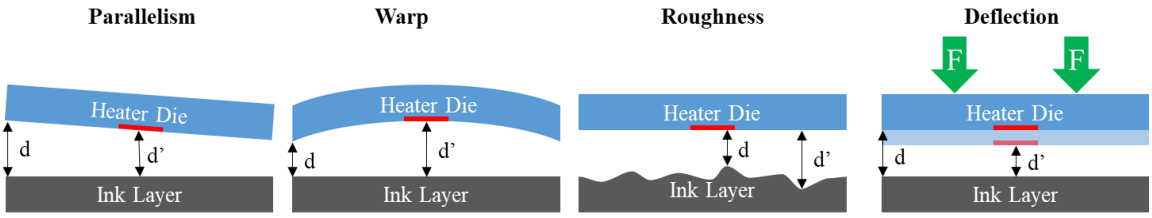

Figure 25 – Four factors which can affect the tolerance of the air gap between the heater die and the ink layer: the variable d represents the desired air gap while d' represents the actual air gap after accounting for any one factor [108].

4.3.3 Parallelism

An analysis of parallelism is concerned with how the microheater die can be suspended over the substrate. To make two planar surfaces parallel, it is necessary to have very fine control of the relative tilt angles and the distance between the surfaces. As was discussed in Section 4.2.2, the face of the microheater die is adjusted relative to a reference plane made with the three printhead supports as seen in Figure 26. The three printhead supports are adjusted by fine screws such that only a 25° turn results in the corresponding corner being vertically displaced by 1μm. We use a contact sensor to determine the vertical displacement of the microheater die with respect to the reference plane; similarly, the tilt of the microheater can be dialed in by using a contact sensor on each corner of the microheater die; both methods have proven effective in previous research to establish nanometer scale gaps [113].

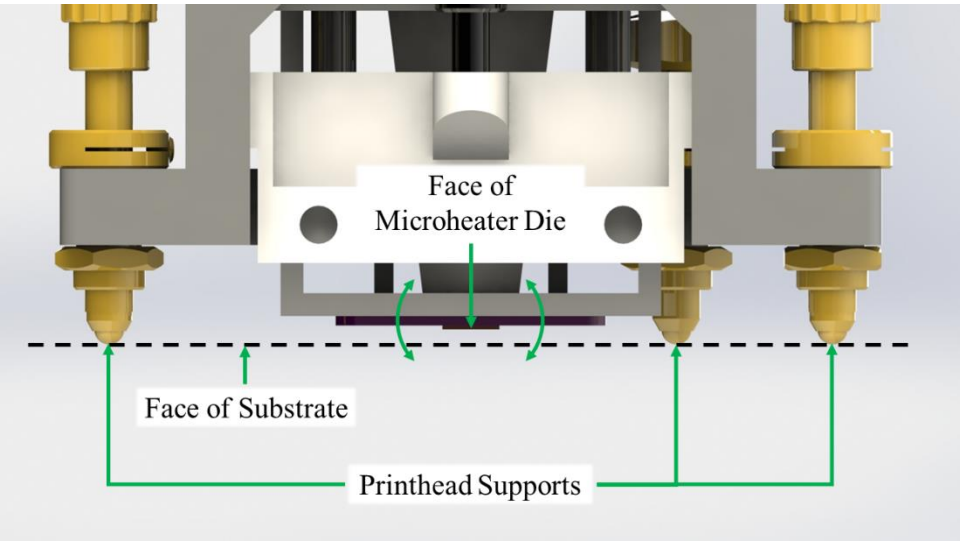

Figure 26 - Illustration of the method of adjusting the tilt of the microheater to achieve parallelism between the microheater die and substrate [108].

4.3.4 Flatness and Total Thickness Variation

The flatness of both the microheater surface and the ink layer surface needs to be considered. The microheater array was fabricated on a 100mm x 0.5mm thick AF 32 eco glass wafer from Schott; the specifications for Schott's wafers show that the warp over the width of the wafer is less than 200µm [114]; this value can be used to calculate the flatness error over the length of the microheater die by using chord geometry as shown in Equation 4:

$$R = \frac{\left(\frac{d}{2}\right)^2 + h^2}{2h} = \frac{\left(\frac{d'}{2}\right)^2 + h'^2}{2h'} \tag{4}$$

Where R is the radius of curvature of a surface, d and d' are the length of the total surface and section of surface investigated respectively, and h and h' are the amount of warp experienced by the surface and section of surface investigated respectively. For a warp of 200µm over a 100mm wafer, the warp experienced over a 7mm heater die made from this wafer is less than 1µm. This relationship is clarified in Figure 27.

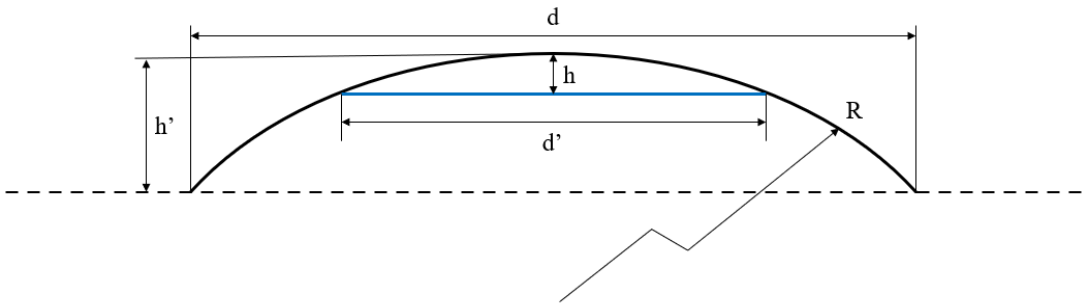

Figure 27 - Illustration of warp experienced in a wafer. The values of 100mm and 200µm are used for d and h respectively, then a value of 6250.5mm is obtained for R. This value and the known value of d', 7mm, can be used to solve for h', which is 1µm [108].

The ink layer is deposited on a flexible substrate which is placed onto a glass substrate carrier, so the flatness of the substrate carrier must be considered. An optical flat was used to determine the flatness of the substrate carrier to be ~500nm.

The only property to consider of the substrate is its Total Thickness Variation, or TTV, which is the difference between the thickest and thinnest portion of the film. This property of the plastic film was tested by sampling the thickness of the film at various points using a micro-gauge over a granite table and was confirmed to be less than 1µm as shown in Figure 28.

Y \ X	0 cm	2.5 cm	5 cm
0 cm	127 µm	127 µm	127 µm
2 cm	126 µm	126 µm	126 µm
4 cm	126 µm	126 µm	126 µm
6 cm	126 µm	126 µm	126 µm
8 cm	126 µm	126 µm	126 µm
10 cm	126 µm	126 µm	126 µm

Figure 28 - Experimental setup to determine TTV of the plastic film and test results. The values for X and Y describe the position of the measurement while the values in the table represent the thickness at that location [108].

4.3.5 Surface Roughness

During printing, the ink layer is deposited onto the surface of the substrate by screen printing: the surface roughness must be considered. To determine the surface roughness of the screen-printed ink layer, ink was deposited on the plastic film and cured in an oven so that the film could be examined using a profilometer. It was found that the surface roughness was 120nm RMS. The surface roughness of the glass used for the microheater die should also be considered: it is specified as < 0.8nm RMS, which is negligible since it is several orders of magnitude less than the desired air gap.

4.3.6 Deflection

Finally, deflection of the system should be accounted for. A finite element simulation was conducted to determine the amount of vertical displacement the microheater die would

experience during normal operation. Simulations showed a vertical displacement of the microheater die of 0.09µm as seen in Figure 29.

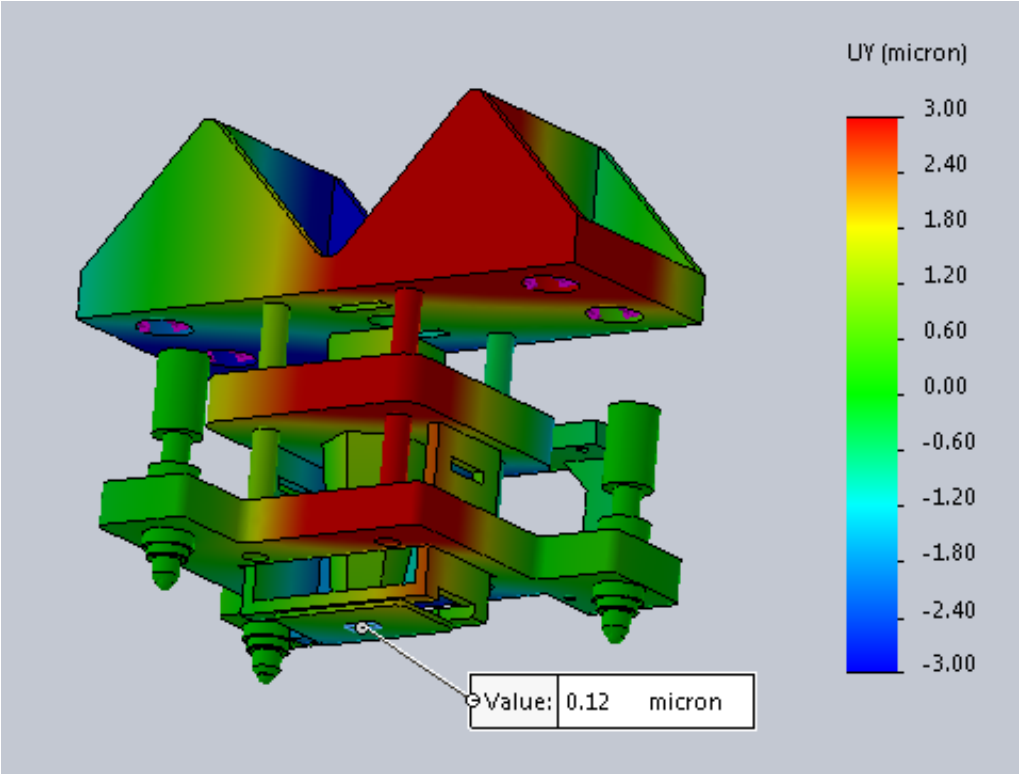

Figure 29 - Solidworks simulation of the printhead while under load during printing [108].

4.3.7 Air gap tolerance

The factors outlined in this section were considered in determining that an air gap can be maintained within the 3µm error, as shown in Table 2.

Table 2 - Tolerance analysis results for the air gap achievable by this experimental setup [108].

Source	Contribution to Air Gap Error
Warp (Heater Die)	< 1µm
Roughness (Heater Die)	< 0.8nm RMS
Substrate TTV	< 1µm
Substrate Carrier Flatness	~ 500nm
Ink Layer Roughness	120nm RMS
Deflection	< 0.1 µm
Total	± < 3µm

4.4 Printing Test

With the experimental setup from the previous sections built, a test consisting of printing a conductive line onto a flexible substrate will be performed. We will first describe the substrate used in this system, then outline the operating steps and show a printed line. Finally, the printed line will be analyzed, and its quality will be discussed relative to other established methods of printing flexible electronics.

4.4.1 Substrate and Printing Material

It is necessary to obtain a suitable substrate and sintering material to carry out the tests. We use Melinex ST505 film from Tekra, which is a heat stabilized PET (HS-PET) plastic film [115]. The ink used must be a typical ink used in manufacturing of flexible electronics: therefore, a silver nanoparticle ink is used. The ink used is Novacentrix's PSI-211 nanoparticle screen printing ink, which has an average particle size of less than 100nm [116], which is similar to what was used in simulations in our previous research.

The HS-PET substrate was cut into 170mm x 225mm sections and a uniform layer of the screen printing ink was spread using an AMI MSP-485 automatic screen printer with a fine 500TPI mesh without a mask [117].

4.4.2 Experimental Procedures

The following steps were taken to perform the tests:

1. The contact plate is used as described in Section 4.3.1 to establish an air gap of 5µm;
2. The contact plate is removed and the substrate with the layer of ink as described in Section 4.4.1 is placed on the substrate carrier;
3. The printhead is lowered onto the substrate;
4. A single microheater is brought to a temperature of 600°C using PID control;
5. The stepper motor is used to move the substrate relative to the printhead at a constant speed of 7mm/s;
6. After the stage moves 50mm, the motor and microheater are deactivated and the substrate removed;
7. The substrate is cleaned using isopropyl alcohol and a soft cloth to remove any uncured ink.

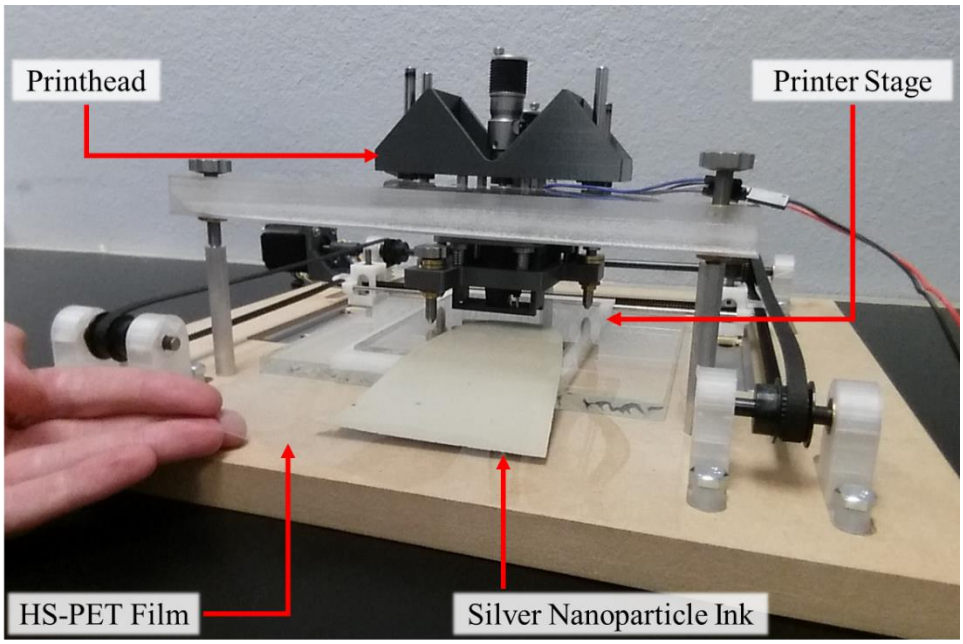

Figure 30 - The film with the deposited silver ink is placed onto the substrate carrier to enable printing [108].

4.4.3 Results

Several conductive lines were printed on the HS-PET substrate. A profilometer was used to determine the cross-sectional area of the line, the results of which can be seen in Figure 31.

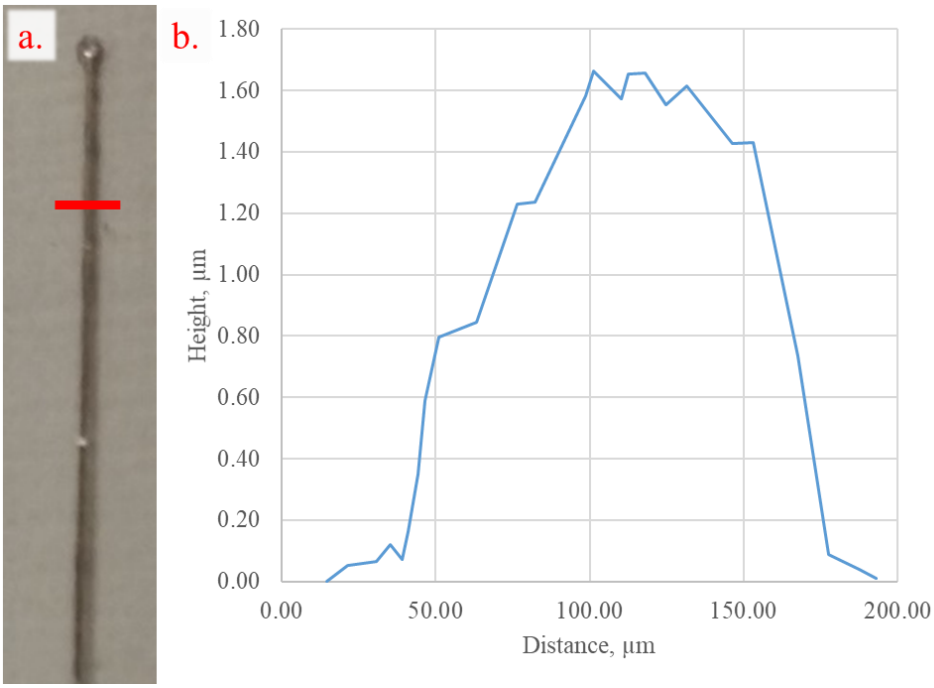

Figure 31 - a. Section of a printed line: the red line indicates the profilometer path and b. Profile of the conductive line printed using the MAPS printing method [108].

The overall width of the line is ~135µm. The width of the line is affected by the printing speed: for example, to produce a slimmer line, a faster printing speed could be used. In this way, we could experimentally validate the results from Section 3.1.3.

The cross-sectional area of the line and the resistance along the line was used to find the average resistivity, which was found to be 10.9µΩ*cm (15% of the conductivity of bulk silver). To further characterize this result, the conductive line was viewed under SEM microscope to determine if sintering had taken place, as shown in Figure 32. There are clear signs that parts of the silver nanoparticles were melted and re-solidified. This is because the microheater, when

operating at 600°C, can heat the silver nanoparticles to ~440°C, which is sufficient to melt the silver nanoparticles [101].

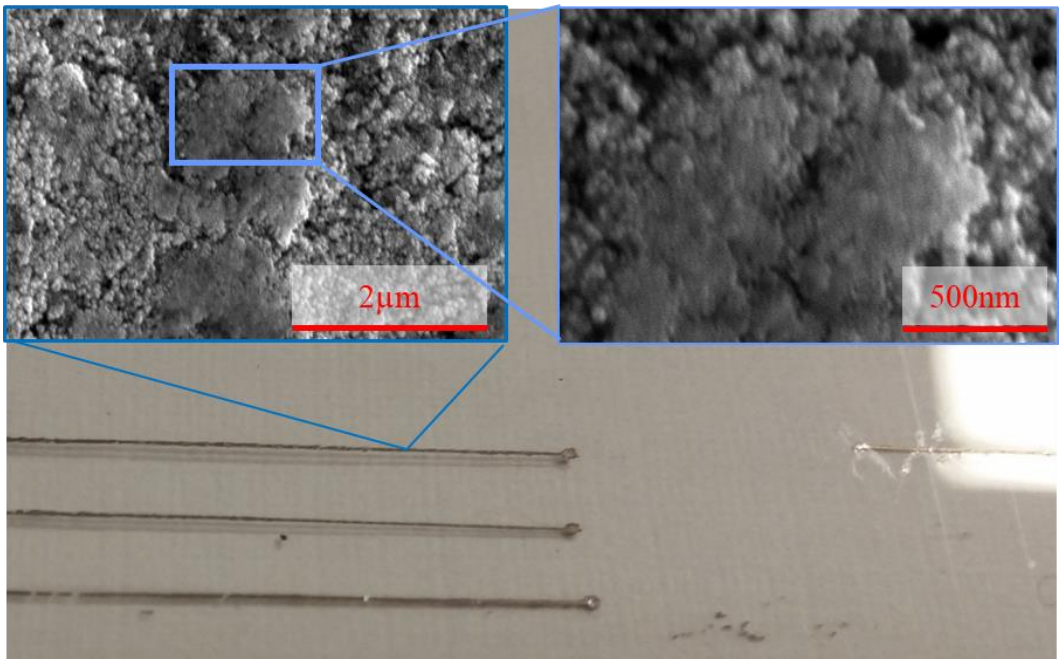

Figure 32 - Conductive lines printed using the MAPS printing process; the SEM photo shows the top layer of the lines to have been fully melted by the microheater [108].

4.4.4 Comparison to other processes

To evaluate the performance of MAPS against existing printing methods, a comparison in terms of print speed and production time between screen, inkjet and MAPS printing is presented in Table 3: it accounts for different curing methods and projects a printing time that could be expected to print a pattern that fills a standard A4 paper, which is 210mm x 297mm, if the printing direction is along the longer dimension.

Table 3 - Comparison of similar printing methods to MAPS [108].

Printing Method	Typical Patterning Speed (mm/s)	Curing Method	Typical Curing Time	Total Printing Time on A4 paper (s)	% Bulk Conductivity
Flatbed Screen Printing	250 [117]	Oven	90s [116]	90.8	18%
Inkjet	30 [16]	Oven + PulseForge	5min [118]	307	20%
		Oven	10min [119]	607	5%
MAPS	7	N/A	N/A	30	15%

In comparing the speed of MAPS to other technologies, it should be considered that the microheater array can be scaled in the direction of travel to increase the printing speed, like inkjet. Furthermore, simulations from our previous research have shown that replacing the conducting medium of air with helium will improve the printing speed of MAPS by 12 times [67] and the speed can be further increased by increasing the operating temperature of the microheater. These results show that the MAPS printing process is capable of printing conductive lines which are on par with those produced by current methods, and at speeds that compete with leading technologies. The results acquired from SEM analysis which show full melting of the silver nanoparticles show great promise for the improvement of the MAPS process: this suggests that much higher values of conductivity approaching bulk silver can be achieved through optimization of printing parameters, ink selection, and the ink deposition process.

CHAPTER 5

MAPS Printer for Flexible Electronics

The proof of concept model described previously provided great credibility to our project by enabling printing of conductive lines. However, there are some key areas for improvement. The first area for improvement is the microheater reliability. The previous microheater array was fabricated by depositing platinum filaments onto a Schott AF 32 eco glass wafer, which proved suitable for operation up to about 600°C. However, the microheaters usually don't last long at these high temperatures and tend to fail after a few seconds (some microheaters lasted longer than others, allowing the printed lines in Chapter 4 to be generated). The typical mode of failure for our microheaters was delamination of the filament from the glass substrate, as shown in Figure 33. Factors that contribute to this are the bond strength and coefficient of thermal expansion mismatch ("CTE mismatch") between the filament and the glass.

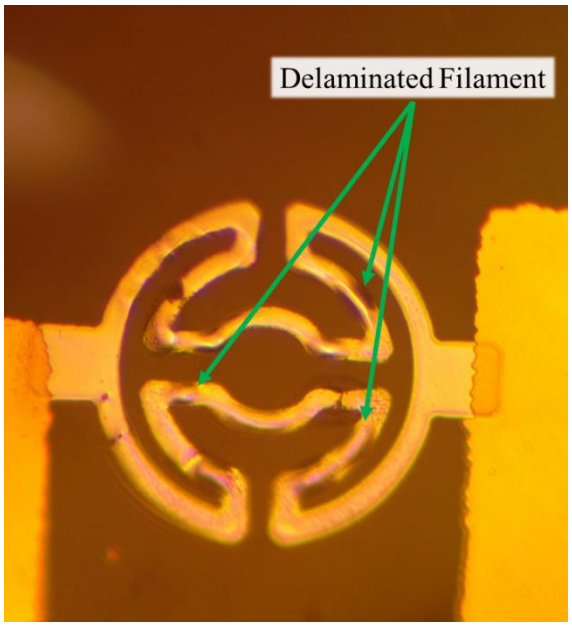

Figure 33 - The typical failure mode of a microheater: delamination of the thin film from the substrate.

In addition to reliability, the layout of the microheaters must be addressed. The previous microheater die had only 4 filaments arranged in a 2 x 2 square pattern. For printing, this design was only useful as a proof of concept to print a single conductive line at a time. The next step in developing this technology will be to show that we can print simple circuits using an array of microheaters.

The hardware also needs improvement. The method used to establish air gap was not reliable; Although the air gap could be maintained within ±3um as previously described in CHAPTER 4, initial setup of the air gap had an error of several microns. This is likely due to the contact plate flexing under the load of the printhead during setup. A reliable method of establishing air gap and microheater die parallel is required to expand this system to include a larger array of microheaters.

Lastly, a method of depositing ink should be incorporated into the printer. The method used to deposit ink in the previous design was to use screen printing in a separate process. This requires the use of another machine; however, it is more desirable if the process of depositing ink can be handled by the printer. This eliminates the need to have screen printing equipment on hand to use the MAPS printer.

This chapter outlines the design for a prototype printer which includes: design, fabrication and validation of a new microheater array and improvements to the printer hardware. Following design, the printer is fabricated. Some validation tests are performed to ensure that the printer will be capable of printing using MAPS technology.

5.1 Expanded Microheater Array

A new microheater die was developed to allow printing of simple circuits. The new microheater die was designed with the following requirements:

1. The array must be 16 microheaters wide
2. The microheaters should be arranged such that there is no gap between them in the direction of travel
3. Each lead must offer the same electrical resistance
4. The microheaters should share a ground lead
5. The microheaters must be capable of reaching a temperature of 600°C
6. The microheaters must survive the target temperature for at least 1 hour
7. Electrical connection must be possible without wire bonding

5.1.1 Design

A new arrangement was designed which used the same microheater geometry as described in CHAPTER 3. To meet requirement 1, 16 microheaters were arranged in an array 1.6mm wide, with each microheater being 100µm diameter. To meet requirement 2, the microheaters are staggered by spacing them by 100µm transverse to the travel direction and by 200µm longitudinal to the travel direction as shown in Figure 34. This arrangement ensures that there is no gap between the microheaters in the array direction, which will enable lines to be printed transverse to the direction of travel. To meet requirement 3, the width of the power lead is increased based on the distance from the microheater to the electrical contact point. To meet requirement 3, all the microheaters are connected on one side to ground.

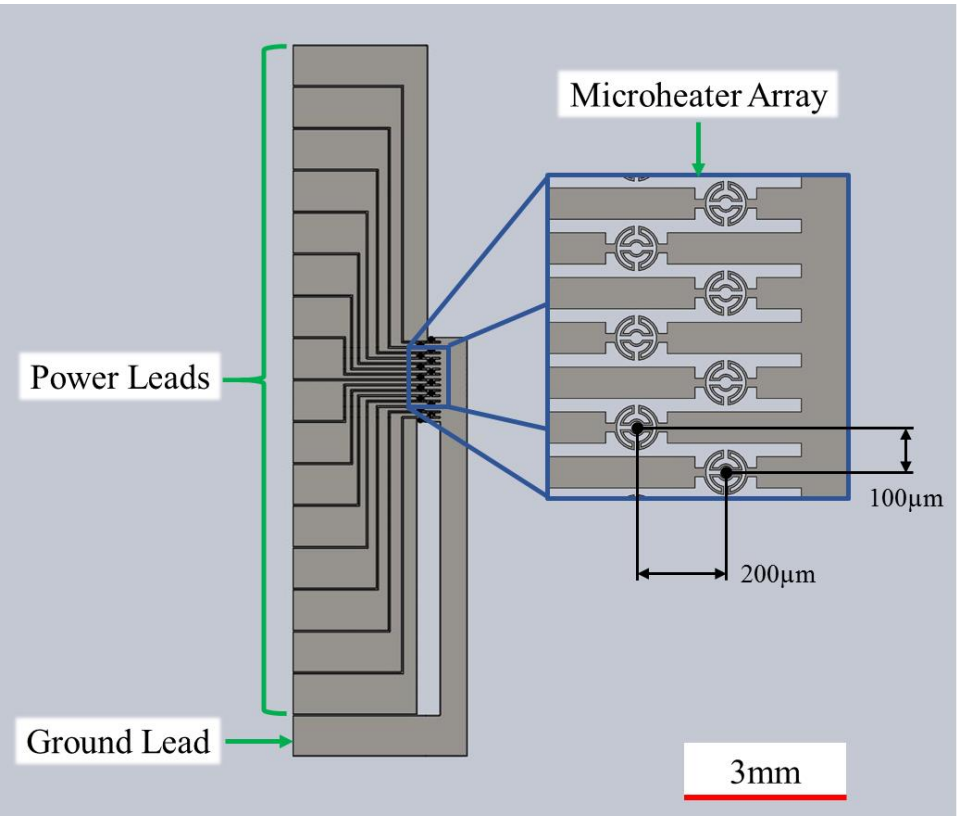

Figure 34 - Design of the new microheater array.

To meet requirements 5 and 6, new materials are needed to fabricate the microheaters. The primary failure mechanism in our microheaters was debonding of the filament from the substrate, which is due to the bond strength and CTE mismatch between the filament and the glass. For the new microheater array, sapphire was used as a substrate instead of the AF 32 eco glass due to the higher rate of thermal expansion and higher working temperature, as shown in Table 4. Sapphire is an anisotropic rhombohedral crystal form of aluminum oxide, and the rate of thermal expansion is different if measured normal to or parallel to the C-plane.

Table 4 - Comparison of the coefficients of thermal expansion (CTE) and maximum temperatures of Schott AF 32 eco glass [102], sapphire [103], and the metals composing the microheaters [120, 121].

Substrate	**CTE (10^{-6}/°C^{-1})**		**Maximum Working Temperature (°C)**
Schott AF 32 eco	3.2		717
Sapphire	Normal to C-plane	4.3	2000
	Parallel to C-plane	5.4	
Tantalum	6.5		2980
Platinum	9.0		1770

Finally, to meet requirement 7 extended leads were used in the design of the microheater die as shown in Figure 35. This was the same approach which was successfully used before as reported in CHAPTER 3.

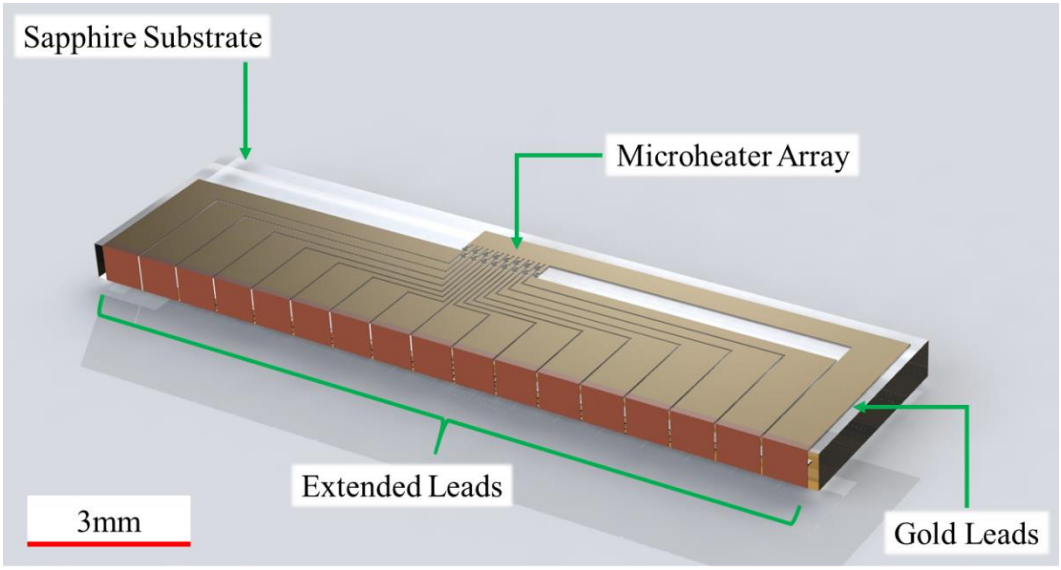

Figure 35 - Model of the new microheater die.

5.1.2 Fabrication

The fabrication steps of the microheater array are identical to the previous array except that the substrate is sapphire instead of AF 32 eco glass; the fabrication steps of the previous array can be seen in Figure 11. After deposition of the microheater arrays, the sapphire wafer was diced, yielding microheater dies that measure 13.6mm x 3.6mm. The finished microheater die can be seen in Figure 36.

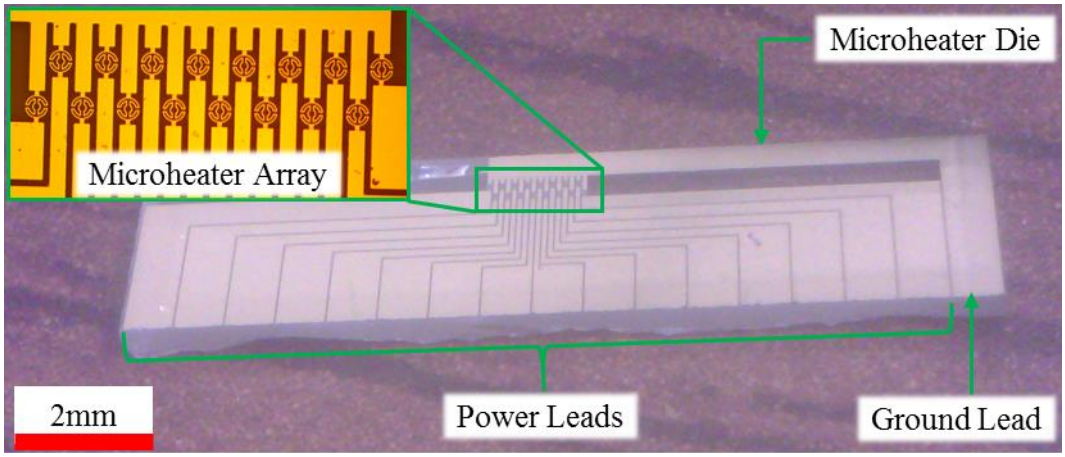

Figure 36 - The new microheater array on a sapphire substrate.

Extended leads can then be deposited onto the new microheater dies by following the steps shown in Figure 12. New packages were developed for the microheater dies which are like the ones used before. The finished microheater package can be seen in Figure *37*.

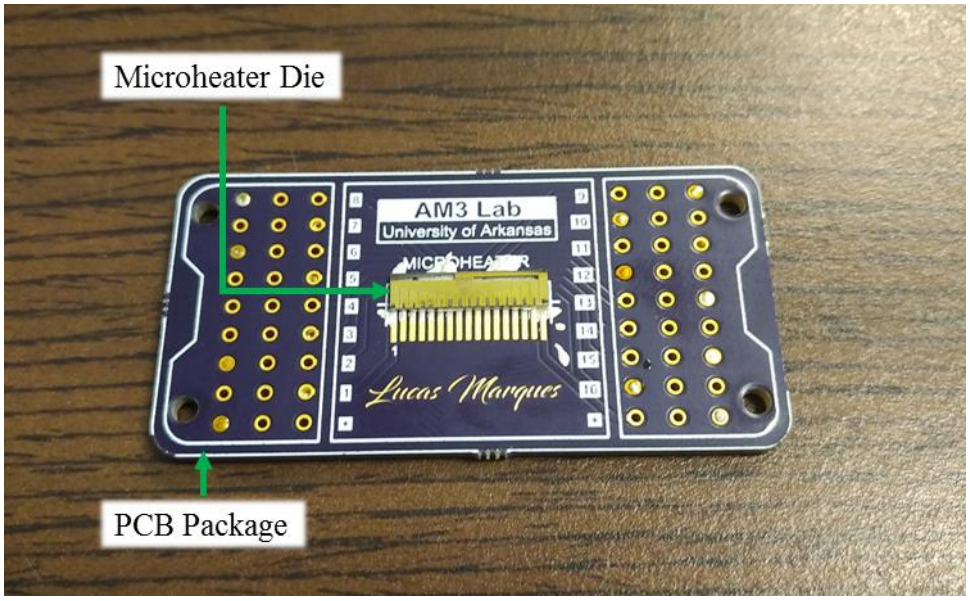

Figure 37 - Assembled microheater package

5.1.3 Validation

The same validation tests as used in Section 3.4 were used again to verify the performance of the new microheaters. Figure 38 shows the results of the same test used previously: the microheaters were put into an oven to determine their resistance – temperature coefficients. It should be noted that this test also measures the increase in the resistance of the leads and wire bonds which act as electrical connection, and after about 300°C, these components become damaged which increases the resistance significantly. Because of this, temperature data only up to 300°C is used. The results may be imprecise but give a good general idea of the response of the microheater to increased temperature.

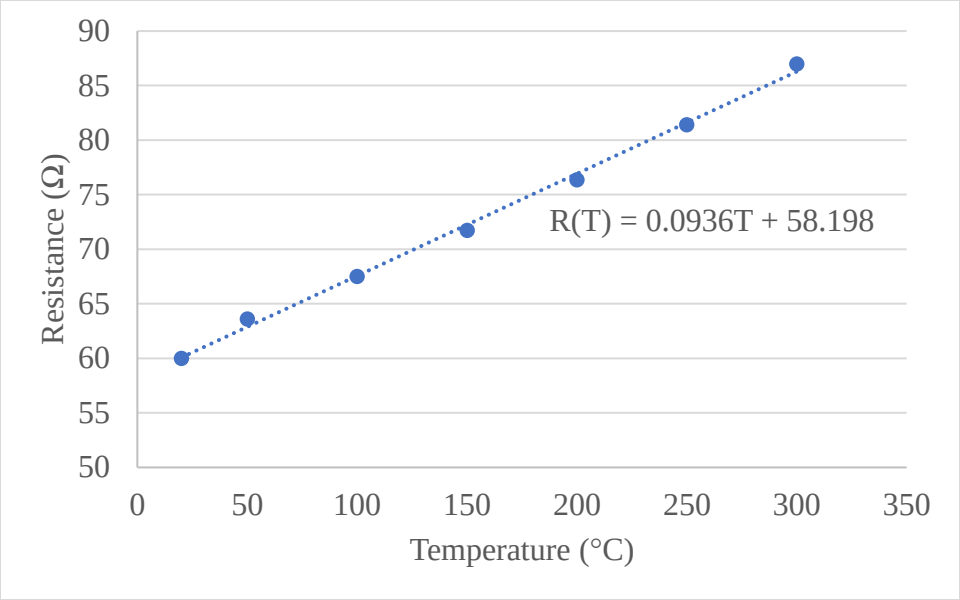

Figure 38 – The resistance of the microheater mounted on sapphire as a function of temperature.

With this data, we can now read the temperature of the microheater during operation by measuring its resistance in a voltage divider such as a Wheatstone bridge as discussed in Section 3.3.

Because the new microheaters are fabricated on a sapphire substrate, they require a much higher voltage to invoke a significant thermal response. This is due to the higher thermal conductivity of sapphire when compared to the glass that was previously used: sapphire has a thermal conductivity of 46 W/(m*K) [103] whereas Schott's AF 32 eco glass (previously used) has a thermal conductivity of 1.16 W/(m*K) [122]. Because sapphire is so effective of a conductor, much of the energy used to power the microheater is lost in heating the sapphire, so a higher voltage is needed to reach the same temperature. Because the previous PID control loop could only supply a maximum voltage of 12V, it could not be used to validate these microheaters. Instead, the microheater was wired into a simple voltage divider that could be used to measure its temperature as shown in Figure 39.

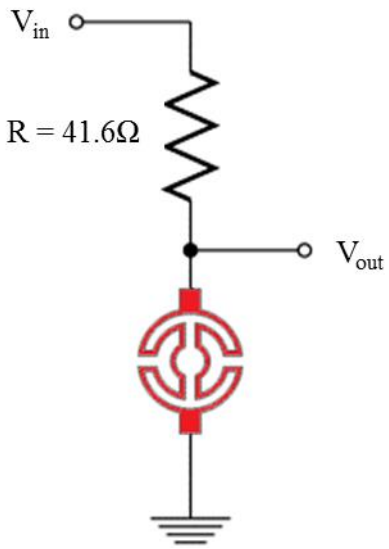

Figure 39 - Voltage divider used to measure the temperature of the microheater.

To use this circuit, a power supply can offer a constant input voltage V_{in}. Since the resistance R is known to be 41.6Ω, we can calculate the resistance of the microheater by reading the voltage V_{out}. This setup allows us to determine the temperature of the microheater by reading the resistance and comparing with the results in Figure 38, but an optimized thermal response time of the microheater using a PID feedback loop cannot be validated. This circuit was used to plot the temperature versus the power input of the microheater until failure; the result of this test can be seen in Figure 40.

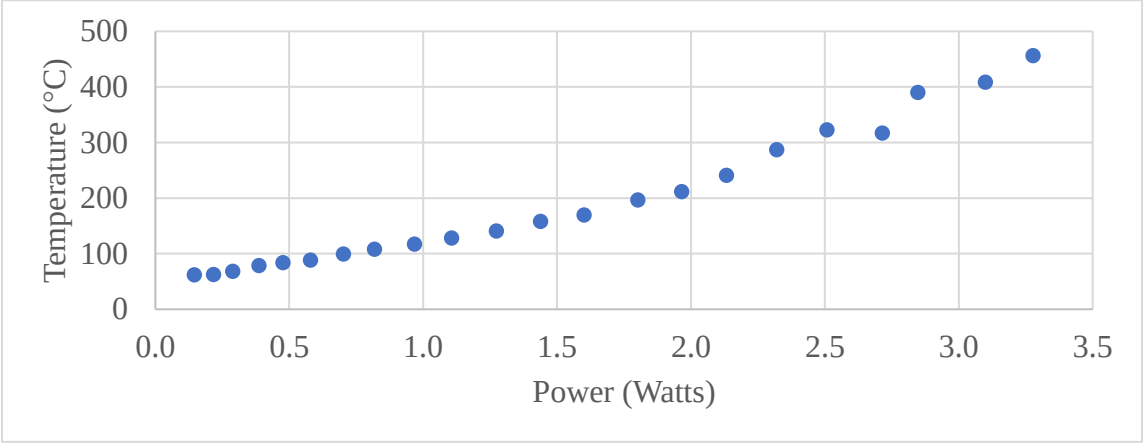

Figure 40 - Plot of the new microheaters' achieved temperature versus power input.

These tests provided two significant results: first, the new microheaters require much more power than the last design to achieve the same temperature (~3.2W versus 0.4W previously), and secondly the new microheaters fail at only ~450°C. The increased power requirement is likely due to the high thermal conductivity of sapphire, as discussed before. Regarding the second revelation: the temperature vs resistance curve that was acquired may be inaccurate, so it is difficult to tell whether the microheaters reach the temperature that we desire. Regardless, we will attempt to use the sapphire based microheaters to print conductive lines in Section 5.4.5 (although we will be unsure of the actual temperature of operation).

5.2 Design of Prototype Printer

In addition to an upgraded microheater array, new hardware is required to scale the proof of concept setup to a prototype printer. The previous setup was a low-cost machine that could only print single lines, but to further develop MAPS technology, the following design requirements were established for a prototype printer:

1. The design of the printhead must accept microheater arrays up to 50mm.
2. The length of the printing area must be at least 50mm long, which will allow a printing area of 50mm x 50mm when accounting for requirement 1.
3. A method of establishing air gap must be automated, and the vertical position of the microheater should be repeatable to ±1µm.
4. A method of validating the level the printhead must be automated.
5. The air gap must not deviate more than 3µm from the set point during operation.
6. A method of spreading ink must be incorporated into the design.

5.2.1 Assembly Overview

The design of the prototype is very similar to the experimental setup discussed in CHAPTER 4 with some notable upgrades. The base consists of a linear motion stage onto which a substrate carrier is attached; the substrate carrier is composed of a vacuum plate which holds the substrate firmly in place during operation. On top of the substrate carrier rests the printhead assembly in the same way as before: on three level-adjusting screws. the new microheater array is mounted onto the printhead assembly and is height-adjustable by a miniature linear motion stage.

The printhead assembly is held in place by a printhead mount by a shoulder bolt. The printhead mount also functions to spread the ink pushing a wet film applicator over the surface of the substrate during operation. The entire assembly is mounted onto a flat aluminum plate along with the motion and microheater controllers. An overview of the assembly can be seen in Figure 41.

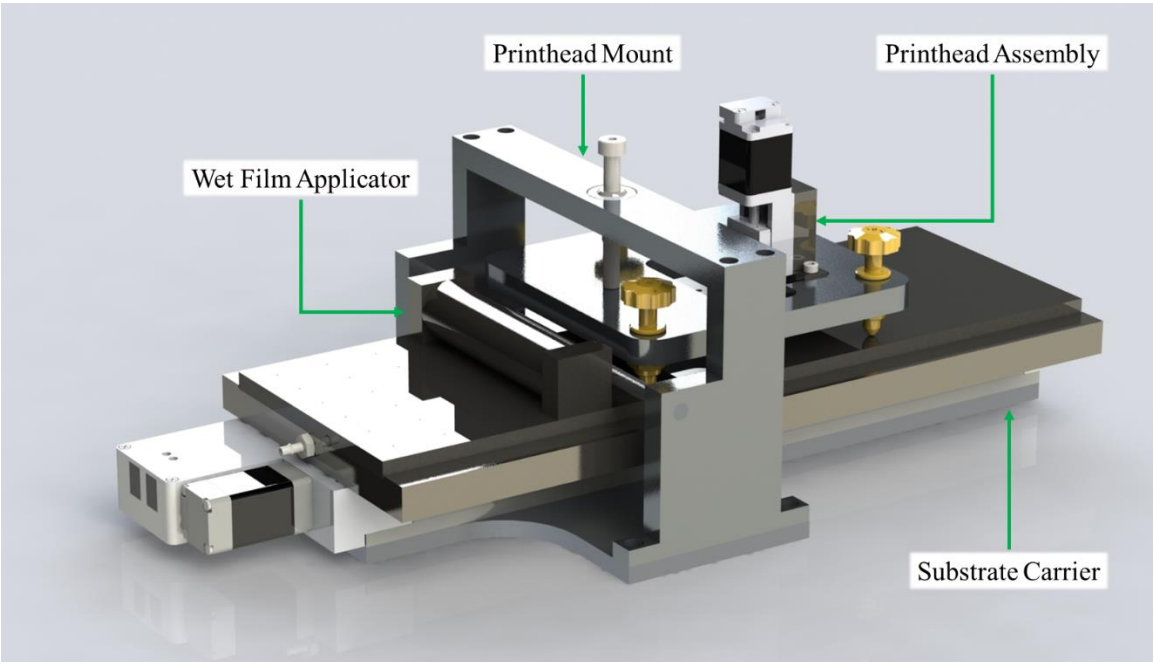

Figure 41 - A model of the prototype printer assembly.

5.2.2 Printing Stage

The printhead sits on top of a substrate carrier as in the previous design. The new substrate carrier is moved horizontally by a linear motion stage (Zaber P/N LRM200A-T3 [123]). The new substrate carrier's top is a steel vacuum plate, which ensures that the substrate stays in place during operation; vacuum is supplied by a 5V miniature vacuum pump (Hargraves P/N E134-11-050 [124]).

5.2.3 Printhead Assembly

The improved microheater package is mounted onto a miniature linear motion stage (Zaber P/N LSA10A-T4 [125]). This linear motion stage is mounted vertically onto a flat horizontal plate which is level-adjustable by three fine adjustment screws (Newport P/N AJS170-0.5K-NL [110]) as in the previous design. To meet requirement 1, the printhead was designed to accommodate a microheater package up to 60mm wide. A model of the printhead can be seen in Figure 42.

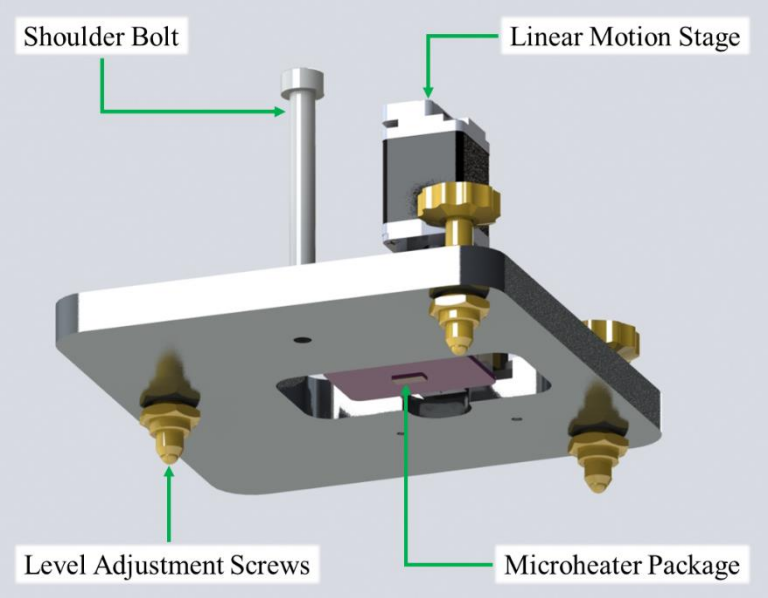

Figure 42 - Model of the printhead assembly.

5.2.4 Printhead Mount and Ink Applicator

The printhead is held in place by a shoulder bolt which attaches to a stationary arch (the printhead mount). The shoulder bolt attaches to the arch through a swivel joint bearing, with which the shoulder bolt shares a slip joint fit. This interface enables the printhead to move freely when adjusting its level but keeps it in place during operation of the printer. The arch also consists of a cross-member which is used to operate a wet film applicator (MTI Corp P/N EQ-Se-KTQ-4S [126]). This style of film applicator is used by dropping some ink on a flat substrate, then pushing the applicator over slowly to achieve a uniform film thickness. The combination of the length of the vacuum plate (300mm) and the position of the film applicator allows a printed area of 50mm, meeting requirement 2 as shown in Figure 43 (a) and (b): once the ink is deposited with the stage retracted (a), the stage can be moved forward to spread the ink and 50mm of the ink will be exposed to the microheater array (b).

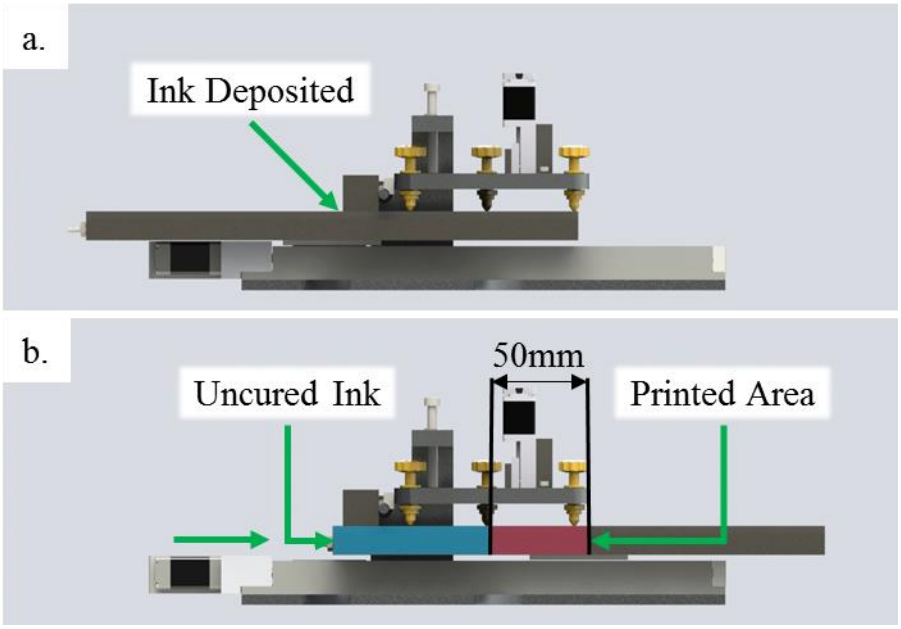

Figure 43 – Representation of the printing area possible using this printer.

5.3 Air Gap Analysis

The achievable air gap for this prototype printer can be analyzed in an identical way to the previous design as performed in CHAPTER 4 when accounting for new materials.

The new sapphire substrate used to make the microheater dies has a warp specification of < 21µm over the width of the wafer, which renders the error contribution from this component only < 0.4µm when solved using Equation 4. The surface roughness of the sapphire is less than the glass that it replaces as it is polished to < 0.35nm RMS.

The same assumptions regarding the substrate flatness made for the experimental proof of concept are used for this printer. The same plastic film can be used, which showed a TTV of < 1µm. The film will conform to the substrate carrier during operation of the printer: this will be ensured by the vacuum plate; therefore, the flatness of the vacuum plate should be considered. The vacuum plate which was used for this printer is made from A2 tool steel with the surface ground to a Geometric Dimensioning and Tolerancing (GD&T) flatness specification of 12µm.

This specification for flatness is the best that a typical machine shop can promise. This makes the steel vacuum plate the weakest link in this design, although it may work if the local flatness in the area that the printer operates is good: an experimental analysis of this is shown in Section 5.4.2 and the results of that analysis are included in Table 5. Although the contribution of the vacuum plate is greater than the desired tolerance, careful control of the printhead stage may mitigate its effects, as discussed in Section 5.4.2.

No significant change was made in the design of the printhead which would give rise to the question of increased deflection; in fact, the new printhead is made from more rigid materials (aluminum and steel) which should further mitigate the effect of deflection.

Table 5 - Tolerance analysis for the air gap achievable by this prototype printer.

Source	**Contribution to Air Gap Error**
Warp (Heater Die)	< 0.4µm
Roughness (Heater Die)	< 0.35nm RMS
Vacuum Plate TTV (in printing area)	6.1µm
Substrate TTV	1µm
Ink Layer Roughness	120nm RMS
Deflection	<< 0.1 µm
Total	± < 4µm

5.4 Printer Validation

The printer described in the previous sections was constructed and is shown in Figure 44. Operation of a MAPS printer requires that the gap between the microheater and the substrate be maintained within only a few microns. It is also critical that the microheater die be parallel to the substrate. These requirements were tested using contact sensors to validate that this printer is capable of the following tasks which will translate to success when using the microheater die:

1. The printhead position can be repeatably zeroed to within 1µm
2. The position of the printhead relative to the substrate is ±3µm over the entire printing area
3. The printhead can be leveled such that multiple contacts can be made in the same moment

The following sections describe the implementation of these tests and experimental results which validate this printer design.

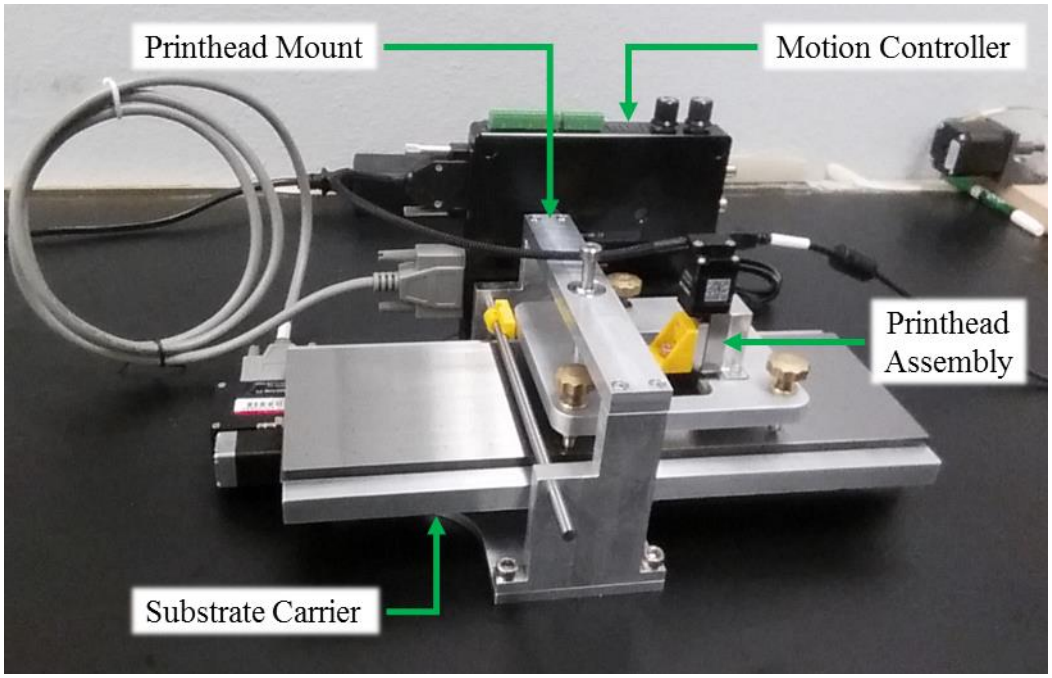

Figure 44 - The assembled prototype printer.

5.4.1 Contact Sensor Repeatability

To test that the air gap is repeatable to within 1µm, a machine screw with a pointed tip was mounted to the printhead and used as a contact sensor. During normal operation of the printer the microheater die will be used as the contact sensor, which has been successfully performed in the past as described in Section 4.3.1. The machine screw was connected to a digital input of the Zaber motion controller such that when contact was made between the screw and the vacuum

plate, a signal was sent to the controller. The followings pseudocode illustrates the steps used to establish contact and are illustrated in Figure 45:

Instruct the printhead to move down at a constant speed of ~240µm/s
While no contact is made (digital input):
    Request contact data
Instruct the printhead to stop
Record the current position of the printhead as the contact position
Instruct the printhead to move up to a "standoff" position of ~500µm

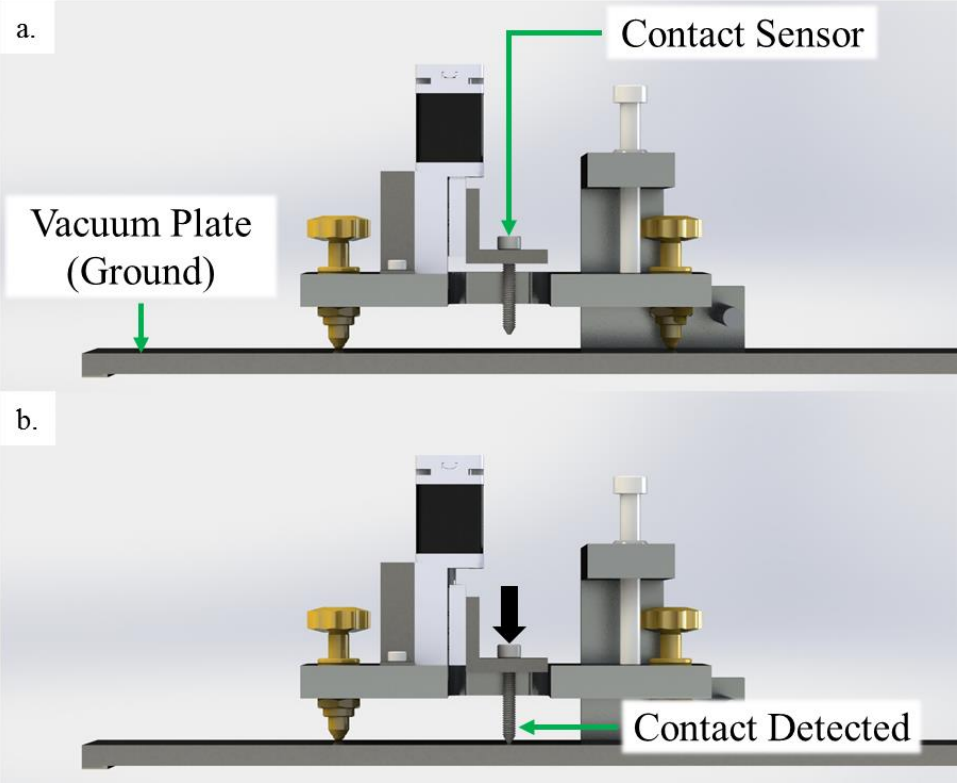

Figure 45 – Illustration of the method of testing repeatability of the contact detection procedure: when the contact sensor touches the vacuum plate it is grounded, which sends a signal to the controller.

This test was repeated 50 times to acquire a good sample size to analyze the proficiency of this contact method. It was found that this method yielded a repeatability within a 0.7µm window; the results of this test are shown in Figure 46.

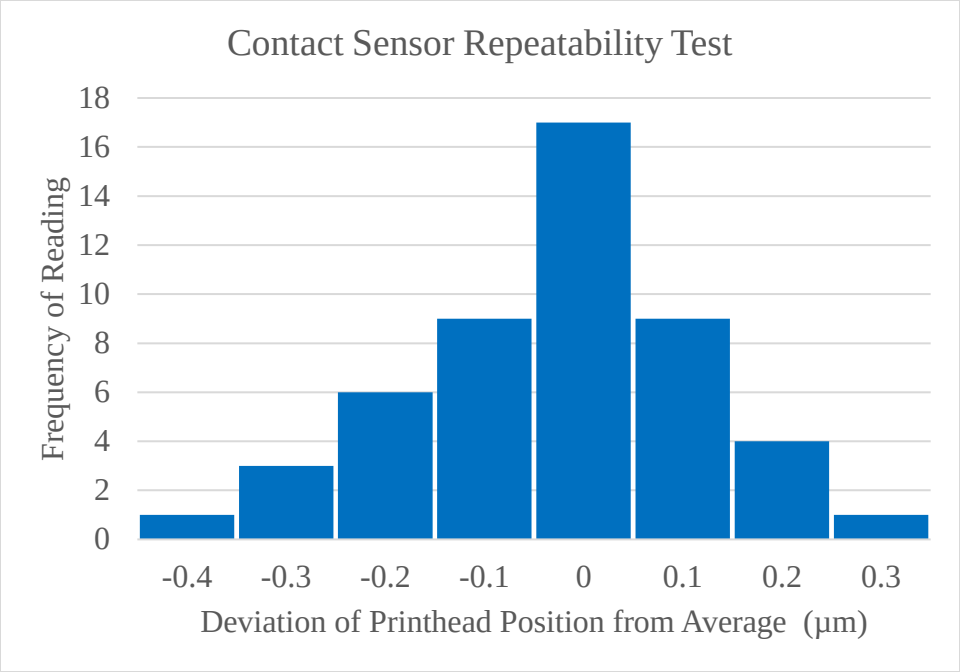

Figure 46 - Histogram of the results of the contact sensor repeatability test

5.4.2 Air Gap over Printing Area

To characterize the air gap tolerance over the entire vacuum plate, the same test from the previous section was used: 10 contacts each were made in multiple locations across the entire travel of the substrate carrier at 5mm intervals. The contacts are plotted across the vacuum plate in a similar fashion to a Coordinate Measuring Machine (CMM).

The results of this test show that the vacuum plate is significantly warped. Better results should be achievable if a polished glass were used instead of metal which is subject to warping. However, it is difficult to drill small vacuum holes in thick glass. For this printer, the area of concern is only between 100mm and 150mm of travel because that is where printing occurs as shown in Figure 43. In that area, the air gap error is within a 6.1µm window as shown in Figure 47. The error associated with maintaining the desired air gap can be further reduced to a 3.2µm window by restricting the printing area to between 100mm to 140mm.

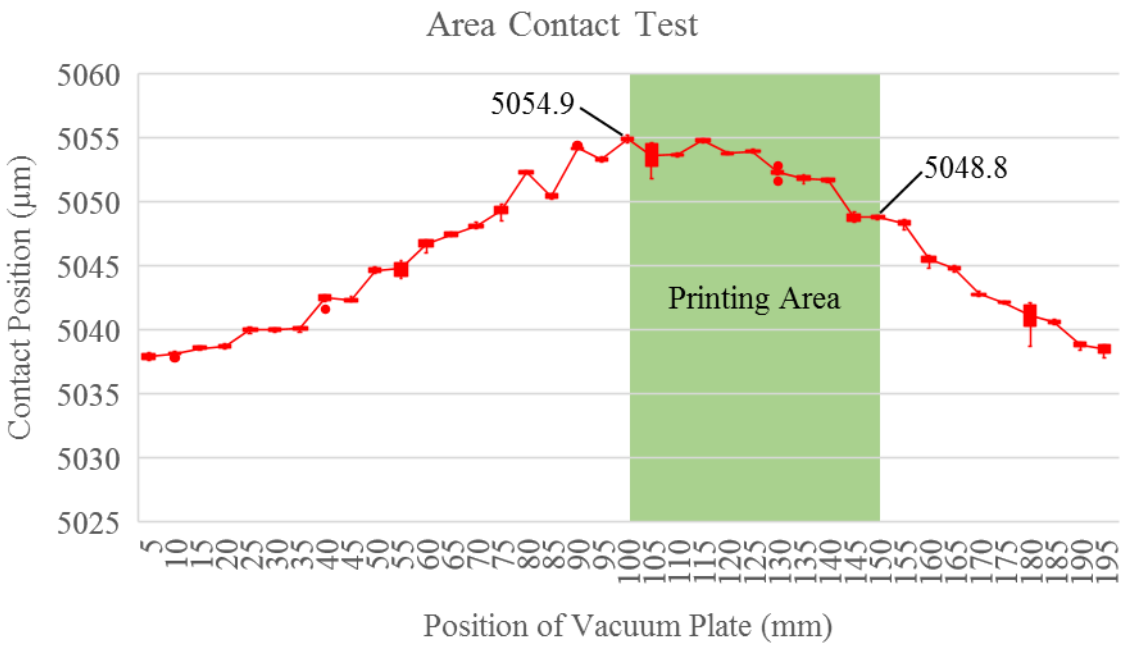

Figure 47 - Whisker plot of the contact test over the entire travel of the substrate carrier. The highlighted section represents the area that may be patterned during printing.

The data from this plot may also be used to dynamically control the height of the printhead during operation to maintain tighter control of the air gap. For example, when the position of the vacuum plate is 100mm, the printhead can be maintained at a position of 5059.9µm to achieve a 5µm air gap. As the vacuum plate moves, the printhead could eventually lower to 5053.8µm to maintain the air gap of 5µm at the vacuum plate position of 150mm. If this is done successfully, very precise control of the air gap can be realized.

5.4.3 Printhead Level Test

To test the leveling function of the printhead, a similar test to the one in Section 5.4.1 was used. The purpose of this test is to prove that the plane of the microheater die can be made parallel to a flat reference plane. In lieu of a microheater die, a fixture with three machine screws was made and attached to the printhead: in this test it is to be shown that the printhead can be adjusted so

that the points of the three screws can contact the vacuum plate in the same instant. During normal printer operation, the corners of the microheater die would be used instead of the screws. Contact was detected in the same way as before, with each machine screw being connected to a digital input of the controller. This setup can be seen in Figure 48.

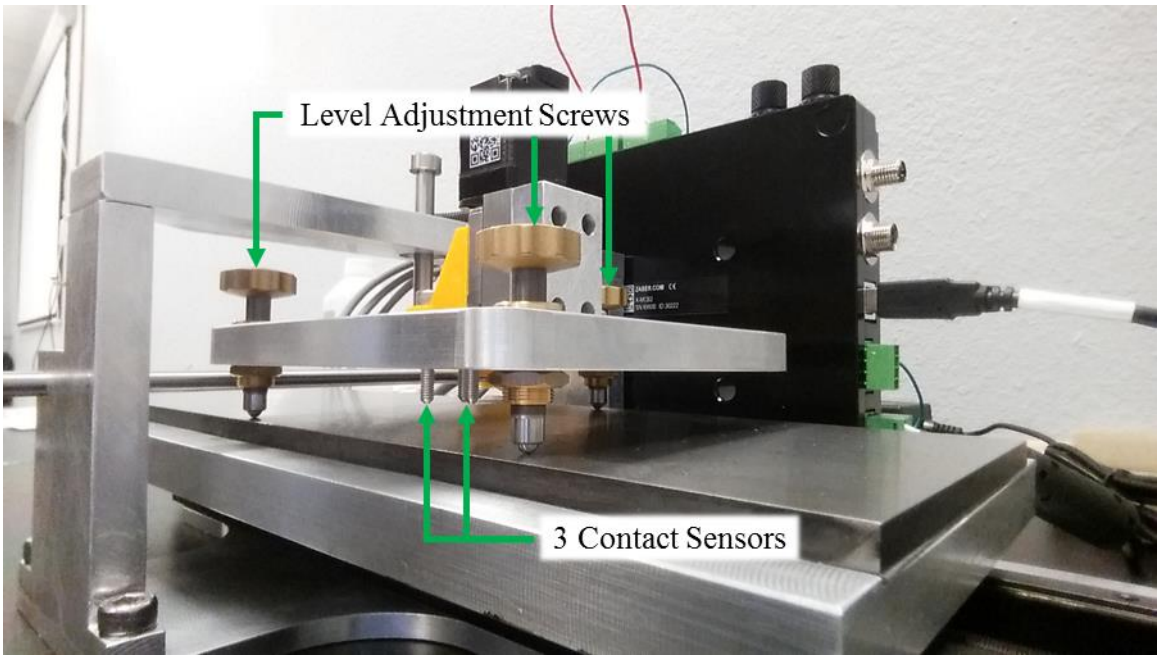

Figure 48 - Experimental setup for validating the leveling function of the printhead.

The logic used by the motion controller for this test was identical to that described in Section 5.4.1, except that the controller stops the printhead motion when any one of the three digital inputs is switched (each corresponding to a separate screw) and the controller reports which screw makes contact. With this information, the user can determine which leveling screw to turn to correct the level of the printhead; the process is repeated until all three screws contact the vacuum plate at once during the test. By using this procedure, the objective was reached with little difficulty.

5.4.4 Ink Spreading Test

To validate that the printer could also spread a layer of ink of a few microns, clear resin from Formlabs was used [127]. This resin has a viscosity of 850 – 900 centipoise, which is similar to silver nanoparticle flexographic inks such as NovaCentrix's PFI-600 ink [128] which can be used for this application. This test was performed with resin first to validate the function of the wet film applicator before silver nanoparticle ink was purchased: it can be reasonably assumed that the results obtained using the resin will also apply to similar silver nanoparticle inks used for flexible electronics.

To perform this test, a film of PET plastic was cut to fit the substrate carrier (100mm x 300mm). This plastic was placed onto the vacuum plate of the substrate carrier and the vacuum pump was activated. The film applicator was placed on its side marked "5µm" in front of the cross-bar of the printer's frame and the resin was applied before the film applicator with the stage in the home position as shown in Figure 49.

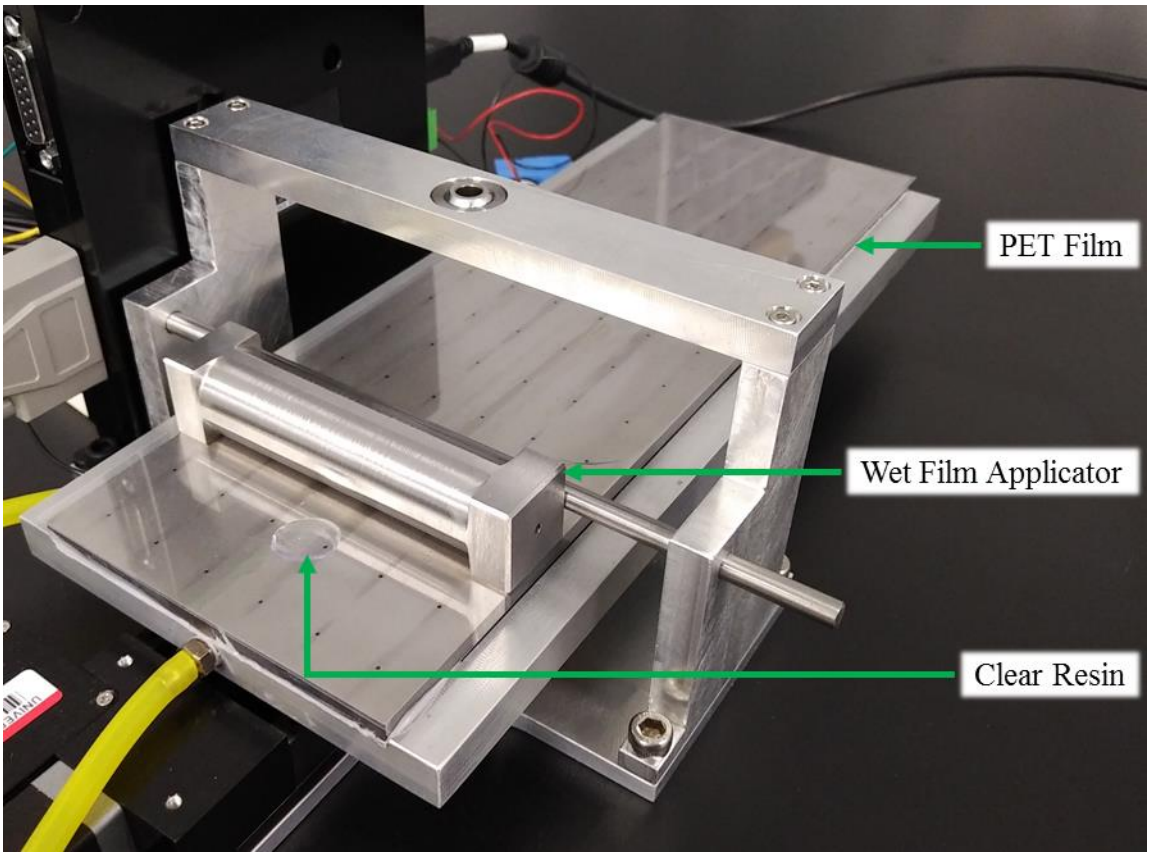

Figure 49 - The experimental setup to test the function of the wet film applicator.

By moving the stage at a constant speed of 6mm/s, the resin was spread in a thin layer on top of the PET plastic film. The plastic was moved underneath a UV lamp to cure the resin. After the resin was cured, a profilometer was used to measure the thickness at the edges of the film. The results showed a 6µm thick film was realized with a ~9µm thick rim along the edge. In practice, the microheater die could contact the ink if it were to move over the rim. We can ensure that this contact doesn't happen by noting the location of the rim and ensuring that the microheater die is raised sufficiently when approaching these areas.

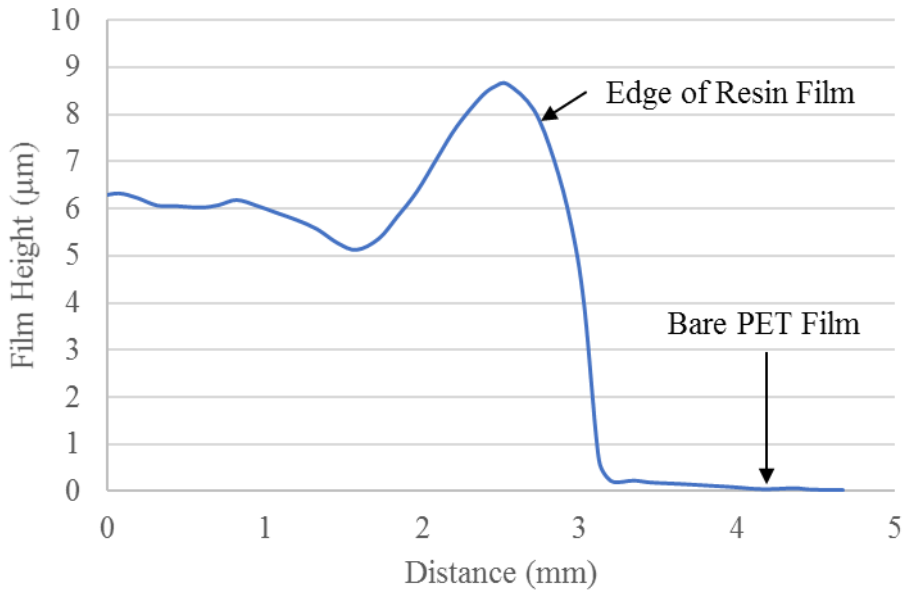

Figure 50 - Result of the profilometer test showing a resin film height of ~6µm

5.4.5 Validation with a microheater die

To validate that the printer could print conductive lines (and furthermore, circuits) as intended, a test was devised similar to that described in Section 4.4. The purpose of this test was to use a microheater to print a conductive line using a single microheater.

Just as with the proof of concept, a PET film was prepared with a screen-printed layer of PSI-211 [116] silver nanoparticle ink. Ideally, a flexography ink such as NovaCentrix's PFI-600 [128] would be used for printing so that the wet film applicator could be incorporated instead of using screen printing. However, only screen printing ink was available in the lab at the time; this ink is not compatible with the wet film applicator because it is too viscous (3500 – 6000 cP [116]). The following steps were taken to operate the printer:

1. The printhead is placed on top of the bare vacuum plate and the microheater is used as a contact sensor as described in section 5.4.1 to establish the “zero” position of the printhead axis.
2. The microheater package is raised several mm over the vacuum plate.
3. The printhead is raised and the PET film with the screen-printed ink is placed onto the vacuum plate.
4. The vacuum pump is activated to pull the PET film into contact with the vacuum plate.
5. The microheater is lowered to the desired air gap (10µm in this test).
6. The microheater is powered by a constant 13V.
7. The substrate carrier axis moves with a constant speed of 3mm/s.
8. After printing, the printhead is raised out of the way and the film is removed.

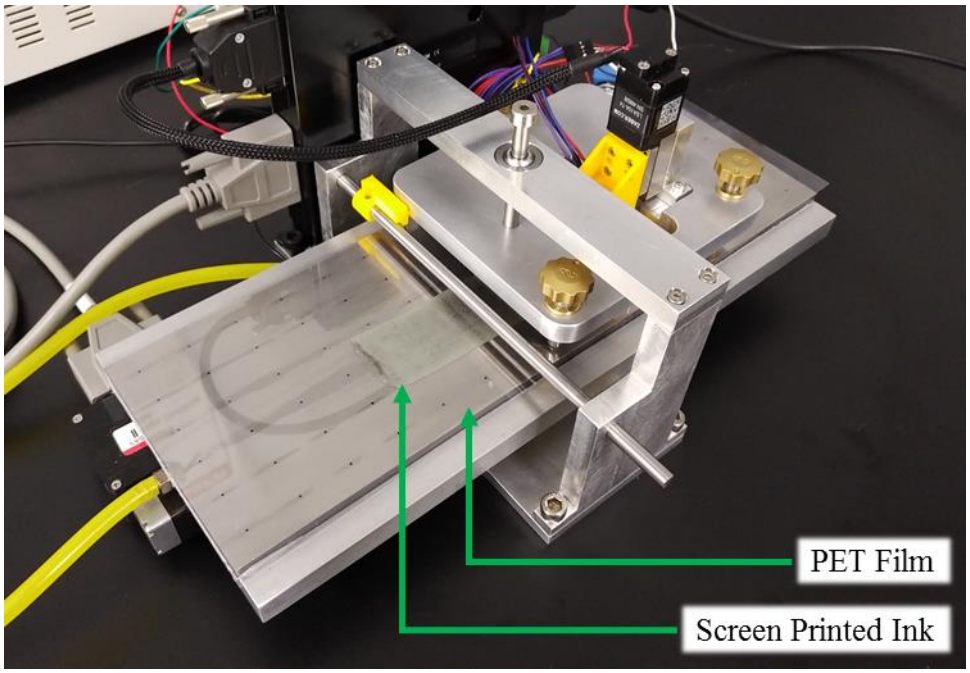

Figure 51 - Experimental setup to print a conductive line

The procedures previously described were used and a conductive trace was made on the PET film; it is shown in Figure 52 along with its profile as measured using a profilometer.

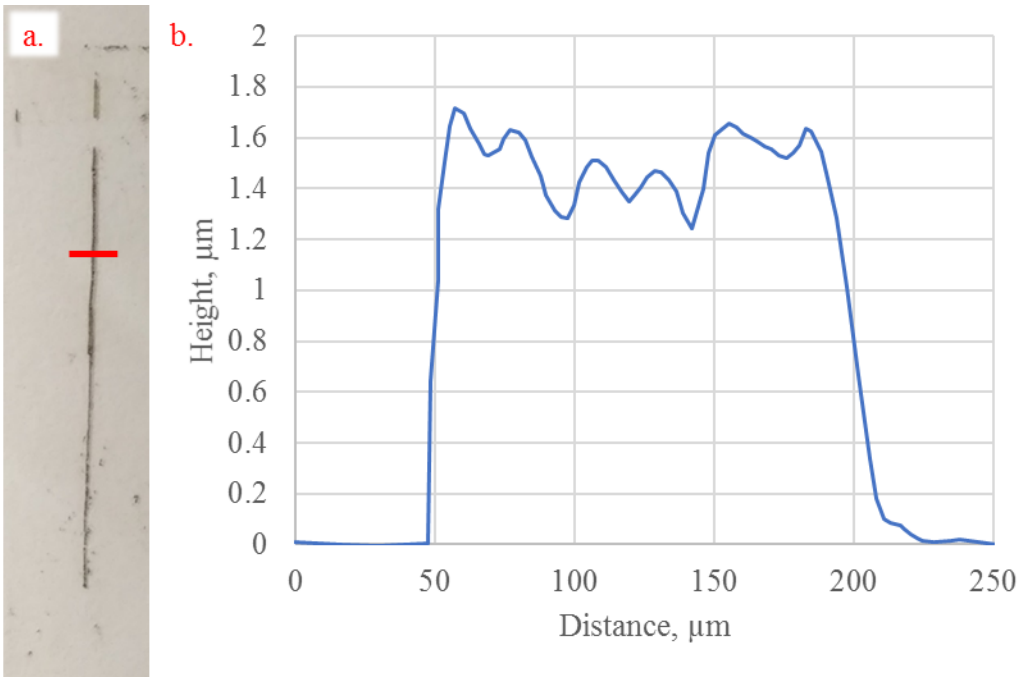

Figure 52 - a. Section of a printed line: the red line indicates the profilometer path and b. Profile of the conductive line printed using the prototype printer.

As before, the cross-sectional area of the line and the resistance along the line was used to find the resistivity, which was found to be 64µΩ*cm; this comes out to 2% of the conductivity of bulk silver which is far less than the 15% bulk conductivity that was achieved before. This is likely due to the multiple voids in the printed line which can be seen along the length of the line as shown in Figure 53.

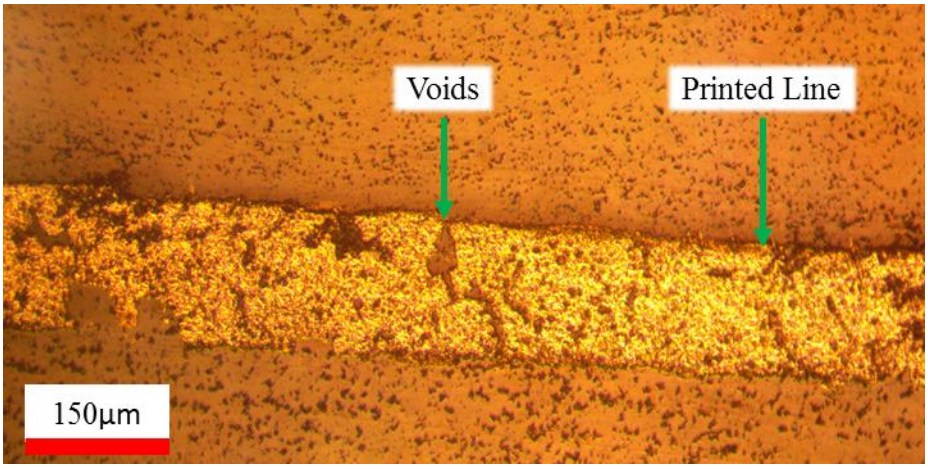

Figure 53 - Microscope view of the printed line

Some factors that may contribute to this problem are the speed of printing or the temperature of the microheater, both of which affect the curing timescale of the ink. In addition, an ink which is formulated for this curing method should improve performance, since this ink is designed to be dried and cured using ovens or infrared lamps [116]. Furthermore, if the average void size stays the same as the line width increases, the problem should become less pronounced when printing wider features. Optimizing the curing timescale to avoid this issue should be pursued in future research.

CHAPTER 6

Conclusions and Recommendations for Future Work

6.1 Summary of Thesis

In this thesis, a novel additive manufacturing method was introduced: Microheater Array Powder Sintering. This system uses microheaters to pattern a substrate over an air gap, which can be used for powder bed processes or for printing flexible electronics. CHAPTER 1 discussed various technologies used to print flexible electronics and their weaknesses, and the capability of MAPS to resolve the problems experienced in the industry today. CHAPTER 2 discussed other printing methods used in powder bed fusion processes as well as various parameters of concern to creating a MAPS printer.

In CHAPTER 3, a microheater design which was previously proposed [67, 96] was used in simulations to study the effects of the air gap and dwell time on the printing resolution and to explore ways to increase the air gap to ~100µm. Then, fabrication and control of the microheater was discussed. The microheater consisted of a platinum filament and gold leads and was fabricated on a glass substrate. The microheater was scaled to a 2 x 2 array and controlled using a PID control loop to maintain a temperature of 600°C.

In CHAPTER 4, an experimental setup which uses MAPS technology to generate conductive lines on a flexible substrate was developed. Design parameters and methods of overcoming different challenges associated with MAPS were discussed. Finally, a printer was built, and conductive lines were patterned onto a flexible plastic substrate. Conductive lines were printed onto a HS-PET flexible substrate which exhibited a resistivity of 10.9µΩ*cm, which is on par with other printing methods that are currently on the market.

Finally, CHAPTER 5 discussed the development of an improved prototype MAPS printer which features an expanded high temperature microheater array and automated controls. The new microheater array is fabricated on a sapphire substrate, which enables more reliable operation at high temperatures. The prototype printer is a more refined version of the proof of concept model which utilizes linear motion stages with sub-micron accuracy for positioning of the microheater array relative to the substrate. Validation tests were performed using machine screws as contact sensors to verify that a sub-micron air gap could be maintained by this printer for MAPS printing operation.

6.2 Market Analysis

The equipment market for flexible electronics is driven by the dramatic growth of electronic devices that use flexible circuits. The market for flexible electronics is projected to reach $87 billion by 2024 [129]. As consumer electronic devices become smaller and smaller, the demand for flexible electronics and subsequent printers will continue to grow: the market for printing equipment used to produce flexible circuits is estimated to be $1.4 billion by 2020 and to grow at a 33.4% compounded annual growth rate [129].

Various experts were interviewed by the author in regards to flexible circuit board production at the IDTechEx Printed Electronics USA 2017 trade show in Santa Clara, CA: generally, manufacturers use roll-to-roll methods such as flexography when a high number of components are required (> 10,000) but prefer screen printing for smaller order sizes (< 10,000 components) where each component might be sized at 100 ~ 1000 cm^2. Almost all manufacturers abstain from inkjet printing due to the slow drying speed of the ink unless it is required for making specialty products that require it such as flexible displays. From this research, it was determined that the

main parameters manufacturers use for choosing a production method are the speed and cost of printing, both of which relate to the practical order size that can be made as shown graphically in Figure 54. Because of this, MAPS may not compete with high-volume production methods such as gravure or flexography, but low-volume methods such as flatbed screen printing are fair game.

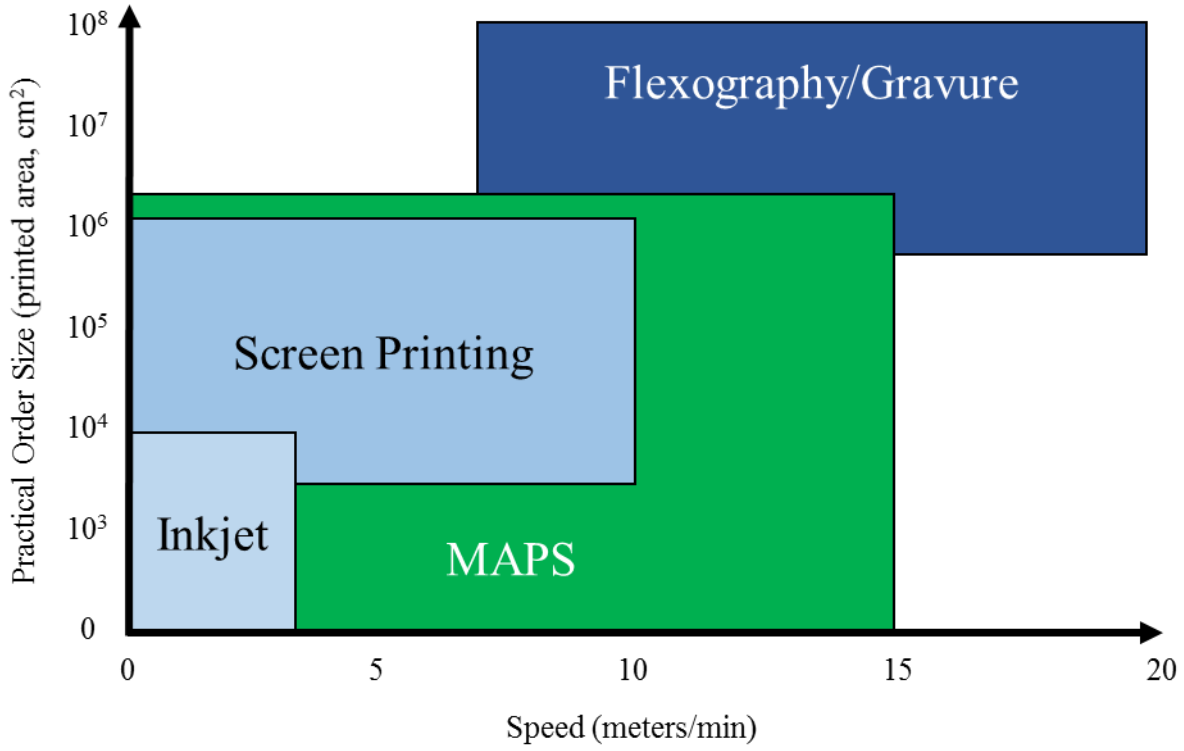

Figure 54 – A graphic showing the utility of MAPS compared to other systems.

MAPS will be attractive to the printing equipment market because the speed of a printing process is usually limited by the drying process, which we eliminate. For example, although Ceradrop's X-Serie inkjet printer can deposit ink at speeds up to 30 meters per minute [15], the ink can typically be dried at only 2 meters per minute [16]. MAPS combines the patterning and curing steps, increasing printing speeds. Furthermore, MAPS is based on a scalable design, in which the speed of printing can be increased by scaling the array in the direction of printing. For example, one microheater can be used to print at a speed of 7mm/s but two microheaters in a row along the

direction of printing doubles the speed to 14mm/s. The speed can further be increased by introducing helium into the process, which our simulations have shown will increase the speed 12 times [96]. Based on simulation data, a printing speed of 15 meters per minute can be achieved with a three-heater-long array and helium process gas whereas a typical rotary screen printing line might typically achieve 10 meters per minute [16].

In addition to offering increased printing speeds compared to inkjet and flatbed screen printing, MAPS offers a reduction in equipment and tooling costs. The design of the printhead allows for digital printing, which eliminates the need for special tooling to be made for each print. For example, screen printing requires a new screen to be made for each print, which costs hundreds of dollars per screen depending on resolution requirements and can take a few days or weeks to deliver. The equipment required to make screens in-house costs hundreds of thousands of dollars. MAPS can generate the desired pattern directly without any screens, stamps, or other order-specific tooling. By eliminating this requirement, MAPS gives manufacturers the ability to seamlessly accommodate smaller production runs (prototypes, small custom orders) in addition to medium to large orders (~1,000's to ~10,000's of flexible circuit boards). The elimination of tool fabrication, drying, and curing from the process is the major benefit offered by MAPS technology, because it allows manufacturers to reduce costs associated with equipment and tooling.

MAPS can reduce operating costs as well. One manufacturer told us that their screen printers cost them as much as $1,000 per hour to operate: included in this figure is tooling, power consumption, and floor space, among others. Screen printers require new screens for each order and new squeegees every 4 hours, but MAPS only requires new printheads once the microheaters burn out. Screen printed circuits require blanket exposure by infrared lamps and photonic curing

cells which consume kilowatts of power, but microheaters operate at milliwatts, and it is estimated that MAPS will use only 1% of the power when compared to these curing methods. The footprint of MAPS is much less than that of a screen printing line, since drying and curing stations are eliminated. These differences between the technologies allow MAPS to save manufacturers an estimated $2.3 million in operating costs per year if they switch from screen printing, which is illustrated in Table 6 along with estimated equipment costs for a single production line of each, based on industry interviews. The prospect of great savings will entice manufacturers to use our technology even if they have sunk costs into screen printing equipment.

Table 6 - Comparison of MAPS versus other prominent printing methods

	Screen Printing	**Inkjet**	**MAPS**
Printing Speed (m/min)	~10	~2	~15
Order Scalability	Good	Poor	Excellent
Tooling Cost per Order	$40 - $1500	$0	$0
Equipment Costs	~$400,000	~$650,000	~$200,000
Operating Costs per Week	~$170,000	~$165,000	~$100,000

Manufacturers also indicated that they need to use the same technology to create prototypes and production parts. Doing this reduces error between prototypes and final production, and customers can test the prototypes expecting the same results from production parts. MAPS addresses this issue by offering digital printing, thus eliminating the time and monetary costs of creating new tooling for the small prototype runs.

6.3 Future Work Recommendations

For MAPS to be competitive in the industrial market, some key issues must be addressed:

1. Increasing the air gap
2. Microheater reliability
3. Microheater control

The first problem refers to the small air gap of only a few microns between the printhead and the substrate. This is a very small gap that can be difficult to control during dynamic motion of the printing system. Our simulations have shown that the air gap can be increased to 20μm by using helium in place of air; a gap this size can more easily be maintained. Increasing the size of the air gap can also be achieved by raising the temperature of the microheaters. As described in this thesis, MAPS requires microheaters that can reach a temperature of 600°C; this generates considerable stresses on the materials used to build them, ultimately causing failure. Creating microheaters that can reliably withstand such high temperatures is challenging, but researchers have successfully created surface acoustic wave (SAW) devices using similar materials that can withstand temperatures up to 1,000°C [130, 104].

The second problem refers to the overall performance and expected life of the microheater array. A more in-depth study should be performed to evaluate the microheaters that are currently used for MAPS, and new microheaters should be developed which feature higher operating temperatures and longer operating life.

The third problem refers to the method used to control individual microheaters. Currently, one microheater is controlled at a time. A suitable circuit must be made to control multiple microheaters at once. Finally, software must be developed to coordinate substrate motion and microheater function so that a pattern can be printed. This is something that has been done before (ex. Inkjet). With some modification, this same principle can be used by a MAPS system to determine when to activate microheaters based on the substrate's position.

6.4 Closing Remarks

MAPS is an exciting new technology that has the potential to disrupt the market of flexible electronics. Despite the difficult challenges that this technology presents, it has shown great progress in the four short years since its inception. The microheaters used for the process have steadily improved in performance and reliability, low cost methods of maintaining a dynamic air gap have been realized, and conductive traces have been produced. In addition, MAPS has spurred interest among several leaders in the flexible electronics industry as a way of reducing cost and increasing speed of production in flexible electronics manufacturing. In several years when you purchase a new device with flexible electronics, perhaps it will be made with this novel system.

References

[1] V. Zardetto, T. M. Brown, A. Reale and A. Di Carlo, "Substrates for flexible electronics: A practical investigation on the electrical, film flexibility, optical, temperature, and solvent resistance properties," *J. Polym. Sci. B Polym. Phys.*, vol. 49, pp. 638-648, 2011.

[2] J. S. Kang, H. S. Kim and J. Ryu, "Inkjet printed electronics using copper nanoparticle ink," *Journal of Materials Science: Materials in Electronics,* vol. 21, no. 11, pp. 1213-1220, 2010.

[3] S. Magdassi, M. Grouchko and A. Kamyshny, "Conductive Ink-Jet Inks for Plastic Electronics: Air Stable Copper Nanoparticles and Room Temperature Sintering," in *International Conference on Digital Printing Technologies*, 2009.

[4] M. Zenou, O. Ermak, A. Saar and Z. Zotler, "Laser sintering of copper nanoparticles," *Journal of Physics D: Applied Physics*, vol. 47, no. 2, 2013.

[5] M. Schmidt, R. Kusche, B. von Issendorf and H. Haberland, "Irregular variations in the melting point of size-selected atomic clusters," *Nature,* vol. 393, pp. 238-240, 1998.

[6] P. Buffat and J.-P. Borel, "Size effect on the melting temperature of gold particles," *Physical Review A*, vol. 13, no. 6, pp. 2287-2298, 1976.

[7] S. H. Yoon, J. H. Lee, P. C. Lee and J. D. Nam, "Sintering and Consolidation of Silver Nanoparticles Printed on Polyimide Substrate Films," *Macromolecular Research,* vol. 17, no. 8, pp. 568-574, 2009.

[8] D. Feng, Y. Feng and S. Yuan, "Melting behavior of Ag nanoparticles and their clusters," *Applied Thermal Engineering*, vol. 111, pp. 1457-1463, 2017.

[9] C. Lee and J. W. Hahn, "Calculating the Threshold Energy of the Pulsed Laser Sintering of Silver and Copper Nanoparticles," *Journal of the Optical Society of Korea,* vol. 20, no. 5, pp. 601-606, 2016.

[10] M. S. Yusof and D. T. Gethin, "Investigation of Carbon Black Ink on Fine Solid Line Printing in Flexography," in *Proceeding of 10th WSEAS international conference on electronics, hardware, wireless and optical communications*, Cambridge, UK, 2011.

[11] M. Gagliardi, "Global Markets for Roll-to-Roll Technologies for Flexible Devices," BCC Research, Wellesley, MA, 2016.

[12] J. Chang, G. Tong and E. Sanchez-Sinencio, "Challenges of printed electronics on flexible substrates," in *IEEE 55th International Midwest Symposium on Circuits and Systems (MWSCAS)*, 2012.

[13] E. Jewell, S. Hamblyn, T. Claypole and D. Gethin, "Deposition of high conductivity low silver content materials by screen printing," *Coatings,* vol. 5, pp. 172-185, 2015.

[14] DLP Imaging Corp., "fineLine directLaser!®," http://www.digitalscreenprinting.com, [Online]. Available: https://tinyurl.com/ybmlqmyg. [Accessed 28 November 2017].

[15] Ceradrop, "X-Serie | Product Specifications," [Online]. Available: http://www.ceradrop.com/content/uploads/2016/04/CeraPrinter_X-Serie.pdf. [Accessed 27 November 2017].

[16] M. Hösel, R. Søndergaard, D. Angmo and F. Krebs, "Comparison of Fast Roll-to-Roll Flexographic, Inkjet, Flatbed, and Rotary Screen Printing of Metal Black Electrodes for Polymer Solar Cells," *Advanced Engineering Materials,* vol. 15, no. 10, pp. 995-1001, 2013.

[17] Y. Huang and N. Bu, "Inkjet printing for flexible electronics: Materials, processes and equipments," *Chinese Science Bulletin,* vol. 55, no. 30, pp. 3383-3407, 2010.

[18] K. C. Yung, X. Gu, C. P. Lee and H. S. Choy, "Ink-jet printing and camera flash sintering of silver tracks on different substrates," *Journal of Materials Processing Technology,* vol. 210, no. 15, pp. 2268-2272, 2010.

[19] M. J. Guillot, S. C. McCool and K. A. Schroder, "Simulating the thermal response of thin films during photonic curing," in *ASME 2012 International Mechanical Engineering Congress & Exposition*, Houston, 2012.

[20] N. D. Holt, L. G. Marques, A. Van Horn, M. Montazeri and W. Zhou, "Fabrication and control of a microheater array for Microheater Array Powder Sintering," *The International Journal of Advanced Manufacturing Technology,* 2017.

[21] J. J. Beaman and C. R. Deckard, "Selective Laser Sintering with Assisted Powder Handling". Patent US4938816A, 1990.

[22] M. Agarwala, D. Bourell, J. Beaman, H. Marcus and J. Barlow, "Direct Selective Laser Sintering of Metals," *Rapid Prototyping Journal,* vol. 1, no. 1, pp. 26-36, 1995.

[23] C. Shuai, P. Feng and C. Gao, "Simulation of dynamic temperature field during selective laser sintering of ceramic powder," *Mathematical and Computer Modelling of Dynamical Systems,* vol. 19, no. 1, pp. 1-11, 2013.

[24] Y. P. Kathuria, "Microstructuring by selective laser sintering of metallic powder," *Surface and Coatings Technology,* vol. 116, pp. 643-647, 1999.

[25] J. P. Kruth, M. C. Leu and T. Nakagawa, "Progress in additive manufacturing and rapid prototyping," *CIRP Annals - Manufacturing Technology,* vol. 47, no. 2, pp. 525-540, 1998.

[26] J. P. Kruth, B. Van der Schueren, J. Bonse and B. Morren, "Basic powder metallurgical aspects in selective metal powder sintering," *CIRP Annals - Manufacturing Technology,* vol. 45, no. 1, pp. 183-186, 1996.

[27] B. Van der Schueren and J. P. Kruth, "Powder deposition in selective metal powder sintering," *Rapid Prototyping Journal,* vol. 1, no. 3, pp. 23-31, 1995.

[28] S. Kumar, "Selective laser sintering: a qualitative and objective approach," *JOM,* vol. 55, no. 10, pp. 43-47, 2003.

[29] T. R. Mahale, "Electron beam melting of advanced materials and structures," 2009.

[30] I. Gibson, D. Rosen and B. Stucker, Additive Manufacturing Technologies, Second Edition, New York: Springer, 2015.

[31] M. Khang, J. Fuh and L. Lu, "Direct metal laser sintering for rapid tooling: processing and characterisation of EOS parts," *Journal of Materials Processing Technology,* vol. 113, no. 1, pp. 269-272, 2001.

[32] H. Ho, I. Gibson and W. Cheung, "Effects of energy density on morphology and properties of selective laser sintered polycarbonate," *Journal of Materials Processing Technology,* vol. 89, pp. 204-210, 1999.

[33] D. Miller, C. Deckard and J. Williams, "Variable beam size SLS workstation and enhanced SLS model," *Rapid Prototyping Journal,* vol. 3, no. 1, pp. 4-11, 1997.

[34] H. Niu and I. Chang, "Selective laser sintering of gas atomized M2 high speed steel powder," *Journal of materials science,* vol. 35, no. 1, pp. 31-38, 2000.

[35] Y. A. Song and W. Koenig, "Experimental study of the basic process mechanism for direct selective laser sintering of low-melting metallic powder," *CIRP Annals - Manufacturing Technology,* vol. 46, no. 1, pp. 127-130, 1997.

[36] R. Patwa, H. Herfurth, J. Chae and J. Mazumder, "Multi-beam laser additive manufacturing," in *32nd International Congress on Applications of Lasers and Electro-Optics,* 2013.

[37] D. S. Hermann and R. Larson, "Selective Mask Sintering for Rapid Production of Parts, Implemented by Digital Printing of Optical Toner Masks," in *NIP & Digital Fabrication Conference,* 2008.

[38] H. R. Thomas, N. Hopkinson and P. Erasenthiran, "High speed sintering - continuing research into a new rapid manufacturing process," in *Proceedings of 17th SFF Symposium*, Austin, TX, 2006.

[39] B. Khoshnevis, "Selective inhibition of bonding of powder particles for layered fabrication of 3-D objects". United States of America Patent US6589471, 8 July 2003.

[40] B. Khoshnevis, M. Yoozbashizadeh and Y. Chen, "Metallic part fabrication using selective inhibition sintering (SIS)," *Rapid Prototyping Journal*, vol. 18, no. 2, pp. 144-153, 2012.

[41] J. Moon, J. E. Grau, V. Knezevic, M. J. Cima and E. M. Sachs, "Ink-jet printing of binders for ceramic components," *Journal of the American Ceramic Society*, vol. 85, no. 4, pp. 755-762, 2002.

[42] A. S. Basu, S. McNamara and Y. B. Gianchandani, "Scanning thermal lithography: maskless, submicron thermochemical patterning of photoresist by ultracompliant probes," *Journal of Vacuum Science & Technology B*, vol. 22, no. 6, pp. 3217-3220, 2004.

[43] B. C. Chou, "Thermal printing device and methods for manufacturing the same". United States of America Patent US20050212859, 29 September 2005.

[44] A. Ø. Hartmann and F. W. Tjellesen, "Three-dimensional printer". United States of America Patent US9421715, 23 August 2016.

[45] C. K. Chua and K. F. Leong, Rapid prototyping: principles and aplications, World Scientific, 2003.

[46] P. Torabi, M. Petros and B. Khoshnevis, "Selective inhibition sintering: the process for consumer metal additive manufacturing," *3D Printing and Additive Manufacturing*, vol. 1, no. 3, pp. 152-155, 2014.

[47] D. R. Askeland and W. J. Wright, The Science and Engineering of Materials, Seventh Edition, Boston: Cengage Learning, 2014.

[48] J. K. Mackenzie and R. Shuttleworth, "A Phenomenological Theory of Sintering," in *Proceedings of the Physical Society. Section B*, 1949.

[49] Kruth, "Binding Mechanisms in Selective Laser Sintering and Selective Laser Melting," *Rapid Prototyping Journal*, vol. 11, no. 1, pp. 44-59, 2004.

[50] E. O. Olakanmi, "Selective laser sintering/melting (SLS/SLM) of pure Al, Al-Mg, and Al-Si powders: Effect of processing conditions and powder properties," *Journal of Materials Processing Technology*, vol. 213, no. 8, pp. 1387-1405, 2013.

[51] R. M. German, P. Suri and S. J. Park, "Review: liquid phase sintering," *Journal of Materials Science,* vol. 44, no. 1, pp. 1-39, 2009.

[52] *Metalon® JS-B40G*, NovaCentrix, 2015.

[53] X. Gu, "Ink-jet printed high conductive silver traces on polymer substrates sintered at room temperature by a camera flash lamp," in *16th International Conference on Electronic Packaging Technology*, 2015.

[54] K. A. Schroder, "Mechanisms of Photonic Curing: Processing High Temperature Films on Low Temperature Substrates," *Nanotech,* vol. 2, 2011.

[55] "Conductive Metallic Inks," Applied Nanotech, Inc., 2015. [Online]. Available: http://www.appliednanotech.net/tech/conductive_inks.php. [Accessed 20 February 2017].

[56] G. Vandevenne, W. Marchal and I. Verboven, "A study of the thermal sintering process of silver nanoparticle inkjet inks to achieve smooth and highly conducting silver layers," *Physica status solidi,* vol. 213, no. 6, pp. 1403-1409, 2016.

[57] O. Ermak, M. Zenou and G. Toker, "Rapid laser sintering of metal nano-particles inks," *Nanotechnology,* vol. 27, no. 38, 2016.

[58] K. L. Zhang, "Fabrication, modeling and testing of a thin film Au/Ti microheater," *International Journal of Thermal Sciences,* vol. 46, no. 6, pp. 580-588, 2007.

[59] S. Toskov, R. Glatz, G. Miskovic and G. Radosavljevic, "Modeling and fabrication of pt micro-heaters built on alumina substrate," in *36th International Spring Seminar On Electronics Technology*, 2013.

[60] R. M. Tiggelaar, "Silicon-technology based microreactors for high-temperature heterogeneous partial oxidation reactions," M.S. Thesis, University of Twente, Enschede, The Netherlands, 2004.

[61] S. Z. Ali, F. Udrea, W. I. Milne and J. W. Gardner, "Tungsten-based SOI microhotplates for smart gas sensors," *Journal of Microelectromechanical Systems,* vol. 17, pp. 1408-1417, 2008.

[62] L. Mele, F. Santagata and E. Iervolino, "A molybdenum MEMS microhotplate for high-temperature operation," *Sensors and Actuators A: Physical,* vol. 188, pp. 173-180, 2012.

[63] L. Setti, C. Piana and S. Bonazzi, "Thermal inkjet technology for the microdeposition of biological molecules as a viable route for the realization of biosensors," *Anal. Lett.,* vol. 37, pp. 1559-1570, 2004.

[64] X. Cui and T. Boland, "Human microvasculature fabrication using thermal inkjet printing technology," *Biomaterials,* vol. 30, pp. 6221-6227, 2009.

[65] T. Mendum, E. Stoler, H. VanBenschoten and J. C. Warner, "Concentration of bisphenol A in thermal paper," *Green Chemistry Letters and Reviews,* vol. 4, pp. 81-86, 2011.

[66] M. Baumers, C. Tuck and R. Hague, "SELECTIVE HEAT SINTERING VERSUS LASER SINTERING: COMPARISON OF DEPOSITION RATE, PROCESS ENERGY CONSUMPTION AND COST PERFORMANCE".

[67] A. VanHorn, "Selective Resistive Sintering: A Novel Additive Manufacturing Process," M.S. Thesis, University of Arkansas, Fayetteville, 2016.

[68] L. Xu, Y. Wang and H. Zhou, "Design, Fabrication, and Characterization of a High-Heating-Efficiency 3-D Microheater for Catalytic Gas Sensors," *Journal of Microelectromechanical Systems,* vol. 21, no. 6, pp. 1402-1409, 2012.

[69] W.-Y. Chang and Y.-S. Hsihe, "Multilayer microheater based on glass substrate using MEMS technology," *Microelectronic Engineering,* vol. 149, pp. 25-30, 2016.

[70] T. Guan and R. Puers, "Thermal Analysis of a Ag/Ti Based Microheater," *Procedia Engineering,* vol. 5, pp. 1356-1359, 2010.

[71] A. Pike and J. W. Gardner, "Thermal modelling and characterisation of micropower chemoresistive silicon sensors," *Sensors and Actuators B: Chemical,* vol. 45, pp. 19-26, 1997.

[72] D. Bradley and A. Entwistle, "Determination of the emissivity, for total radiation, of small diameter Platinum-10% Rhodium wires in the temperature range 600-1450 C," *British Journal of Applied Physics,* vol. 12, p. 708, 1961.

[73] S. Joy and J. K. Antony, "Design and simulation of a micro hotplate using COMSOL multiphysics for MEMS based gas sensor," in *Fifth International Conference on Advances in Computing and Communications (ICACC),* 2015.

[74] G. Velmathi, S. Ramshanker and S. Mohan, "Design, electro-thermal simulation and geometrical optimization of double spiral shaped microheater on a suspended membrane for gas sensing," in *36th Annual Conference on IEEE Industrial Electronics Society,* 2010.

[75] S. Lee, D. Dyer and J. Gardner, "Design and optimisation of a high-temperature silicon micro-hotplate for nanoporous palladium pellistors," *Microelectronics Journal,* vol. 34, pp. 115-126, 2003.

[76] Y. Mo, Y. Okawa, K. Inoue and K. Natukawa, "Low-voltage and low-power optimization of micro-heater and its on-chip drive circuitry for gas sensor array," *Sensors and Actuators A: Physical,* vol. 100, pp. 94-101, 2002.

[77] B. Bae, J. Yeom, B. R. Flachsbart and M. A. Shannon, "A Sensorless and Versatile Temperature-Control System for MEMS Microheaters," *Transactions of the Korean Institute of Electrical Engineers*, vol. 55, no. 11, pp. 544-547, 2006.

[78] M. N. H. Z. Alam, A. A. A. Moghadam and A. Kouzani, "Establishment of temperature control scheme for microbioreactor operation using integrated microheater," *Microsystem Technologies*, vol. 21, no. 2, pp. 415-428, 2015.

[79] J. F. Creemer, D. Briand and H. W. Zandbergen, "Microhotplates with TiN heaters," *Sensors and Actuators A: Physical*, vol. 148, no. 2, pp. 416-421, 2008.

[80] A. R. English, "3-Screw Bed Leveling and the Importance of a Level Print Bed on a 3D Printer," www.protoparadigm.com, 2013. [Online]. Available: https://tinyurl.com/o9otm4u.

[81] X. Shan, S.-K. Kuo, J. Zhang and C.-H. Menq, "Ultra Precision Motion Control of a Multiple Degrees of Freedom Magnetic Suspension Stage," *IEEE/ASME TRANSACTIONS ON MECHATRONICS*, 2002.

[82] S.-K. Kuo, X. Shan and C.-H. Menq, "Large Travel Ultra Precision x y theta Motion Control of a Magnetic-Suspension Stage," *IEEE/ASME TRANSACTIONS ON MECHATRONICS*, 2003.

[83] C.-H. Menq and S.-K. Kuo, "Modeling and Control of a Six-Axis Precision Motion Control Stage," *IEEE/ASME TRANSACTIONS ON MECHATRONICS*, 2005.

[84] Nikon, "Following stage planar motor". Patent US 6927505 B2.

[85] Nikon, "Stacked six degree-of-freedom table". Patent US 20060033043 A1.

[86] I. Boldea and S. A. Naser, LINEAR MOTION ELECTROMAGNETIC SYSTEMS, 1985.

[87] B. A. Awabdy, W.-C. Shih and D. M. Auslander, "Nanometer Positioning of a Linear Motion Stage Under Static Loads," *IEEE/ASME TRANSACTIONS ON MECHATRONICS*, 1998.

[88] K. Tan, T. Lee and S. Huang, Precision Motion Control: Design and Implementation, Springer.

[89] J. E. Howard, O. H. Lieder, B. B. Bowlds and P. A. Lindsay, "Capacitive sensor and method for non-contacting gap and dielectric medium measurement". Patent US 7256588 B2, 2007.

[90] A. R. George and J. A. Dahlquist, "Non-contact sensor and method using inductance and laser distance measurements for measuring the thickness of a layer of material overlaying a substrate". Patent US 5355083 A, 1994.

[91] U. o. Texas, "Methods for high-precision gap and orientation sensing between a transparent template and substrate for imprint lithography". Patent US 6954275 B2.

[92] E. E. Moon, "Nanometer-precision tip-to-substrate control and pattern registration for scanning-probe lithography". Patent US 7474410 B2.

[93] B. J. Choi, S. V. Sreenivasan and S. C. Johnson, "High precision orientation alignment and gap control stages for imprint lithography processes". Patent US 6873087 B1.

[94] X. Wen, L. M. Traverso, P. Srisungsitthisunti, X. Xu and E. E. Moon, "High precision dynamic alignment adn gap control for optical near-field nanolithography," *Journal of Vacuum Science and Technology,* 2013.

[95] A. VanHorn and W. Zhou, "Design and optimization of a high temperature microheater for inkjet deposition," *The International Journal of Advanced Manufacturing Technology,* pp. 1-11, 2016.

[96] N. D. Holt, M. Montazeri and W. Zhou, "Microheater Array Powder Sintering: A Novel Additive Manufacturing Process," *Journal of Manufacturing Processes,* vol. 31, pp. 536-551, 2017.

[97] S. Chol, "Enhancing thermal conductivity of fluids with nanoparticles," *ASME-Publications-Fed,* vol. 231, pp. 99-106, 1995.

[98] nanoComposix, "50 nm Silver Nanospheres," https://nanocomposix.com, 2017. [Online]. Available: https://tinyurl.com/y9dwkufw. [Accessed 9 February 2017].

[99] N. Ren, L. Jia and D. Wang, "Numerical simulation analysis on the temperature field in indirect selective laser sintering of 316L," *Advanced Materials Research,* vol. 711, pp. 209-213, 2013.

[100] F. R. Liu, Q. Zhang and W. P. Zhou, "Micro scale 3D FEM simulation on thermal evolution within the porous structure in selective laser sintering," *Journal of Materials Processing Technology,* vol. 212, pp. 2058-2065, 2012.

[101] P. Peng, A. Hu and Y. Zhou, "Laser sintering of silver nanoparticle thin films: microstructure and optical properties," *Applied Physics A,* vol. 108, no. 3, pp. 685-691, 2012.

[102] Schott Advanced Optics, "AF 32 Thin Glass," http://www.schott.com, [Online]. Available: https://tinyurl.com/y8z3h79p. [Accessed 16 March 2017].

[103] Insaco, "Sapphire," 2018. [Online]. Available: http://www.insaco.com/materials/other-materials/sapphire. [Accessed 20 March 2018].

[104] M. Cunha, T. Moonlight and R. Lad, "Enabling very high temperature acoustic wave devices for sensor & frequency control applications," in *IEEE Ultrasonics Symposium, 2007*, 2007.

[105] Schott Advanced Optics, "Schott HermeS - Hermetic Through Glass Vias (TGV)," us.schott.com, [Online]. Available: https://tinyurl.com/y98qu8fn. [Accessed 16 March 2017].

[106] EPOXY TECHNOLOGY, INC., "EPO-TEK P1011 Technical Data Sheet," www.epotek.com, [Online]. Available: https://tinyurl.com/y9ld6ty8. [Accessed 13 April 2017].

[107] "Thermophysical Data on Platinum," *Platinum Metals Review,* vol. 28, no. 4, p. 164, 1984.

[108] N. D. Holt and W. Zhou, "Design and Fabrication of an Experimental Microheater Array Powder Sintering Printer," *JOM,* 2018.

[109] OptoSigma, "Sub-micron Worm Drive Micrometer Heads," [Online]. Available: https://www.global-optosigma.com/en/page_pdf/WGP.pdf?v=1499622866. [Accessed 27 November 2017].

[110] Newport, "AJS100-20-127-S," www.newport.com, [Online]. Available: https://tinyurl.com/yc9azmwg. [Accessed 27 November 2017].

[111] Automation Technology Inc., "NEMA17 Stepper Motor (KL17H248-25-4A) for 3D Printer, 67 oz-in," www.automationtechnologiesinc.com, [Online]. Available: https://tinyurl.com/y7bvpo7e. [Accessed 27 November 2017].

[112] A. Fleming, "A review of nanometer resolution position sensors: Operation and performance," *Sensors and Actuators A: Physical,* vol. 190, pp. 106-126, 2012.

[113] Y. Ganjeh, B. Song and K. Pagadala, "A platform to parallelize planar surfaces and control their spatial separation with nanometer resolution," *Review of Scientific Instruments,* vol. 83, no. 10, 2012.

[114] Schott Advanced Optics, "Glass Wafers and Substrates," us.schott.com, February 2018. [Online]. Available: https://tinyurl.com/y95f5mq5. [Accessed March 2018].

[115] DuPont Teijin Films, "Melinex® ST506 Datasheet," [Online]. Available: http://69.67.54.76/FilmEnterprise/Datasheet.asp?ID=271&Version=US.

[116] NovaCentrix, "PSI-211® Conductive Screen Ink Datasheet," www.novacentrix.com, [Online]. Available: https://tinyurl.com/ycal96bz.

[117] Affiliated Manufacturers, Inc., *MSP-485 Precision Screen Printer Brochure.*

[118] J. S. Kang, J. Ryu, H. S. Kim and H. T. Hahn, "Sintering of Inkjet-Printed Silver Nanoparticles at Room Temperature Using Intense Pulsed Light," *Journal of Electronic Materials*, vol. 40, no. 11, pp. 2268-2277, 2011.

[119] Novacentrix, "Metalon® JS-A101A and JS-A102A," www.novacentrix.com, August 2017. [Online]. Available: https://tinyurl.com/y7kspfox. [Accessed 27 November 2017].

[120] The Engineering Toolbox, "Thermal Expansion of Metals," 2018. [Online]. Available: https://tinyurl.com/y7n9dxzh. [Accessed 21 March 2018].

[121] The Engineering Toolbox, "Metals - Melting Temperatures," 2018. [Online]. Available: https://tinyurl.com/ybo44p29. [Accessed 21 March 2018].

[122] Schott AG, "AF 32 eco," 12 2008. [Online]. Available: http://www.markoptics.com/files/Schott%20AF%2032%20eco%20PCP.pdf. [Accessed 3 May 2018].

[123] Zaber, "LRM200A-T3: Motorized linear stage, 200 mm travel, fine resolution," www.zaber.com, 2018. [Online]. Available: https://tinyurl.com/y8v3hgnl. [Accessed 22 March 2018].

[124] Hargraves Fluidics, Inc., "E134-11-050," http://www.hargravesfluidics.com, 2018. [Online]. Available: https://tinyurl.com/yb2uqnwr. [Accessed 23 March 2018].

[125] Zaber, "LSA10A-T4: Motorized linear stage, 10mm travel (controller required)," www.zaber.com, 2018. [Online]. Available: https://tinyurl.com/ybao6t9u. [Accessed 22 March 2018].

[126] MTI Corporation, "4 Paths Micron Precision Film Applicator with Optional (80/120mm) Coating Width and Thickess of 5μm, 10μm, 15μm, 20μm - EQ-Se-KTQ-4S," www.mtixtl.com, [Online]. Available: http://www.mtixtl.com/EQ-Se-KTQ-4S-2.aspx. [Accessed 15 March 2018].

[127] Formlabs, "CLEAR SAFETY DATA SHEET," 10 February 2016. [Online]. Available: https://formlabs.com/media/upload/Clear-SDS_u324bsC.pdf. [Accessed 20 April 2018].

[128] NovaCentrix, "PFI-600® Conductive Flexo Ink," July 2017. [Online]. Available: https://tinyurl.com/y7z59e95. [Accessed 3 May 2018].

[129] Grand View Research, "Flexible Electronics Market By Components (Display, Battery, Sensors, Memory), By Application (Consumer Electronics, Automotive, Healthcare, Industrial) And Segment Forecast To 2024," Grand View Research, San Francisco, 2016.

[130] T. Aubert, O. Elmazria and B. Assouar, "Study of tantalum and iridium as adhesion layers for Pt/LGS high temperature SAW devices," in *IEEE International Ultrasonics Symposium*, 2009.